

Integrated Dynamical Approach to Relativistic Heavy Ion Collisions

T. Hirano,^{1,2} P. Huovinen,^{3,4} K. Murase,^{2,1} Y. Nara,⁵

¹Department of Physics, Sophia University, Tokyo 102-8554, Japan

²Department of Physics, The University of Tokyo, Tokyo 113-0033, Japan

³Frankfurt Institute for Advanced Studies, 60438 Frankfurt am Main, Germany

⁴Institut für Theoretische Physik, Johann Wolfgang Goethe-Universität,
60438 Frankfurt am Main, Germany

⁵Akita International University, Yuwa, Akita-city 010-1292, Japan

November 5, 2018

Abstract

We review integrated dynamical approaches to describe heavy ion reaction as a whole at ultrarelativistic energies. Since final observables result from all the history of the reaction, it is important to describe all the stages of the reaction to obtain the properties of the quark gluon plasma from experimental data. As an example of these approaches, we develop an integrated dynamical model, which is composed of a fully (3+1) dimensional ideal hydrodynamic model with the state-of-the-art equation of state based on lattice QCD, and subsequent hadronic cascade in the late stage. Initial conditions are obtained employing Monte Carlo versions of the Kharzeev-Levin-Nardi model (MC-KLN) or the Glauber model (MC-Glauber). Using this integrated model, we first simulate relativistic heavy ion collisions at the RHIC and LHC energies starting from conventional smooth initial conditions. We next utilise each Monte Carlo samples of initial conditions on an event-by-event basis and perform event-by-event dynamical simulations to accumulate a large number of minimum bias events. A special attention is paid to performing the flow analysis as in experiments toward consistent comparison of theoretical results with experimental data.

Contents

1	Introduction	2
2	Model	4
2.1	<i>Hydrodynamic Equations</i>	5
2.2	<i>Equation of State</i>	6
2.3	<i>Fluid to Particles</i>	9
2.4	<i>Hadronic Cascade</i>	12
2.5	<i>Brief overview of hydro + hadronic cascade models</i>	13
2.6	<i>Initial Conditions</i>	19
2.7	<i>Brief overview of event-by-event initial conditions</i>	29
3	Results from smooth initial profile	36
3.1	<i>Results at RHIC</i>	37
3.2	<i>Results at LHC</i>	39
4	Results from event-by-event hybrid simulations	42
4.1	<i>Event plane method</i>	42
4.2	<i>Multi-particle cumulants</i>	47
4.3	<i>Results</i>	50
5	Conclusion	56

1 Introduction

Heavy ion programs at Large Hadron Collider (LHC) in European Organization for Nuclear Research (CERN) and at Relativistic Heavy Ion Collider (RHIC) in Brookhaven National Laboratory (BNL) have focused on the physics of strongly interacting matter of quarks and gluons under extreme conditions, namely, on the physics of the quark gluon plasma (QGP) [1]. By colliding two heavy nuclei at relativistic energies, the matter formed in the collision is expected to be in the state of QGP in temperatures up to 400 MeV $\sim 4 \times 10^{12}$ K. Such a high temperature was reached in the early universe about ten micro seconds after the Big Bang. One of the main goals of the heavy ion programs is to extract bulk and transport properties of the QGP from analyses of experimental data.

So far, a vast body of experimental data have been obtained at RHIC and LHC. Among them, the azimuthal anisotropy of the emitted particles, so-called elliptic flow [2, 3, 4, 5, 6, 7, 8, 9, 10, 11, 12, 13] is one of the main observables to provide information of the bulk properties of the QGP. In particular, the large observed value of elliptic flow at RHIC was one of the main reasons to conclude that the matter produced in the collisions at RHIC does indeed thermalise and form QGP [14, 15].

In a non-central collision of two spherical nuclei, the reaction zone has an almond-like shape in the plane perpendicular to the collision axis, so called transverse plane. Because of this geometry, pressure gradient within the reaction zone is not azimuthally isotropic, but it is larger along the impact parameter than to the direction orthogonal to it. This leads to anisotropic expansion of the system with more particles being emitted along the impact parameter than orthogonal to it. It is customary to call the plane spanned by the beam and the impact parameter a reaction plane, and thus we say that larger emission along the impact parameter means larger emission “in-plane” than “out-of-plane”. This anisotropic particle emission can be quantified by Fourier expanding the azimuthal distribution of observed particles. In particular, this kind of anisotropy is quantified by the second Fourier coefficient of the expansion, v_2 . Since a finite v_2 in a Fourier expansion corresponds to an elliptic shape, this

anisotropy is commonly called *elliptic flow* [16]. Quite surprisingly ideal hydrodynamics, which neglects all the dissipative effects, gave a good description of the elliptic flow observed at RHIC [17, 18, 19, 20, 21, 22]. Given a fact that the expansion rate of the system formed in a heavy ion collision is tremendously large ($\sim 10^{24}$ /sec), it is far from obvious that dissipative effects can be neglected. Since in ideal hydrodynamics perfect local equilibrium is assumed to hold at any instant, couplings among constituents of the fluid must be so strong that relaxation of the system against any thermodynamic forces happens extremely quickly. Thus, from the agreement of hydrodynamic prediction with the elliptic flow data, an announcement of the “discovery of perfect fluidity” was made [23], and a new paradigm of the strongly coupled QGP (sQGP) was established [14, 15, 24, 25, 26, 27].

However, the described shape of the reaction zone is realistic only as an average over many collisions. Since the nuclei are not uniform but consist of separate nucleons, we may expect the reaction zone in a single event to depict similar granular structure to the nuclei. For example, according to the Monte-Carlo Glauber model [28, 29, 30] the reaction zone consists of several peaks (*a.k.a.* hot spots) and valleys originating from the configuration of nucleons in the colliding nuclei. This irregular structure means that even if the underlying shape of the reaction zone in a non-central collision is almond-like, it has been distorted and tilted. Thus, if one fits an ellipse to the reaction zone, its minor axis no longer aligns with the impact parameter. As described, elliptic flow is generated by the anisotropy of pressure gradient. Now, if the thermodynamic language of pressure gradients is applicable in an individual event, the largest gradient and thus the largest emission of particles is not along the reaction plane. It is along the participant plane¹, which is spanned by the beam and the minor axis of the reaction zone. Thus, the particle distribution should not be Fourier expanded with respect to the reaction plane, but to the participant plane.

The importance of these event-by-event fluctuations of the shape and orientation of reaction zone was discovered when trying to understand the behaviour of v_2 in Cu+Cu collisions. It had been found that when experimentally measured v_2 was divided by the modelled eccentricity of the reaction zone², ε , the ratio v_2/ε scales with transverse density $(1/S)dN/dy$, where S is the modelled transverse area of the overlap region and dN/dy is the measured final particle multiplicity at midrapidity [3, 31]. However, the measured v_2 in Cu+Cu collisions did not obey such a scaling, but when the eccentricity ε was replaced by the participant eccentricity $\varepsilon_{\text{part}}$, the scaling was restored [32]. The main difference is that ε is always evaluated with respect to the reaction plane, whereas the participant eccentricity $\varepsilon_{\text{part}}$ is evaluated with respect to the participant plane in each individual event, and thus takes into account the fluctuations in the orientation of the reaction zone [33].

Since the reaction zone has a complicated azimuthal structure, and the elliptic flow was explained as a result of the azimuthal variation of the pressure gradient, it is natural to expect that the Fourier coefficients beyond v_2 would be nonzero as well. The third coefficient in the Fourier expansion, v_3 , is called triangular flow [34]. It is generated by the triangular component of the shape of the fluctuating reaction zone, and some puzzling phenomena in intermediate transverse momentum regions can be interpreted as manifestation of triangular flow. For example, Mach-cone like structure was discovered in the away-side region in di-hadron correlation functions at RHIC [35, 36, 37] when one subtracts background elliptic flow component from it. Recently, it was found that these di-hadron correlation functions can be reproduced by a sum of independently analysed higher harmonic components [38, 39], which indicates that Mach-cone like structure would be caused simply by collective triangular flow.

If one Fourier-decomposes the azimuthal particle distribution, one can obtain information how the system responds to the initial fluctuating profile and from this response one may deduce what the properties of the system itself are [40, 41, 42, 43, 44]. This reminds an analysis in observational cosmology: Through decomposition of power spectrum of cosmic microwave background radiation into

¹Also called event plane is some of the literature.

²Sometimes called standard eccentricity ε_{std} . For definitions, see Section 2.6.

spherical harmonics, one can constrain important cosmological constants and even mass/energy budget of the universe [45].

In the observational cosmology, analysis tools [46] played important roles in extracting cosmological parameters. The situation in the physics of relativistic heavy ion collisions is quite similar to this [47]: One has to develop analysis tools to extract the properties of the QGP from experimental data. From this point of view, let us overview the dynamics of heavy ion collisions. High energy heavy ion collisions contain rich physics and exhibit many aspects of dynamics according to relevant energy and time scales. Two energetic, Lorentz-contracted, heavy nuclei collide with each other. These nuclei can be described by the colour glass condensate (CGC), a universal form of hadrons and nuclei at extremely high energies [48, 49, 50]. These collisions can be viewed as collisions of two bunches of highly coherent and dense gluons. Just after the collisions, longitudinal colour electric and magnetic fields, which are also known as the colour flux tubes [51] are formed between two passing nuclei. Subsequent non-equilibrium evolution of these colour fields towards locally thermalised QGP is called “glasma” [52]. Once local thermalisation is achieved, a QGP fluid expands hydrodynamically, cools down and turns into a hadronic gas. Hadrons continue to rescatter until the system is so dilute that interactions become very rare, and hadrons stream freely towards the detectors.

Since the final observables are the result of all these various stages of the collision, it is important to describe the heavy ion collision as a whole. So far, we have developed the following integrated dynamical model [53, 54] to describe the dynamics of relativistic heavy ion collisions. For the initial stage, initial conditions are calculated using the CGC picture [55, 56, 57]. Using these initial conditions, we describe fully three dimensional ideal hydrodynamic expansion of the QGP fluid [21, 22] using a realistic equation of state from lattice QCD simulations [58, 59, 60]. The late stage evolution of the hadron gas is described using microscopic kinetic theory [61]. Technical details about numerical simulations of ideal hydrodynamics and hadronic cascades can be found in Ref. [62].

In this paper, we discuss experimental observables, in particular anisotropic flow, at RHIC and LHC energies using an integrated dynamical model. A special emphasis will be put on discussion about initial conditions and final flow analysis methods from an event-by-event analysis point of view. In theoretical calculations both the reaction plane and the participant plane are trivially known, but in experiments it is impossible to measure the reaction plane, and it is quite hard to precisely determine the participant plane from the finite number of observed particles. Thus, several flow analysis methods have been proposed [63, 64, 65] to experimentally measure anisotropic flow. Hence, a *consistent* comparison of hydrodynamic results with experimental observables is non-trivial. In this paper we demonstrate the differences of several experimental methods of flow analysis by using them to analyse the output of the integrated dynamical model.

The paper is organised as follows. In Sec. 2 we describe and review the hybrid models, in which hydrodynamics is combined with hadronic cascade, and hydrodynamic simulations on an event-by-event basis. In particular we describe each module and the interfaces between them of our integrated dynamical model. In Sec. 3, we first summarise the results obtained using smooth initial profiles, which are the conventional initial conditions employed in hydrodynamic simulations. We next show results from event-by-event hydrodynamic simulations in Sec. 4 emphasising the importance of employing the same flow analysis method as in experiment. Section 5 is devoted to the conclusion and outlook.

2 Model

Integrated dynamical models, in general, consist of three separate stages: Initial conditions, hydrodynamics and hadronic cascade. In our version, the initial particle production in the collision of the nuclei is either described by the MC-KLN version of the colour glass condensate, or parametrised using the MC-Glauber model. These models provide the initial state for the subsequent expansion of the matter,

which we describe by relativistic ideal hydrodynamics. As for the equation of state, we employ results from the state-of-the-art lattice QCD simulations [58, 59]. Once the matter is dilute enough to form hadrons, we switch the description of the system from fluid dynamics to microscopic hadron cascade. In this section we describe all these stages of the integrated model, and how we connect hydrodynamics to cascade. We also review current status of the equation of state and its application, hybrid models, and event-by-event hydrodynamic simulations.

2.1 Hydrodynamic Equations

To describe a system in length scales much larger than a typical microscopic length scale, like the mean free path, it is sufficient to characterise it in terms of a few macroscopic fields: The energy-momentum tensor $T^{\mu\nu}$, and conserved charge currents j_i^μ (if any). In relativistic fluid dynamics, the equations of motion are given by the conservation laws for these fields

$$\partial_\mu T^{\mu\nu} = 0 \quad \text{and} \quad \partial_\mu j_i^\mu = 0. \quad (1)$$

Without any additional constraints these $4 + n$ (n is the number of conserved currents) equations contain $10 + 4n$ unknown variables. To close the system of equations, one either has to provide further equations in the form of constituent equations for dissipative currents (shear stress tensor $\pi^{\mu\nu}$, bulk pressure Π and energy flow/particle number diffusion q_i), or to eliminate some of the variables by further approximations. In the following we apply the latter approach and reduce the number of unknowns by assuming that the fluid is in exact local thermodynamical equilibrium.

In a local thermodynamical equilibrium, the single particle phase-space distribution for noninteracting fermions or bosons is

$$f_0(p, x) = \frac{g}{(2\pi)^3} \frac{1}{\exp(p \cdot u(x) - \mu(x))/T(x) \pm 1}. \quad (2)$$

When one applies this to the kinetic theory definitions of the energy-momentum tensor and charged currents, one obtains

$$T^{\mu\nu}(x) = [\epsilon(x) + P(x)] u^\mu(x) u^\nu(x) - P(x) g^{\mu\nu}, \quad \text{and} \quad j_i^\mu(x) = n_i(x) u^\mu(x), \quad (3)$$

respectively, where ϵ is the energy, and n_i are the charge densities in the local rest frame of the fluid, P is the thermodynamic pressure and u^μ is the fluid flow four-velocity. The Eqs. (3) imply that for a fluid in local thermodynamical equilibrium the dissipative currents are zero. This consideration of a non-interacting gas in local equilibrium is the starting point of the ideal fluid approximation: One postulates that the energy-momentum tensor and charge currents are of the form of Eqs. (3), and thus the dissipative currents are zero by definition.

Such an approximation reduces the number of unknown variables in Eqs. (1) to $5 + n$: the above mentioned densities, pressure and three components of the flow four-velocity (note that the usual normalisation $u_\mu u^\mu = 1$ reduces the number of unknowns by one). To finally close the system of equations, an additional equation is usually provided in the form of the equilibrium equation of state (EoS) of the matter, which expresses the pressure and densities in terms of thermodynamical parameters temperature T and chemical potentials $\{\mu_i\}$, $P = P(T, \{\mu_i\})$. However, to solve the Eqs. (1), it is often practical to provide the EoS in the form $P = P(\epsilon, \{n_i\})$ connecting the pressure directly to the densities. The knowledge of temperature and chemical potentials is not necessarily required to calculate the evolution of the fluid itself.

Note that once the EoS, and boundary conditions (usually referred to as initial conditions) for the set of differential equations in Eqs. (1) are fixed, the evolution is determined by Eqs. (1). In the ideal

fluid approximation, the only place where information about the nature of the constituents of the fluid and their microscopic interactions enters, is the EoS.

In the implementation of our model, we solve Eqs. (1) numerically in all three spatial dimensions. We employ the Milne coordinates (τ, x, y, η_s) , where $\tau = \sqrt{t^2 - z^2}$ is proper time and $\eta_s = \frac{1}{2} \log \frac{t+z}{t-z}$ is space-time rapidity.

Since we are mostly interested in the observables at midrapidity in the collider energies³, we can ignore the baryon current [66, 67, 68, 69]⁴. As usual in hydrodynamical models, we take the spatial boundary condition to be vacuum at infinity [70], *i.e.* the hydrodynamical evolution proceeds independently without any feedback from the cascade. The temporal boundary, *i.e.* the initial value(s) for the differential equations are described in Section 2.6. We employ the Piecewise Parabolic Method (PPM) [71] as an algorithm to solve the equations of ideal hydrodynamics (Eqs. (1)). PPM is known to be robust against strong shocks, therefore it is suitable to apply for bumpy initial conditions in event-by-event hydrodynamic simulations. For details on PPM, see Ref. [62].

2.2 Equation of State

The equation of state (EoS) of strongly interacting matter can be obtained either by using various models or by lattice QCD calculations [72]. Even if the recent lattice QCD calculations of the EoS have provided continuum extrapolated results [73], there is a practical reason to use the hadron resonance gas (HRG) model for the EoS at low temperatures. When converting fluid to particles using the Cooper-Frye procedure as described in section 2.3, the conservation laws are obeyed without any further considerations if the degrees of freedom are the same before and after particlisation. In other words, if the emitted particles are the same particles the fluid consists of. If the fluid is described as hadron resonance gas, the degrees of freedom and their properties are well known, and these degrees of freedom are the experimentally observable hadrons which distributions we eventually want to calculate. HRG has also been shown to provide a reasonably good approximation of the EoS of interacting hadron gas in temperatures slightly below the pion mass [74], and its use is therefore justified.

To show how an EoS combining a hadron resonance gas at low temperatures, and lattice QCD results at high temperatures can be made, we briefly review the construction of the *s95p-v1.1* parametrization [53, 60]. The high temperature part of this EoS is based on the lattice QCD results of the hotQCD collaboration [58, 59], and its low temperature part contains the same hadrons and resonances as the JAM hadron cascade [61]. We have also used this EoS to calculate the results discussed in Sections 3 and 4.

The starting point of the construction of the *s95p* EoS is the trace anomaly $\Theta(T) = \epsilon(T) - 3P(T)$ evaluated on lattice, see Fig. 1. The lattice results are parametrised and connected to the trace anomaly of HRG preserving the smooth crossover nature of the transition. The trace anomaly is then converted to pressure via

$$\frac{P(T)}{T^4} - \frac{P(T_{\text{low}})}{T_{\text{low}}^4} = \int_{T_{\text{low}}}^T \frac{dT'}{T'^5} \Theta(T'), \quad (4)$$

where pressure at the lower integration limit, T_{low} , is given by HRG. Energy and entropy densities are subsequently obtained via laws of thermodynamics. By construction such an EoS is limited to zero net baryon density and zero net strangeness, but as mentioned zero charge is a good approximation when describing the system at midrapidity in collisions at RHIC and LHC.

The trace anomaly of the *s95p-v1.1* EoS is shown in Fig. 1, and compared to recent lattice QCD results. It differs considerably from the continuum extrapolated result by the Budapest-Wuppertal

³ $\sqrt{s_{\text{NN}}} = 200$ GeV at RHIC and $\sqrt{s_{\text{NN}}} = 2.76$ TeV at LHC.

⁴The other conserved currents relevant for heavy ion collisions; electric charge, isospin and strangeness are in general either tiny or zero.

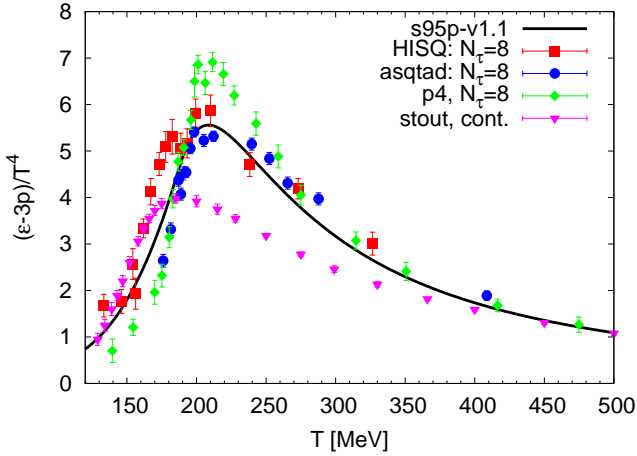


Figure 1: The parametrised trace anomaly compared with lattice results calculated with $p4$ [75], $asqtad$ and $HISQ/tree$ [76] actions as well as the continuum extrapolated result obtained using $stout$ action [73].

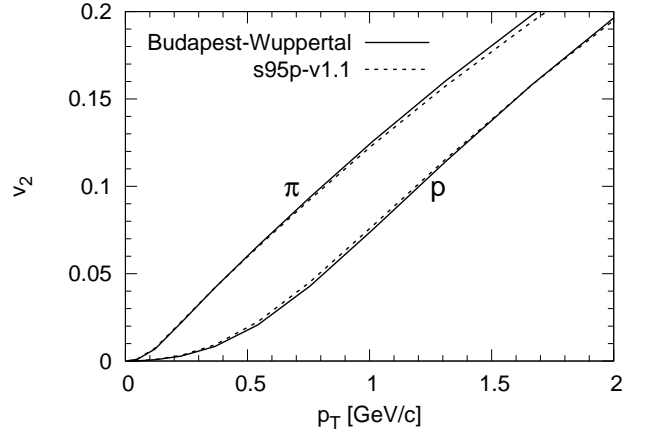


Figure 2: The p_T -differential elliptic flow of pions and protons in $b = 7$ fm Au+Au collisions at $\sqrt{s_{NN}} = 200$ GeV evaluated using ideal fluid hydrodynamical model using EoS $s95p-v1$ [60] and the parametrised Budapest-Wuppertal EoS [73].

collaboration [73]. However, the Budapest-Wuppertal EoS deviates from HRG already at $T \approx 130$ – 140 MeV, which necessitates switching from fluid to cascade below this temperature leading to much worse reproduction of data in our calculations. The $s95p$ parametrisation follows HRG up to $T = 183$ MeV temperature providing much more freedom in choosing the switching temperature, and therefore we prefer to use it. To estimate the uncertainty our choice of EoS produces in the particle anisotropies, we have calculated the elliptic flow anisotropy v_2 in impact parameter $b = 7$ fm Au+Au collisions at the full RHIC energy ($\sqrt{s_{NN}} = 200$ GeV), see Fig. 2. In this calculation we follow the procedure used in Ref. [60] to test various parametrizations of the EoS. We use ideal fluid hydrodynamical model and assume chemical equilibrium until kinetic freeze-out. The model is initialized using an optical Glauber model with components proportional to the number of participants and binary collisions (see Sec. 2.6 and Refs. [14, 77]) The parameters are chosen to reproduce the centrality dependence of charged particle multiplicity. The usual procedure requires choosing the freeze-out temperature to reproduce the particle spectra in most central collisions, but that would require the use of temperature $T_{fo} \approx 140$ MeV. As mentioned, the Budapest-Wuppertal EoS deviates from HRG below that temperature, and thus converting fluid to free particles in such a temperature violates conservation of energy. Therefore we used freeze-out temperature $T_{fo} = 125$ MeV for both EoSs even if it leads to slightly flatter p_T distributions of pions and protons than experimentally observed. Both EoSs, Budapest-Wuppertal and $s95p$ lead to very similar p_T distributions at that temperature. As can be seen in Fig. 2, the difference in p_T -differential elliptic flow is tiny as well, and smaller than the experimental errors. Thus we consider the use of $s95p-v1.1$ EoS a reasonable approximation.

Similar insensitivity to the details of the EoS was seen in Ref. [60] where different parametrizations of lattice EoS were tested. Even if the EoS governs the expansion of the fluid and buildup of collective motion, the details of the EoS have tiny observable consequences. The rule of thumb is that the stiffer the EoS, *i.e.*, the larger the speed of sound in the fluid, the larger the flow velocity generated during the expansion. But, even if larger flow velocity mean flatter p_T spectrum (see *f.ex.* Ref. [78]), this effect can be negated by choosing the fluid to freeze-out earlier at larger temperature, by assuming later thermalisation time and thus later start of the hydrodynamical evolution, by changing the initial

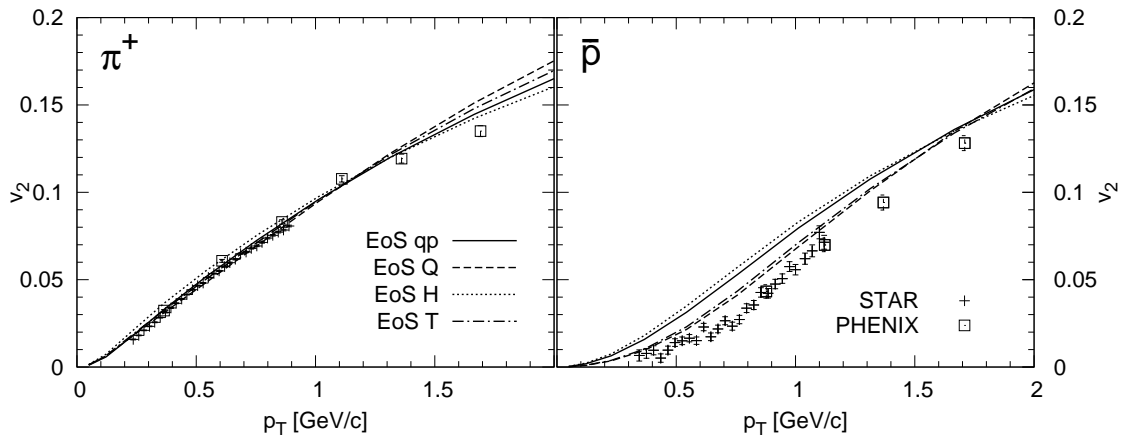


Figure 3: Elliptic flow of pions and antiprotons vs. transverse momentum in minimum bias Au+Au collisions at $\sqrt{s_{NN}} = 200$ GeV calculated using four different EoS [80] and compared with the data by the STAR [79] and PHENIX [6] collaborations. The labels stand for a lattice QCD inspired quasiparticle model (qp), EoS with a first order phase transition (Q), a parametrized smooth but rapid crossover (T) and pure hadron resonance gas with no phase transition (H).

shape of the density distribution (if the model allows) or by any combination of these three. The integrated dynamical models discussed in this paper have no freeze-out temperature, but the final particle distributions are sensitive to the switching temperature from hydro to cascade, and all these problems hamper these models as well.

Based on the p_T distributions on particles alone, we can basically only say that the EoS must contain a large number of degrees of freedom. Otherwise the p_T distributions come too flat, see discussion and Fig. 5 in Ref. [81], nor does the EoS contain all the observed particles and resonances. To say anything beyond the large number of degrees of freedom requires the use of more sophisticated observables like the azimuthal anisotropy v_2 or the HBT-radii, a.k.a. femtoscopy. In general the changes in v_2 due to different EoSs can be compensated by changing the freeze-out temperature. There is, however, an exception. The p_T differential anisotropy of protons, $v_2(p_T)$, is to some extent sensitive to the order of phase transition [80]. This is demonstrated in Fig. 3 where pion and proton $v_2(p_T)$ in minimum bias Au+Au collisions at $\sqrt{s_{NN}} = 200$ GeV are calculated using ideal fluid hydrodynamical model, and four different EoSs. The EoSs are the bag model based EoS with a first order phase transition between HRG and ideal parton gas (EoS Q), pure hadron resonance gas with no phase transition (EoS H), a lattice inspired quasiparticle model EoS (EoS qp, which is quite close to the present lattice QCD EoSs) by Schneider and Weise [82], and an EoS with a parametrised smooth crossover from HRG to ideal parton gas (EoS T). As seen in the figure, the sensitivity of pion $v_2(p_T)$ on the EoS is tiny, but proton $v_2(p_T)$ shows clear sensitivity on EoS. Surprisingly it is the EoS Q with the first order phase transition which provides the best fit to the data—a construction ruled out by the lattice QCD calculations. The lattice inspired EoS qp leads to proton $v_2(p_T)$ which is clearly above the data, and almost as large as the $v_2(p_T)$ obtained using the purely hadronic EoS H. The EoS T, which has a very rapid crossover leads to proton $v_2(p_T)$ which is almost as close to the data than the one obtained using EoS Q. This means that the order of the phase transition does not affect the build up of anisotropy, but how rapid the transition is does have an effect. Nevertheless, EoS T is ruled out by the present lattice data.

On the other hand, it can be argued that a soft EoS leads to a long lifetime of the system, which is excluded by the HBT measurements [83]. It has also been shown that if one assumes a relatively hard, lattice inspired EoS, it is possible to reproduce the measured HBT radii [84], although in that

case the proton $v_2(p_T)$ is not reproduced. This apparent contradiction appears when using ideal fluid dynamics. When dissipative corrections are applied, the proton $v_2(p_T)$ can be reproduced also when a lattice based hard EoS is used, see Fig. 36 in Sect. 3.1, or Ref. [85]. Thus there is no contradiction between lattice QCD EoS and the observed particle anisotropies.

The previous discussion about the sensitivity of the particle distributions to EoS is based on ideal fluid dynamics, since so far there has been no systematic study addressing what we can learn about the EoS of strongly interacting matter using either dissipative hydrodynamics or integrated models. But since dissipative corrections are supposed to be small in the fluid dynamical stage, it is highly unlikely that adding dissipation would make the fluid evolution more sensitive to the details of the EoS. Thus we may expect that what we have learned about the effects of EoS on flow using ideal fluid dynamics, holds for dissipative fluids as well.

2.3 Fluid to Particles

The QGP produced in relativistic heavy ion collisions expands, cools down and goes through a transition to a hadronic gas.⁵ At this late stage, the hadronic system is so diluted that it would be hard to maintain equilibrium during the evolution. Thus, we switch from a macroscopic fluid dynamical picture to a microscopic kinetic picture at a switching temperature T_{sw} . In this subsection, we discuss how to change from hydrodynamic description to kinetic description. We will discuss dynamics of hadron cascade in the next subsection.

We employ the Cooper-Frye formula [86] to calculate the single particle phase-space distribution for all hadrons in the hadronic equation of state. For a hadron of species i , the contribution to the distribution from a single fluid element located at x is

$$\begin{aligned} f_i(p, x) d^3x &= \frac{d\Delta N_i}{d^3p}(x) \\ &= \frac{g_i}{(2\pi)^3 E} \frac{p \cdot \Delta\sigma(x)}{\exp[(p \cdot u(x) - \mu_i(x))/T(x)] \pm 1}. \end{aligned} \quad (5)$$

Here $\Delta\sigma$ is a normal vector of a surface element of a constant temperature hypersurface $T(x) = T_{\text{sw}}$ ⁶.

In the actual calculations, we Monte-Carlo sample the distributions of hadrons emitted from individual surface elements [22]. Regarding this, some comments on the conservation laws are in order here:

1. The Cooper-Frye formula counts the *net* number of emitted particles [86]. Here the net number means the number of particles moving outwards through the surface minus the number of particles moving inwards. Thus the number obtained from Eq. (5) could be negative in a case of a fluid element with either a space-like normal vector $(\Delta\sigma)^2 < 0$ or a time-like normal vector having a negative time component. This so-called negative contribution problem of Cooper-Frye, is a long-standing problem in hydrodynamical modelling of relativistic heavy ion collisions. Note that the *total* number of particles obtained by summing the contribution given by Eq. (5) over *all* surface elements is positive for all initial states relevant for heavy ion collisions. Although the in-coming particles are necessary to ensure the energy momentum conservation, it is conceptually difficult to treat the negative number in the subsequent kinetic approach.⁷ However, at the time of particlisation at $T = T_{\text{sw}}$ the collective flow is large, and thus the particle distributions are

⁵It is not necessarily a phase transition. As mentioned in the previous section, the recent lattice QCD simulations predict a crossover rather than a phase transition between the QGP phase and the hadron phase.

⁶Note that this is not a freezeout hypersurface since in the subsequent stage hadrons still interact with each other.

⁷ One possible solution would be to provide the cascade with the information of the location of the particlisation hypersurface, and remove from the cascade the hadrons which enter the space-time region within the hypersurface.

boosted to the direction of the flow, i.e. outwards. Therefore the yield of the in-coming particles is much smaller than the yield of out-going particles, and they form only a small correction of the order of 5% to the total multiplicity and the energy of the system⁸. As a first order approximation, we may thus ignore these in-coming particles without violating the conservation laws significantly.

2. By sampling we create an integer number of particles from a tiny fluid element whose three dimensional volume is typically $\sim 0.1 \text{ fm}^3$. An expectation value of the number of particles from this fluid element in the grand canonical ensemble is, of course, not an integer and in our calculations less than unity. Therefore energy, momentum and charges are not conserved in each individual sampling, but only in average — as is customary for a grand canonical ensemble. This issue could be resolved by an oversampling method: At each fluid element, N times larger number of particles is sampled with N being large and, the subsequent dynamics of hadrons is simulated with the cross section divided by N to ensure the original Boltzmann equation [88, 89]. This procedure can maintain energy momentum conservation of the order of $\mathcal{O}(1/N)$ at the particlisation. However, this would be numerically expensive and neglect the effect of fluctuations because different events are averaged over in the oversampling method. A faster method which is called “local-ensemble” method has been proposed in Refs. [90, 91, 92]. An alternative approach is to impose the requirement of the conservation of energy and charges on the sampling procedure as done in Refs. [87, 93]. This approach maintains the effect of fluctuations, but requires generating several ensembles of particles, where only parts are kept to avoid bias.
3. In principle one should switch from a macroscopic fluid picture to a microscopic particle picture in a temperature region where both descriptions give similar results. However, the single particle distribution under *local* equilibrium never becomes a solution of the Boltzmann equation: One needs viscous corrections to the local equilibrium distribution to match the two solutions. Since we use ideal fluid hydrodynamics without any dissipative corrections, the hydrodynamical evolution always differs from the cascade. Thus we cannot expect to find a region where the solutions of both models would agree, and simply regard the single particle phase-space distribution obtained using hydrodynamics as an initial condition for the hadron cascade.

Keeping these issues and assumptions in mind, we calculate a discrete single particle phase-space distribution on an event-by-event basis. First, we need the information of the particlisation hypersurface to apply the Cooper-Frye formula (Eq. (5)). We approximate the surface normal $\Delta\sigma^\mu$ in the following way:

Bulk emission: At each time step τ_i in a hydrodynamic simulation, we scan all the fluid elements to check whether particlisation condition for bulk emission (a) $T(\tau_{i-1}) > T_{\text{sw}} > T(\tau_i)$ or (b) $T(\tau_{i-1}) < T_{\text{sw}} < T(\tau_i)$ is satisfied. When this condition is satisfied, information about a surface element vector (a) $\Delta\sigma^\tau = \tau_{\text{sw}}\Delta x\Delta y\Delta\eta_s$ or (b) $\Delta\sigma^\tau = -\tau_{\text{sw}}\Delta x\Delta y\Delta\eta_s$ together with flow velocity u_{sw}^μ at this point are stored. Here particlisation time τ , flow velocities v^x and v^y and flow rapidity $Y_f = \tanh^{-1} v_z$ are linearly interpolated between τ_i and τ_{i-1} such that

$$w_i^0 = \left| \frac{T(\tau_i) - T_{\text{sw}}}{T(\tau_i) - T(\tau_{i-1})} \right|, \quad w_{i-1}^0 = \left| \frac{T_{\text{sw}} - T(\tau_{i-1})}{T(\tau_i) - T(\tau_{i-1})} \right|, \quad (6)$$

$$\tau_{\text{sw}} = \tau_{i-1}w_i^0 + \tau_iw_{i-1}^0, \quad (7)$$

$$v_{\text{sw}}^x = v^x(\tau_{i-1})w_i^0 + v^x(\tau_i)w_{i-1}^0, \quad (8)$$

$$v_{\text{sw}}^y = v^y(\tau_{i-1})w_i^0 + v^y(\tau_i)w_{i-1}^0, \quad (9)$$

$$Y_{f,\text{sw}} = Y_f(\tau_{i-1})w_i^0 + Y_f(\tau_i)w_{i-1}^0. \quad (10)$$

⁸Somewhat larger corrections of the order of 10% were reported in Ref. [87]. We believe that the reason is the different longitudinal structure of the system in these approaches.

Surface emission: At each time step τ_i , we scan all the fluid elements in each direction to check whether particlisation condition for surface emission (a) $T(x_{i-1}) > T_{\text{sw}} > T(x_i)$ or (b) $T(x_{i-1}) < T_{\text{sw}} < T(x_i)$ is satisfied for an adjacent pair of surface elements. Here, for simplicity, we denote only one dimensional dependence, say x coordinate. When this condition is satisfied, information about surface vector (a) $\Delta\sigma^x = \tau_i \Delta\tau \Delta y \Delta\eta_s$ or (b) $\Delta\sigma^x = -\tau_i \Delta\tau \Delta y \Delta\eta_s$ together with flow velocity u_{sw}^μ at this point are stored. Here flow velocities v^x and v^y and flow rapidity Y_f are linearly interpolated between x_i and x_{i-1} at τ_i such that

$$w_i^x = \left| \frac{T(x_i) - T_{\text{sw}}}{T(x_i) - T(x_{i-1})} \right|, \quad w_{i-1}^x = \left| \frac{T_{\text{sw}} - T(x_{i-1})}{T(x_i) - T(x_{i-1})} \right|, \quad (11)$$

$$v_{\text{sw}}^x = v^x(x_{i-1})w_i^x + v^x(x_i)w_{i-1}^x, \quad (12)$$

$$v_{\text{sw}}^y = v^y(x_{i-1})w_i^x + v^y(x_i)w_{i-1}^x, \quad (13)$$

$$Y_{f,\text{sw}} = Y_f(x_{i-1})w_i^x + Y_f(x_i)w_{i-1}^x. \quad (14)$$

Unlike more sophisticated algorithms (see Ref. [87]), which give relatively smooth surfaces, this simple algorithm constructs a granular surface consisting of ‘‘cubes’’. At the limit of infinitely small elements, however, the surfaces are equal. As well, for Cooper-Frye procedure the components of the normal vectors of the surface elements are needed, and those come out similarly in this approach and in the more sophisticated approaches. The main difference is in the positions where the velocity and densities are interpolated on the surface. This causes differences proportional to the grid spacing, which defines the accuracy of the numerics in general as well.

Using this information, we generate a hadron from the surface element. We first calculate an expectation value of the number of hadrons of species i out-going or in-coming through a hypersurface element

$$\Delta N_{\pm}^i = g^i \int \frac{d^3p}{(2\pi)^3 E} \frac{\Theta(\pm p \cdot \Delta\sigma) |p \cdot \Delta\sigma|}{\exp[(p \cdot u - \mu_i)/T_{\text{sw}}] - \epsilon}, \quad (15)$$

where $\epsilon = 1$ for bosons and -1 for fermions. ΔN_{\pm} are always positive by construction. In the following, we neglect ΔN_- for simplicity as we mentioned before. We next create a hadron of species i only when a randomly generated number r_1 ($0 < r_1 < 1$) is less than ΔN_+^i . Note that ΔN_+^i is always less than unity in the usual setting of simulations and its typical values are ~ 0.01 . Such a low value allows us to interpret ΔN_+^i as a probability to create a particle, instead of sampling a Poisson distribution to decide whether and how many particles are created.

If we create a hadron, we choose a momentum for it by sampling the Lorentz invariant distribution

$$\frac{d^3p'}{E'} \frac{1}{\exp[(E' - \mu_i)/T_{\text{sw}}] - \epsilon}. \quad (16)$$

This is a momentum in the local rest frame of the fluid. We next Lorentz-boost it by flow velocity u^μ to obtain momentum in the centre-of-mass frame of the system. By construction the boosted momentum p obeys the distribution

$$\frac{d^3p}{E} \frac{1}{\exp[(p \cdot u - \mu_i)/T_{\text{sw}}] - \epsilon}. \quad (17)$$

We repeat this procedure until the obtained momentum satisfies $p \cdot \Delta\sigma > 0$. Next we consider an weight $p \cdot \Delta\sigma$ in Eq. (15). Suppose r_{max} is the maximum value of $p \cdot \Delta\sigma$, which varies from hypersurface element to element. We generate another random number r_2 , $0 < r_2 < r_{\text{max}}$, and require that the momentum of the hadron fulfils $r_2 < p \cdot \Delta\sigma$. If that is not the case, we discard the momentum, and start the process again by sampling the thermal momentum distribution. Finally, we choose a position for this particle

from a uniform distribution inside the surface element. The emission time is either τ_{sw} for bulk emission or τ_i for surface emission.

We go through all the elements of the particlisation surface, and generate in this way an ensemble of hadrons and resonances with well defined positions x_μ^i and momenta p_μ^i ⁹. We use this ensemble as the initial condition for the hadron cascade JAM, which we use to model the rest of the hadronic rescattering stage. This will be discussed in the next section.

The switching procedure, namely calculating the contribution to the particle distributions of *all* hadrons in the EoS from *all* hypersurface elements of the particlisation surface is numerically expensive. Among all the constituents of hybrid calculations—initial conditions, hydrodynamic simulation, switching process and hadronic cascade—it has been the bottleneck. In event-by-event hybrid simulations, this rather practical issue must be resolved to gain high statistics. In Appendix, we show in detail how to integrate the Cooper-Frye formula at less numerical costs [94].

2.4 Hadronic Cascade

Hadronic transport models can be used to describe the system in the low density hadronic phase of the evolution. In this work we use the microscopic transport model JAM [61, 95] for that purpose. In JAM, the trajectories of all hadrons and resonances, including those produced in resonance or string decays, are propagated along their classical trajectories like in other microscopic hadronic transport models such as RQMD [96, 97, 98, 99], and UrQMD [100, 101, 102]. To achieve a more sophisticated hadronic EoS, a mean field can be included within a framework of either Boltzmann-Uehling-Uhlenberck (BUU) model [103], or Quantum Molecular Dynamics (QMD) [104] approach. However, all results in this work are obtained without any mean field.

In the hadronic transport models, time evolution of system is described by a sum of incoherent binary hadron-hadron (hh) collisions. Two body collisions are realised by the closest distance approach: Two particles collide if their minimum distance b in the centre-of-mass (c.m.) frame of two colliding particles is smaller than the distance given by the geometrical interpretation of cross section:

$$b \leq \sqrt{\frac{\sigma_{\text{tot}}}{\pi}}, \quad (18)$$

where σ_{tot} denotes the total cross section at the energy \sqrt{s} . For two particles with their positions x_1 and x_2 , and four momenta p_1 and p_2 , the Lorentz invariant expression for impact parameter b is given by

$$b^2 = -(x_1 - x_2)^2 + \frac{[P \cdot (x_1 - x_2)]^2}{P^2} + \frac{[q \cdot (x_1 - x_2)]^2}{q^2}, \quad (19)$$

where $P = p_1 + p_2$, and $q = (p_1 - p_2) - \frac{[P \cdot (p_1 - p_2)]^2}{P^2} P$.

Inelastic hh collisions are modelled by resonance formation at low energies and by formation of colour strings at high energies. Threshold between resonance and string formation is set to about 4 GeV for baryon-baryon (BB), 3 GeV for meson-baryon (MB) and 2 GeV for meson-meson (MM) collisions. In the string formation process, we use the same distribution for the light-cone momentum transfer as in the HIJING model [105, 106, 107, 108]. Quark content of a string is assumed to be the same as the quark content of a corresponding hadron before excitation, as in the Fritiof model [109, 110].

The string decays are performed by the Lund string model [111, 112, 113]. Formation points and times for newly produced particles are determined from string decay by yo-yo formation point [114]. Formation time is about 1 fm/c with the string tension $\kappa = 1$ GeV/fm. In a baryon-like string, hadrons are produced by the quark-antiquark pair creation in the colour flux-tube between the quark

⁹Note that JAM allows different initial times t_i for each hadron. Thus hadrons enter the cascade and begin interacting at the time when they are emitted from the fluid.

and diquark. The antiquark from the pair creation is combined with the constituent quark in the in the string to form a first rank hadron. This hadron has an original constituent quark. We assign a formation time for the quarks from the quark-antiquark pair creation, but not for the original constituent quark. Thus, for example, the original constituent quark inside a newly formed meson can scatter, but with a reduced cross section $1/2\sigma_{MM}$. In general, leading hadrons which contain original constituent quarks can scatter during their formation time with cross sections reduced according to the additive quark model. The importance of this quark(diquark)-hadron interaction for the description of baryon stopping at CERN/SPS energies has been reported by Frankfurt group [97, 98, 99, 100, 101].

Experimentally well-known total and elastic cross sections, such as pp , pn , π^+p , K^-p and $\bar{p}p$, are parametrised in JAM. Cross sections involving the resonances are assumed to be the same as the corresponding stable hadron cross sections with the same quark content. For example, ρp cross section is the same as πp cross section.

In nucleon-nucleon scattering, nonstrange baryonic resonance excitation channels

$$NN \rightarrow NR, \quad NN \rightarrow RR, \quad (20)$$

where R means a nucleon resonance ($N(1440)$ - $N(1990)$) or a Δ resonance ($\Delta(1232)$ - $\Delta(1950)$) up to 2 GeV, are implemented. These resonance formation cross sections are fixed by pion production cross sections. Inverse processes such as $NR \rightarrow NN$ are computed employing the detailed balance formula where the finite width of the resonance is taken into account [91, 115, 116]. The lifetime of resonance, t , is randomly chosen according to an exponential decay law $\exp(-t\gamma\Gamma(M))$, where $\Gamma(M)$ is the energy-dependent width of the resonance and $\gamma = E/M$ is the Lorentz factor.

As an example of a meson-baryon scattering, the total cross section for the πN incoming channel is decomposed to

$$\sigma_{\text{tot}}(s) = \sigma_{\text{el}} + \sigma_{\text{ch}}(s) + \sigma_{\text{BW}}(s) + \sigma_{s-S}(s) + \sigma_{t-S}(s), \quad (21)$$

where σ_{el} , $\sigma_{\text{ch}}(s)$, $\sigma_{\text{BW}}(s)$, $\sigma_{s-S}(s)$, and $\sigma_{t-S}(s)$ denote the elastic, charge exchange, s -channel resonance formation, s -channel string formation and t -channel string formation cross section, respectively. Resonance formation cross section $\sigma_{\text{BW}}(s)$ is computed using the Breit-Wigner formula [98] by summing up cross sections to form resonances $R = N(1440)$ - $N(1990)$, $\Delta(1232)$ - $\Delta(1950)$, $\Lambda(1405)$ - $\Lambda(2110)$, $\Sigma(1385)$ - $\Sigma(2030)$ and $\Xi(1535)$ - $\Xi(2030)$.

In the case of $\bar{K}N$ incoming channel, we add t -channel hyperon production cross sections such as $K^-p \rightarrow \pi^0\Lambda$. The cross section of the inverse process $\pi Y \rightarrow \bar{K}N$, $Y = \Lambda, \Sigma$ is calculated using the detailed balance formula. The kaon-nucleon (KN) incoming channel does not have s -channel resonance formation, but t -channel resonance production processes $KN \leftrightarrow K\Delta$, $KN \leftrightarrow K(892)N$, $KN \leftrightarrow K(892)\Delta$ are included. The Breit-Wigner formula is used to evaluate the cross section for resonance production in meson-meson scatterings as well. Meson resonance states are included up to about 1800 MeV.

Additive quark model [97, 98, 101, 102] is used for the experimentally unknown cross sections such as an incoming channel involving multistrange hadrons, *e.g.* ϕ meson-pion scattering. Strangeness suppression factor is correctly included in the additive quark model: We have $\sigma_{\pi N} \approx 26$ mb and $\sigma_{KN} \approx 21$ mb consistent with the experimental data above resonance region.

2.5 Brief overview of hydro + hadronic cascade models

In this subsection, we briefly overview the current status of hydro + hadronic cascade model (sometimes called the ‘‘hybrid’’ model).

The very first work of hydro + cascade approaches was done by Dumitru *et al.* [117]. Motivation in this first study was to describe particle species dependence of freezeout process in a consistent manner. They solved hydrodynamic equations by assuming boost invariant longitudinal flow and cylindrical

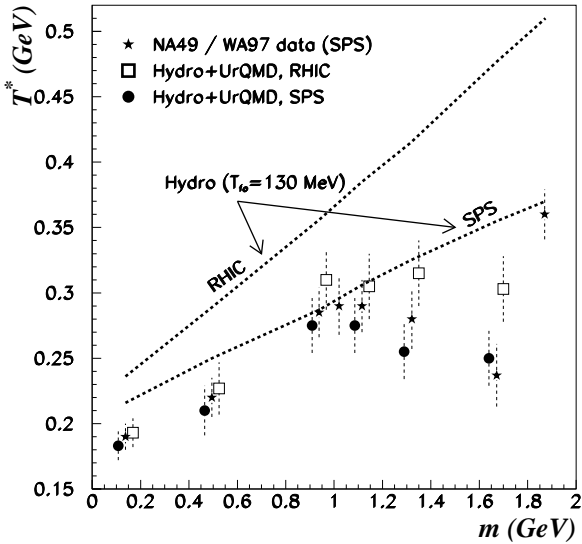


Figure 4: Inverse slopes of the m_T spectra for various strange and non-strange hadrons at midrapidity from the (1+1)-D hybrid model are compared with SPS data (star symbols) [120, 121]. Lines are results from pure hydrodynamic simulations with freezeout temperature $T_{fo} = 130$ MeV. Open squares and closed circles are results from the hybrid model at RHIC and SPS, respectively. Figure is taken from Ref. [117].

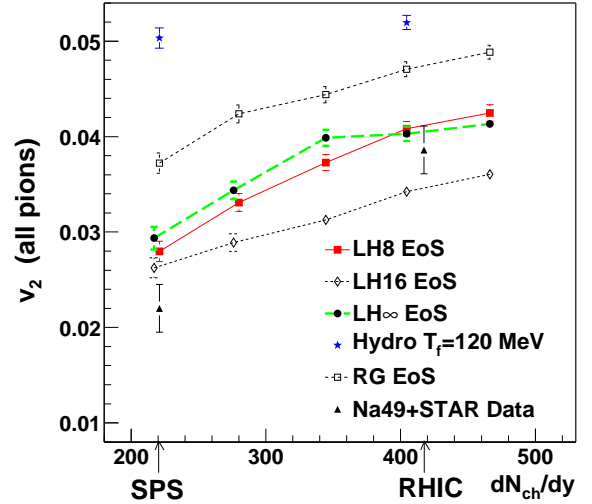


Figure 5: Elliptic flow parameters v_2 from four different equations of state as functions of the charged particle multiplicity from the (2+1)-D hybrid model is compared with SPS [122] and RHIC [123] data (triangle symbols). Impact parameter in the simulations is taken to be $b = 6$ fm. Star symbols are results from pure hydrodynamic simulations with freezeout temperature $T_f = 120$ MeV. Figure is taken from Ref. [19].

symmetry. As for the equation of state, a bag model which exhibits the first order phase transition was employed with $T_c = 160$ MeV. They switched description of dynamics from hydrodynamics to hadronic cascade at hadronisation. The m_T inverse slope parameters for various hadrons including multi-strange ones were calculated both in pure hydrodynamics (with $T_{fo} = 130$ MeV) and in the hydro + cascade approach as shown in Fig. 4. In pure hydrodynamics, it is known that the inverse slope parameter increases monotonically with the hadron mass. On the other hand, the slope parameter of multi strange hadrons from the hadron cascade approach are almost identical regardless of the mass difference [117], which is clearly different from a tendency of the pure hydrodynamic result mentioned above. They made a further analysis of kinetic freezeout in the subsequent papers [118, 119] within this hybrid approach.

A systematic analysis of SPS and RHIC data was done by Teaney *et al.* within a (2+1) dimensional hydro + cascade model [19, 20], where an event generator, RQMD, was employed for the hadronic cascade model. The importance of hadronic dissipation in interpreting the elliptic flow data was first demonstrated in this study. In the SPS and RHIC energy regions, pure ideal hydrodynamics predicts $v_2/\epsilon \sim 0.2-0.25$ depending on the equation of state employed in the simulations. This is sometimes called “hydrodynamic limit”. Experimental data of v_2/ϵ increase with the transverse particle density $(1/S)dN_{ch}/d\eta$ [31], where S is the transverse area, and reach the “hydrodynamic limit” of ~ 0.2 in central collisions at the top RHIC energy. As mentioned, ideal hydrodynamics predicts roughly constant v_2/ϵ , and does not reproduce this data. On the other hand, as shown in Fig. 5, this monotonic increase is described by the hydro + RQMD model [19, 20] in which finite cross sections of hadronic interactions

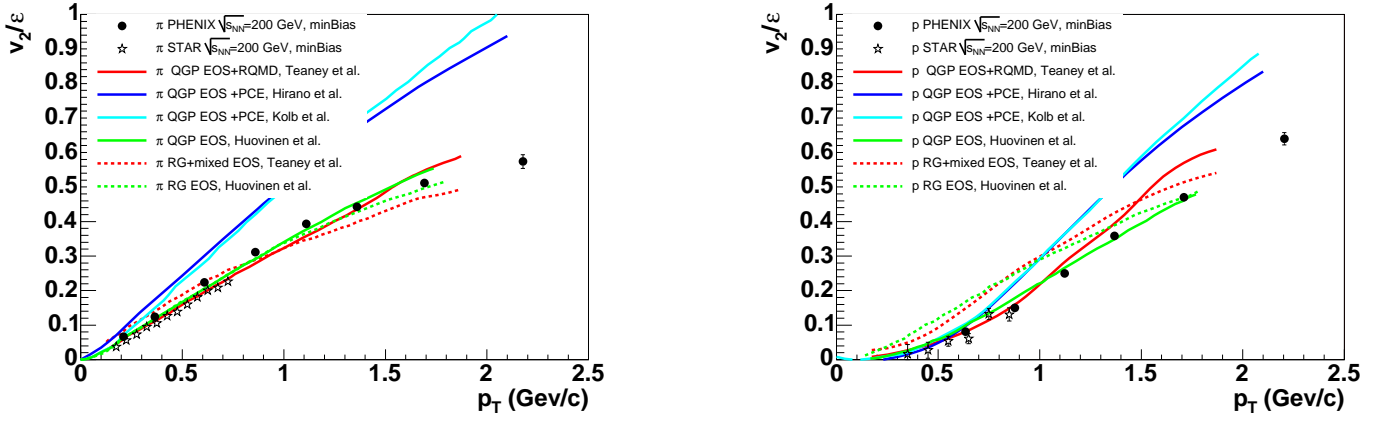


Figure 6: A compilation of hydrodynamic results as of year 2004. v_2/ϵ as a function of transverse momentum for pions (left) and for protons (right) from hydrodynamic models are compared with STAR and PHENIX minimum bias data. For details, see text and Ref. [124].

lead to dissipation and, consequently, integrated v_2 is considerably reduced in comparison with pure ideal hydrodynamic calculations.

Figure 6 shows a compilation of hydrodynamic results made by the PHENIX Collaboration [124] as of year 2004. Among several hydrodynamic approaches, it was only the hydro + RQMD model that reproduced particle identified spectra and $v_2(p_T)$ data at the same time. p_T spectra for pions and $v_2(p_T)$ for pions and protons are reproduced using ideal hydrodynamics where the fluid is in chemical equilibrium. However, such a model fails to reproduce the yield of protons since the freeze-out temperature required to fit the slopes of the p_T distributions is well below the temperature required to fit the observed particle ratios. To solve this issue, a partial chemical equilibrium (PCE) model [22] is employed. In this case, chemical freezeout is incorporated in the equation of state and the system is in kinetic but not in chemical equilibrium below a chemical freeze-out temperature. Such a model leads to successful reproduction of yields and spectra for pions and protons, but a slope of pion $v_2(p_T)$ is steeper than that of the data [22] as shown in Fig. 6 (left). The importance of the hadronic dissipative effects in simultaneous reproduction of yields, spectra and differential v_2 was discussed in detail later in Ref. [27].

Hirano *et al.* [125, 126] combined a fully (3+1) dimensional ideal hydrodynamics with a hadronic cascade model, JAM. Our integrated dynamical approach presented in this paper is based on this model. One of the advantages of the fully three dimensional simulations without assuming Bjorken scaling solution is to be able to obtain elliptic flow parameter as a function of pseudorapidity, $v_2(\eta)$. The charged hadron $v_2(\eta)$ has been measured by the PHOBOS Collaboration and it has a maximum at midrapidity and decreases as moving away from midrapidity [8, 9]. In a full three dimensional ideal hydrodynamic simulation with $T_{fo} = 100$ MeV [22], v_2 does not depend strongly on rapidity. Thus the main dependence on pseudorapidity comes from the Jacobian between rapidity and pseudorapidity [127], and the calculated $v_2(\eta)$ is flatter than the measured, whereas the three dimensional hybrid approach reproduces the observed $v_2(\eta)$ in the whole rapidity region in non-central collisions when the Glauber initial conditions are used [125], see Fig. 7. The space-time rapidity dependence of life time of the QGP fluid plays an important role in understanding the (pseudo-)rapidity dependence of v_2 since it takes time for the system to fully develop elliptic flow. Since $dN_{ch}/d\eta$ decreases with increasing η , initial entropy and, in turn, initial temperature decreases with increasing η_s . Consequently, the lifetime of the QGP also decreases with increasing η_s , and we may expect lower values of v_2 at large η_s if we evaluate v_2 immediately after hadronisation. In these calculations phase transition took place at $T_c = 170$ MeV,

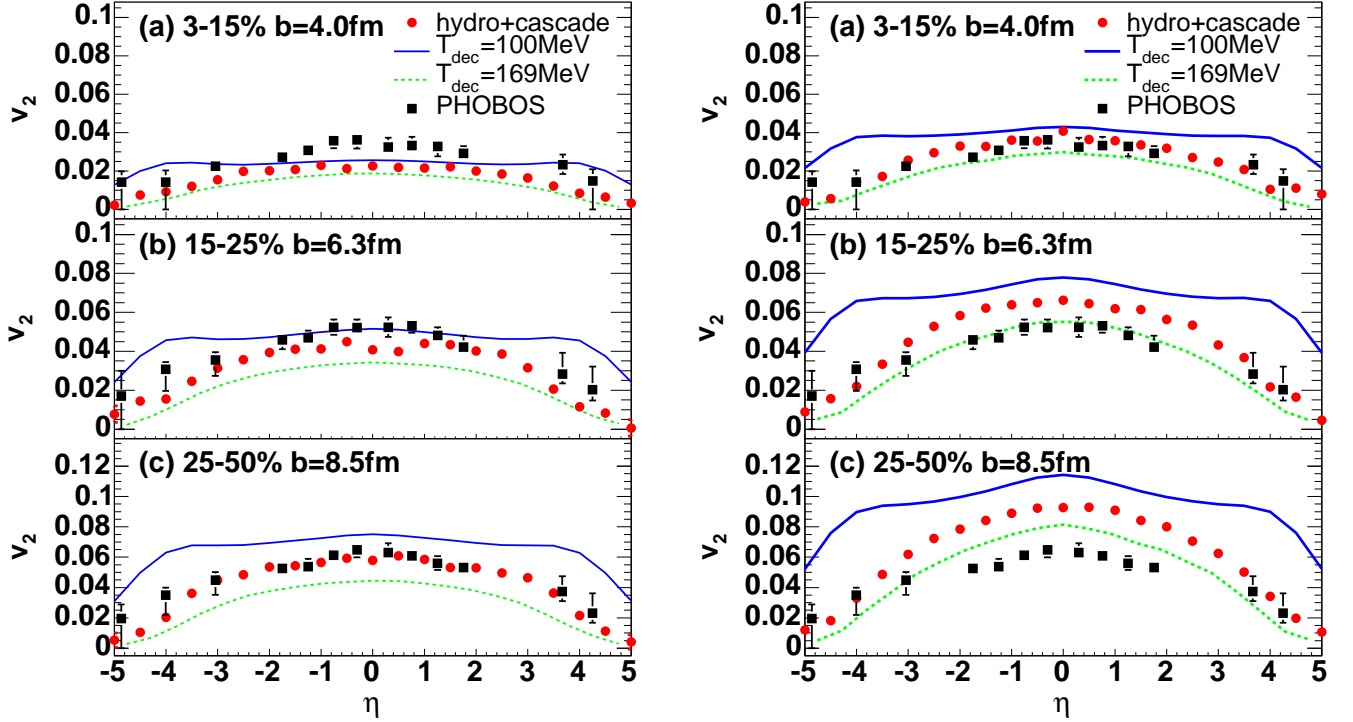


Figure 7: Pseudorapidity dependence of v_2 in 3-15%, 15-25% and 25-50% centralities from Glauber-BGK (left) and KLN (right) initial conditions are compared with the PHOBOS data [10]. Plots are results from the full 3D hybrid model. Solid and dashed curves are results from pure hydrodynamic simulations with freezeout (decoupling) temperature $T_{\text{dec}} = 100$ MeV and 169 MeV, respectively. Since the temperature of the boundary between the QGP and hadron phases in these calculations is $T = 170$ MeV, results with $T_{\text{dec}} = 169$ MeV correspond to the ones just after complete hadronisation. Figures are taken from Ref. [125].

and the evaluation of $v_2(\eta)$ on a $T = 169$ MeV surface leads to a shape peaking at midrapidity as expected, see Fig. 7, although the overall magnitude is less than the PHOBOS data [8, 9]. Additional generation of elliptic flow during the hadronic cascading stage fills this gap to reproduce the PHOBOS data. Compared with a purely ideal hydrodynamic treatment of the hadronic gas, the hadron cascade contains dissipative effects through finite mean free path. This indicates the importance of hadronic dissipative effects in particular in forward/backward regions.

It is interesting to note the deviations of the 3D hybrid model results from the PHOBOS data as well [125]. First, $v_2(\eta)$ from the full 3D hybrid model is smaller than the data at 3-15% centrality when the Glauber type initial conditions are employed (see top panel of Fig. 7 (left)), which implies the necessity of eccentricity fluctuations in the initial conditions. Second, the hybrid model with the KLN initialisation leads to larger v_2 than the data in semi-central to peripheral collisions (see Fig. 7 (right)), which leaves room for finite although very small QGP viscosity.

Another important finding from this full 3D hybrid model is a violation of mass ordering in differential elliptic flow parameter $v_2(p_T)$ [126]. Because of the interplay of thermal and collective motion, we expect that $m_1 < m_2 \Rightarrow v_2(p_T, m_1) > v_2(p_T, m_2)$ [18]. This mass ordering, however, holds only for particles frozen out in the same temperature having the same collective flow velocity. We expect that particles like ϕ mesons, which have very small cross sections and thus hardly rescatter, freeze-out

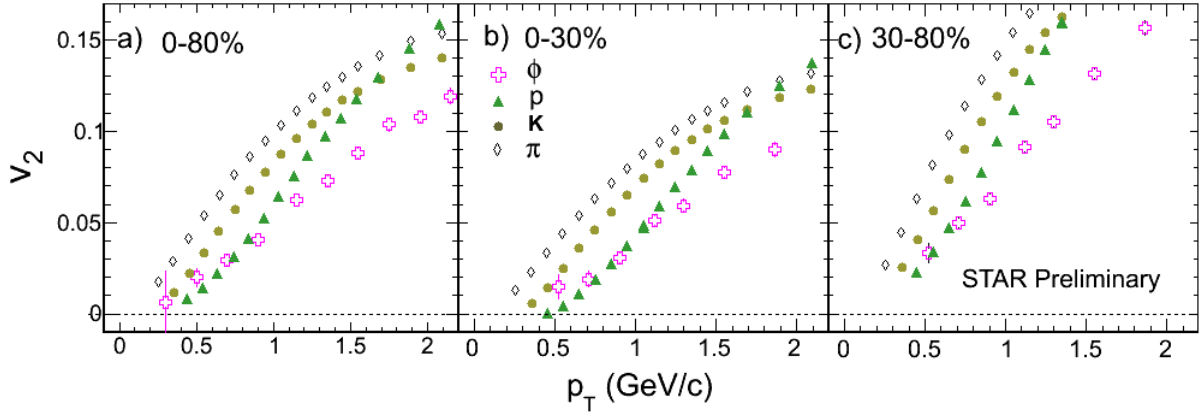


Figure 8: Transverse momentum dependence of particle identified elliptic flow parameters in 0-80%, 0-30% and 30-80% centrality from STAR Collaboration. Violation of mass ordering is clearly seen below ~ 0.8 GeV/c in 0-30% centrality. Figures are taken from Ref. [128].

earlier. Such a particle's $v_2(p_T)$ would be typical for larger temperature and smaller flow velocity. For particles with mass around 1 GeV mass, like ϕ mesons, freezing out earlier would mean larger $v_2(p_T)$ at small p_T . The hybrid model calculations predicted this kind of behaviour for the ϕ meson [126], and this violation of mass ordering was recently confirmed by the STAR collaboration [128] (See also Fig. 8).

The ideas of the Frankfurt group's first work were taken over by Nonaka and Bass [129] who used a fully three dimensional ideal hydrodynamic model coupled to UrQMD. Similar reduction of v_2 in forward/backward rapidity regions as shown in Fig. 7 was found in their results as well. Hadronic rescattering effects are seen in Fig. 9 as shifts of the peaks of freeze-out time distributions from ~ 10 fm/c to ~ 18 fm/c. The effect is similar for pions and kaons.

Petersen *et al.* combined full three dimensional ideal hydrodynamics in the Cartesian coordinate with UrQMD [93, 130, 131, 132, 133, 134, 135]. This is the first hybrid simulation on an event-by-event basis, which will be discussed later. One of the distinct features of this model is to employ isochronous particlisation when energy density of all fluid elements drops below 5 times ground state energy density (~ 730 MeV/fm³). They also discussed all fluid elements in one transverse slice rather than the whole region dropping below this value as an alternative criterion [130]. By using this (called gradual freezeout), one can take account of time dilatation in the forward rapidity region where the fluid moves faster in the Cartesian coordinate. An advantage of this method is to be able to avoid negative contribution in the Cooper-Frye formula since the hypersurface element is always time-like vector $d\sigma^\mu = (d^3x, \mathbf{0})$ and $p^\mu d\sigma_\mu$ term in this formula is positive definite. On the other hand, it may happen that freezeout occurs in some fluid elements only when the temperature becomes very small ($T < 100$ MeV) and the system is already diluted sufficiently. In the context of hadronic rescattering effects, they mainly focused on collisions at SPS energies and lower and found that their hybrid model can nicely describe elliptic flow at those energies [93, 130, 131], see Fig. 10. Recently this model has been extended to allow isothermal or iso density particlisation as well [87].

Pratt and Vredevogd [136] were the first to develop a hybrid model based on viscous hydrodynamics. Their goal was to understand femtosopic observables at RHIC, and they assumed radial symmetry and boost invariance both in hydrodynamical calculation and hadron cascade. In their model particlisation happens at a switching energy density $e_{sw} = 400$ MeV/fm³ instead of a constant temperature. They kept information about particlisation hypersurface and a hadron which returns to the interior of the

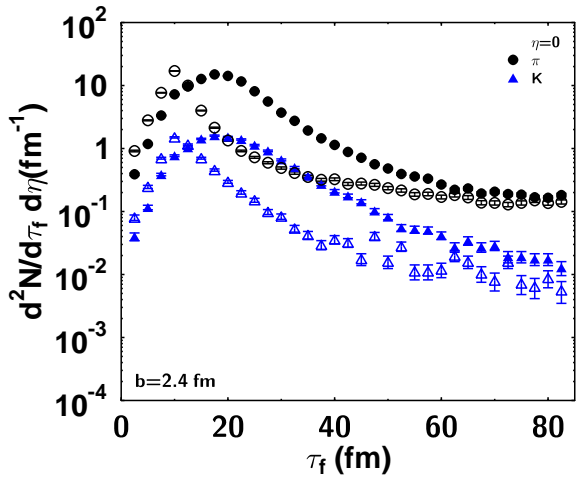


Figure 9: Freezeout-time distribution for pions (circles) and kaons (triangles) at an impact parameter $b = 2.4$ fm at the RHIC energy. Open (Closed) symbols correspond to results without (with) hadronic rescatterings. Figure is taken from Ref. [129].

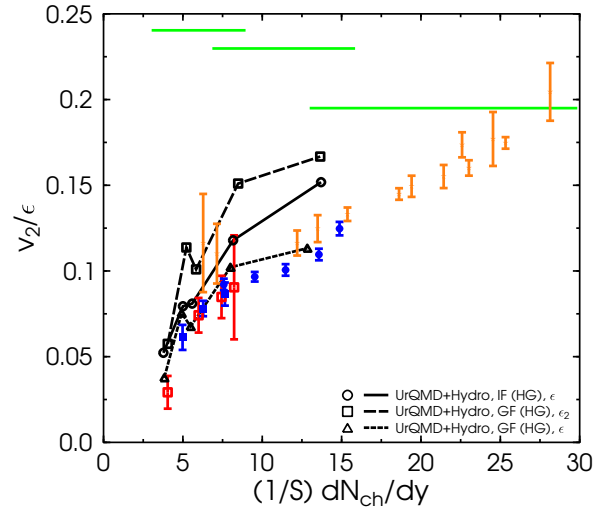


Figure 10: v_2/ϵ as a function of transverse density $(1/S)dN_{ch}/dy$ from a full 3D hybrid model is compared with experimental data at AGS, SPS and RHIC energies. Results with isochronous freezeout and gradual freezeout are shown as open circles and triangles, respectively. Results with gradual freezeout using event-by-event ϵ averaged over many events is shown as open squares. Figure is taken from Ref. [130].

surface ($e > e_{sw}$) during the cascade description is deleted from simulations. This would correspond to negative contribution to the Cooper-Frye formula. According to their estimation, a percentage of the absorbed particles is only about one percent. Fig. 11 shows positions of last interaction points for pions with $p_x = 300$, $p_y = 0$ MeV/c. Modestly positive correlation between the outward position and the emission time is seen, which would result in R_{out}/R_{side} to be close to unity.

Werner *et al.* combined an event generator, EPOS, full (3+1) dimensional ideal hydrodynamics and an hadronic cascade, UrQMD [137, 138, 139, 140]. In addition to nuclear collisions, they also applied their hybrid model to proton-proton collisions at the LHC energies. They concluded there exists collective flow even in pp collisions. Their results on ridge phenomenon will be discussed later in Sec. 2.7.

Detailed analyses of elliptic flow parameters based on a (2+1) dimensional hybrid model combining viscous hydrodynamics with UrQMD have been made by Song *et al.* [85, 141, 142, 143]. They mainly focused on extraction of η/s from a comparison of v_2/ϵ results with data and found η/s is not larger than twice the conjectured minimum bound, $1/4\pi$ [144] (See Fig. 12). From a hybrid model viewpoint, a systematic analysis of switching temperature dependence was made. They concluded that there exists no safe window of temperature below $T_{ch} = 165$ MeV to switch from viscous hydrodynamics to UrQMD [85]. This means that below 165 MeV UrQMD describes expanding matter far from equilibrium. On the other hand they did not test switching temperatures larger than 165 MeV, and thus it is not possible to say whether a temperature range exists in their model where the exact value of the switching temperature does not affect the results.

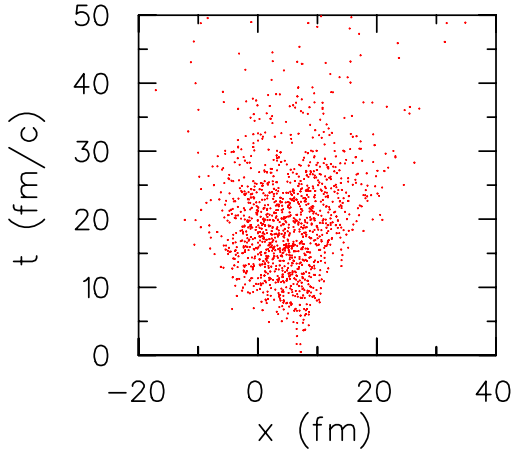


Figure 11: Positions of last interaction points for pions with $p_x = 300$, $p_y = 0$ MeV/c. Figure is taken from Ref. [136].

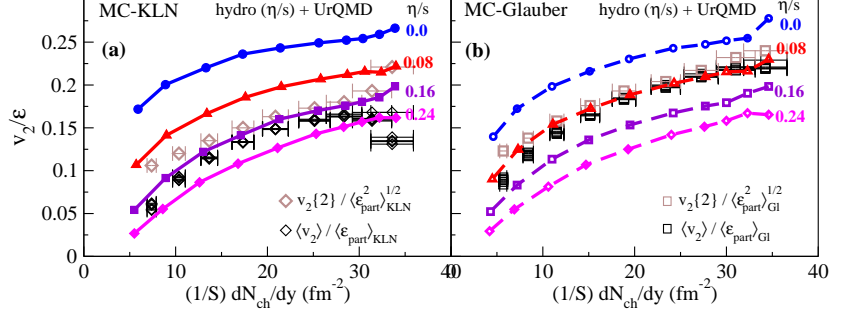


Figure 12: Comparison of v_2/ϵ vs. $(1/S)(dN_{ch}/dy)$ curves with experimental data from the STAR Collaboration. (a) the MC-KLN model and (b) the MC-Glauber model. Figures are taken from Ref. [141].

The χ^2 -fitting to spectra, v_2 and HBT radii in 0-10% central collisions at the RHIC energy was done by Soltz *et al.* using (2+1) dimensional viscous hydrodynamic simulations combined with the UrQMD cascade code [145]. Although the fit was done to a relatively small number of data sets, they were able to exclude two sets of initial conditions, namely N_{part} density without pre-equilibrium flow and N_{coll} density with pre-equilibrium flow, and to constrain initial temperature and the ratio of shear viscosity to entropy density for the other two sets of initial conditions, N_{part} density with pre-equilibrium flow and N_{coll} density without pre-equilibrium flow.

The simultaneous implementation of full three dimensionality, viscosity, hadronic cascade and event-by-event initialisation was first made by Ryu *et al.* [146]. Their results are preliminary at the moment, since they do not take into account the dissipative corrections to particle distributions at particlisation, and the statistics in their calculations is so far limited leading to large statistical error bars. Nevertheless, this is one of the promising approaches to investigate the transport properties of the QGP.

Table 1 summarises the current hydro + cascade models by focusing on the cascade model and the switching temperature.

2.6 Initial Conditions

The results of hydrodynamic calculations depend strongly on initial conditions since hydrodynamics requires solving initial value problems of partial differential equations. In principle one should obtain the initial conditions for hydrodynamic evolution by solving the non-equilibrium evolution of the matter created in the primary collision of nuclei, but unfortunately this is one of the outstanding problems in heavy-ion physics. Therefore we skip the description of how the matter equilibrates, and rely on models assuming that the matter has equilibrated, and that the densities are given by the density of produced gluons immediately after the primary collision (MC-KLN) or by the density of participating nucleons or binary collisions (MC-Glauber). Due to the lack of models, it is very difficult to quantify how pre-equilibrium dynamics would affect the interpretation of data and our understanding of the initial state of hydrodynamical evolution. It has been argued that flow built up during thermalisation would strongly affect the femtosopic data [136], but so far we do not know the mechanism creating pre-equilibrium flow, and thus do not know how large it could be. As well, it has been argued that the pre-equilibrium processes affect the granularity of the initial state in event-by-event calculations [85],

Table 1: Current status of the hydro + cascade models.

Authors and References	Hadronic Cascade	Hydrodynamics	T_{sw} [MeV]
Bass <i>et al.</i> [117, 118, 119]	UrQMD	(1+1)-D ideal	160
Teaney <i>et al.</i> [19, 20]	RQMD	(2+1)-D ideal	160
Hirano <i>et al.</i> [125, 126]	JAM	(3+1)-D ideal	169, 155
Nonaka and Bass [129]	UrQMD	(3+1)-D ideal	150
Petersen <i>et al.</i> [93, 130, 131, 132, 133, 134, 135]	UrQMD	(3+1)-D ideal	*1
Pratt and Vredevogd [136]	*2	(1+1)-D viscous	*3
Werner <i>et al.</i> [137, 138, 139, 140]	UrQMD	(3+1)-D ideal	166
Song <i>et al.</i> [141, 142, 85, 143]	UrQMD	(2+1)-D viscous	165*4
Soltz <i>et al.</i> [145]	UrQMD	(2+1)-D viscous	165
Ryu <i>et al.</i> [146]	UrQMD	(3+1)-D viscous	170

*1 Switching energy density is taken to be ~ 730 MeV/fm³.

*2 A rather simple hadronic cascade model is employed here [136].

*3 Switching energy density is taken to be 400 MeV/fm³.

*4 Sensitivity of the results to the value of T_{sw} is also investigated.

but we cannot calculate how large this smearing effect should be.

The Glauber model [28, 29, 30] has been widely used to fix the initial conditions of hydrodynamic simulations. In the various implementations of Glauber model, one either initialises the energy or entropy density, and assumes it to be proportional to the number density of participants, binary collisions, or some combination of those two [14, 77]. On the other hand, one expects highly coherent dense gluon system, called colour glass condensate (CGC) [48, 49, 50], to appear in high energy hadronic and nuclear collisions. One may describe the dynamics of gluon fields before local equilibration by solving classical Yang-Mills equation [147, 148, 149, 150, 151, 152, 153, 154]. The k_T -factorisation formulation is widely used to compute the inclusive cross section for produced gluons [155, 156, 157, 158, 159, 160, 161, 162, 163, 164, 165, 166, 167, 168, 169, 170] in hadronic collisions. Here we shall employ the Monte-Carlo implementations of k_T -factorisation formulation (MC-KLN) [171, 172, 173] and Glauber model (MC-Glauber) [28, 29, 30] to obtain initial conditions of hydrodynamical simulations. These Monte-Carlo approaches include fluctuations of the positions of nucleons inside colliding nuclei, which allows us to generate a set of initial conditions which fluctuate event-by-event. We do not include fluctuations of energy deposition/entropy generation per collisions [174], which results in negative binomial distribution of multiplicity [133, 166, 167, 175], since rapidity dependence of this kind of fluctuation is not known well.

In MC-Glauber model, for each event the positions of nucleons inside the two colliding nuclei are randomly sampled according to a nuclear density distribution (*e.g.*, Woods-Saxon function). One of the nuclei, and nucleons within, is shifted by a randomly-chosen impact parameter b with probability bdb . A nucleon-nucleon collision is assumed to take place if their distance d in the transverse plane orthogonal to the beam axis fulfils the condition

$$d \leq \sqrt{\frac{\sigma_{\text{in}}(\sqrt{s})}{\pi}}, \quad (22)$$

where $\sigma_{\text{in}}(\sqrt{s})$ denotes the inelastic nucleon-nucleon cross section at the c.m. energy \sqrt{s} . Incident energy dependent total pp cross section is parametrised based on Regge theory, which parameters have been determined by the Particle Data Group [176]:

$$\sigma_{\text{tot}}(\sqrt{s}) = Xs^\epsilon + Ys^{-\eta} \quad (23)$$

with $X = 22$, $Y = 56.1$, $\epsilon = 0.079$ and $\eta = 0.46$ for pp collision. Elastic cross section is computed using PYTHIA parametrisation [113, 177, 178]:

$$\sigma_{\text{el}} = \frac{\sigma_{\text{tot}}^2}{16\pi B_{\text{el}}(s)}, \quad B_{\text{el}}(s) = 4b_p + 4s^{0.0808} - 4.2 \text{ (GeV}^{-2}\text{)}, \quad (24)$$

where $b_p = 2.3$. This parametrisation leads to the following values for the inelastic cross section: $\sigma_{\text{in}} = \sigma_{\text{tot}} - \sigma_{\text{el}} = 39.53, 41.94$ and 61.36 mb at $\sqrt{s} = 130, 200$ and 2760 GeV, respectively.

It should be noted that the standard Woods-Saxon parameters shown in, *e.g.*, Ref. [179] cannot be directly used to distribute nucleons inside a nucleus because of the finite interaction range in our approach. We need to modify nuclear density parameters so that a convolution of nucleon profiles leads to the measured Woods-Saxon profile [57]:

$$\rho(\vec{x}) = \int \Delta(\vec{x} - \vec{x}_0) \rho_{\text{WS}}(\vec{x}_0) d^3x_0, \quad (25)$$

$$\Delta(\vec{x} - \vec{x}_0) = \frac{\theta(r_N - |\vec{x} - \vec{x}_0|)}{V_N}, \quad (26)$$

$$V_N = \frac{4\pi r_N^3}{3}, \quad r_N = \sqrt{\frac{\sigma_{NN}^{\text{in}}}{\pi}}, \quad \rho_{\text{WS}} = \frac{\rho_0}{\exp\left(\frac{r - r_0}{\delta r}\right) + 1}. \quad (27)$$

Figure 13 shows the standard Woods-Saxon profile (dashed) and the nuclear density profile taking

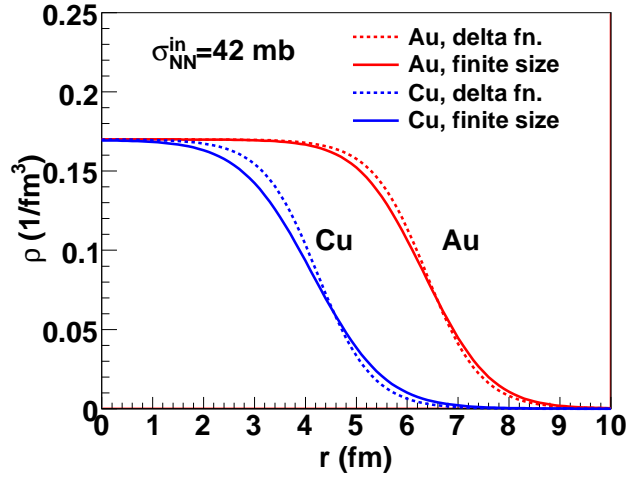


Figure 13: Nuclear density as a function of nuclear radius. Solid lines show nuclear density distribution for gold and copper nuclei in which a finite nucleon profile is implemented and positions of nucleons are sampled according to the Woods-Saxon distribution with default parameter sets. Dashed lines show the Woods-Saxon distribution with default parameter sets.

into account finite interaction ranges above but keeping the standard Woods-Saxon parameters (solid). In both gold and copper nuclei, the finite nucleon profile in Eq. (26) makes the nuclear surface more diffused if one uses the standard Woods-Saxon parameters to distribute nucleons in a nucleus. Without adjustment of the Woods-Saxon parameters for the finite nucleon profile, eccentricity becomes smaller by $\sim 10\%$ [55]. So we re-parametrise the distribution of nucleon position to reproduce the Woods-Saxon distribution with default parameters in Eq. (27) [29]. The adjustment of the Woods-Saxon parameters has not been considered in most of Monte Carlo approaches of the collisions including event generators If

one wants to discuss eccentricity and elliptic flow coefficient v_2 within $\sim 10\%$ accuracy, this adjustment should be taken into account. If the Gaussian form is used as a nucleon profile, one obtains better agreement with the measured nucleus charged distribution [180]. However, hard sphere form for the nucleon profile is sufficient for the discussion of v_2 in this work. In our MC-Glauber model, we find the default Woods-Saxon distribution is reproduced by larger radius parameter and smaller diffuseness parameter (*i.e.*, sharper boundary of a nucleus) than the default parameters: $\rho_0 = 0.1695$ (0.1686) fm^{-3} , $r_0 = 6.42$ (4.28) fm and $\delta r = 0.44$ (0.50) fm for a gold (copper) nucleus at $\sqrt{s_{NN}} = 200$ GeV and $\rho_0 = 0.161$ fm^{-3} , $r_0 = 6.68$ fm and $\delta r = 0.38$ for a lead nucleus at $\sqrt{s_{NN}} = 2.76$ TeV. In Ref. [180], one finds the parametrisation in the case of Gaussian shape for nucleons. This kind of effect exists in almost all Monte Carlo approaches to the collisions, including event generators. If one wants to discuss eccentricity and elliptic flow coefficient v_2 within $\sim 10\%$ accuracy, this effect should be taken into account. We also calculate initial entropy distribution in U+U collisions at $\sqrt{s_{NN}} = 200$ GeV by changing the nuclear density from gold to uranium. To take account of the prolate deformation of uranium nuclei, we parametrise the radius parameter in the Woods-Saxon distribution as

$$R(\theta, \phi) = r_0 (1 + \beta_2 Y_{20}(\theta, \phi) + \beta_4 Y_{40}(\theta, \phi)), \quad (28)$$

where Y_{lm} is the spherical harmonic function, $r_0 = 6.86$ fm, $\beta_2 = 0.28$ and $\beta_4 = 0.093$ [181]. Note that to account of the finite interaction range of nucleons in the Monte Carlo approach, we have again adjusted R_0 above and the diffuseness parameter $\delta r = 0.44$ fm and the saturation density $\rho_0 = 0.166$ fm^{-3} to retain the nuclear density as in the original Woods-Saxon distribution [57]. We also take into account that colliding uranium nuclei are randomly oriented in each event.

Next, we compute particle production at each grid point in the transverse plane. In the MC-Glauber approach, we assume that the initial entropy profile in the transverse plane is proportional to a linear combination of the number density of participants and that of binary collisions:

$$s_0(\mathbf{r}_\perp) \equiv \left. \frac{dS}{\tau_0 d^2 r_\perp d\eta_s} \right|_{\eta_s=0} = \frac{C}{\tau_0} \left(\frac{1-\alpha}{2} \rho_{\text{part}}(\mathbf{r}_\perp) + \alpha \rho_{\text{coll}}(\mathbf{r}_\perp) \right), \quad (29)$$

where $\tau_0 = 0.6$ fm/ c is a typical initial time for the hydrodynamical simulation. Parameters $C = 15.0$ and $\alpha = 0.18$ have been fixed through comparison with the centrality dependence of p_T spectra in Au+Au collisions at RHIC [67]. At the LHC energy, $C = 41.4$ and $\alpha = 0.08$ are chosen [54] so that we reproduce the ALICE data on centrality dependence of multiplicity in Pb+Pb collisions at $\sqrt{s_{NN}} = 2.76$ TeV [182, 183, 184].

The participant density, $\rho_{\text{part}}(\mathbf{r}_\perp)$, and the number density of binary collisions, $\rho_{\text{coll}}(\mathbf{r}_\perp)$, in Eq. (29) are obtained from the previously described positions of nucleons, and the criterion for their interaction, Eq. (22). At each grid point, the participant density is the sum of the number of those nucleons in both nuclei, which scatter within the radius $r_0 = \sqrt{\sigma_{\text{in}}/\pi}$ around the gridpoint, divided by the area σ_{in} :

$$\rho_{\text{part}}(\mathbf{r}_\perp) = \rho_A(\mathbf{r}_\perp) + \rho_B(\mathbf{r}_\perp) = \frac{N_{A,w}(\mathbf{r}_\perp) + N_{B,w}(\mathbf{r}_\perp)}{\sigma_{\text{in}}}, \quad (30)$$

Similarly, the density of the number of binary collisions at each grid point is obtained by counting the number of binary collisions N_{coll} within the area σ_{in} , where the position of a binary collision is assumed to be the average position of the two colliding nucleons:

$$\rho_{\text{coll}}(\mathbf{r}_\perp) = \frac{N_{\text{coll}}(\mathbf{r}_\perp)}{\sigma_{\text{in}}}. \quad (31)$$

which may be also obtained by the expression $\rho_A(\mathbf{r}_\perp)\rho_B(\mathbf{r}_\perp)\sigma_{\text{in}}$.

Note that we calculate the eccentricity of the initial state based on the densities defined above, whereas in the PHOBOS MC-Glauber model [28, 29, 30], eccentricity is computed based on the actual

positions of point-like particles. The conversion of positions to densities causes an additional smearing over the region σ_{in} [44, 185]. Therefore the eccentricities in our calculations are smaller than eccentricities in the PHOBOS MC-Glauber model. In the literature the conversion of positions to densities is often done by replacing each position by a Gaussian density profile [93, 212, 219]. Such a procedure again leads to slightly different eccentricities.

In the Monte-Carlo KLN (MC-KLN) model [171, 172, 173], the number distribution of gluon production at each transverse grid is given by the k_T -factorisation formula [156, 157, 158]

$$\begin{aligned} \frac{dN_g}{d^2r_{\perp} dy} &= \kappa \frac{4N_c}{N_c^2 - 1} \int \frac{d^2p_{\perp}}{p_{\perp}^2} \int \frac{d^2k_{\perp}}{4} \alpha_s(Q^2) \\ &\times \phi_A(x_1, (\mathbf{p}_{\perp} + \mathbf{k}_{\perp})^2/4) \phi_B(x_2, (\mathbf{p}_{\perp} - \mathbf{k}_{\perp})^2/4) , \end{aligned} \quad (32)$$

with $N_c = 3$ the number of colours. Here, p_{\perp} and y denote the transverse momentum and the rapidity of the produced gluons, respectively. The light-cone momentum fractions of the colliding gluon ladders are then given by $x_{1,2} = p_{\perp} \exp(\pm y) / \sqrt{s_{NN}}$, where $\sqrt{s_{NN}}$ denotes the centre of mass energy. Running coupling $\alpha_s(Q^2)$ is evaluated at the scale $Q^2 = \max((\mathbf{p}_{\perp} - \mathbf{k}_{\perp})^2/4, (\mathbf{p}_{\perp} + \mathbf{k}_{\perp})^2/4)$. An overall normalisation factor κ is chosen to fit the multiplicity data in most central Au+Au collisions at RHIC. In the MC-KLN model, saturation momentum is parametrised by assuming that the saturation momentum squared is 2 GeV² at $x = 0.01$ in Au+Au collisions at $b = 0$ fm at RHIC where $\rho_{\text{part}} = 3.06 \text{ fm}^{-2}$ [156, 157, 158, 186]:

$$Q_{s,A}^2(x; \mathbf{r}_{\perp}) = 2 \text{ GeV}^2 \frac{\rho_A(\mathbf{r}_{\perp})}{1.53 \text{ fm}^{-2}} \left(\frac{0.01}{x} \right)^{\lambda} . \quad (33)$$

λ is a free parameter which is expected to be in the range of $0.2 < \lambda < 0.3$ from Hadron Electron Ring Accelerator (HERA) global analysis for $x < 0.01$ [187, 188]. In MC-KLN, we assume the gluon distribution function as

$$\phi_A(x, k_{\perp}^2; \mathbf{r}_{\perp}) \sim \frac{1}{\alpha_s(Q_{s,A}^2)} \frac{Q_{s,A}^2}{\max(Q_{s,A}^2, k_{\perp}^2)} . \quad (34)$$

We assume that initial conditions of hydrodynamical simulations are obtained by identifying the gluons' momentum rapidity y with space-time rapidity η_s

$$s_0(\mathbf{r}_{\perp}) \propto \frac{dN}{\tau_0 d^2r_{\perp} d\eta_s} . \quad (35)$$

We note that gluon production itself also fluctuates [133, 166, 167, 175], but we do not take those fluctuations into account in our model.

To quantify the anisotropy of the initial distributions, we define the anisotropies ε_n , and the corresponding orientation angles Φ_n [34, 44]:

$$\varepsilon_n\{\text{PP}\} = \frac{|\langle \mathbf{r}_{\perp}^2 e^{in\varphi} \rangle_x|}{\langle \mathbf{r}_{\perp}^2 \rangle_x} \quad (36)$$

$$n\Phi_n = \arg\langle \mathbf{r}_{\perp}^2 e^{in\varphi} \rangle_x \quad (37)$$

where $\langle \dots \rangle_x$ represents a weighted average over the transverse plane at a fixed space-time rapidity, with the initial density distribution as a weight. Although one may take other definitions [132, 189, 190, 191, 192, 193], we restrict our discussion to Eqs. (36) and (37) throughout this paper. As for the initial density, we use the entropy density throughout this work. Here \mathbf{r}_{\perp} is the transverse two dimensional vector measured from the centre of mass defined by $\langle \mathbf{r}_{\perp} \rangle_x = \mathbf{0}$ and φ is its coordinate angle. For

example, the anisotropy ε_2 becomes

$$\varepsilon_2\{\text{PP}\} = \frac{\sqrt{\langle x_\perp^2 - y_\perp^2 \rangle_x^2 + 4\langle x_\perp y_\perp \rangle_x^2}}{\langle x_\perp^2 + y_\perp^2 \rangle_x}, \quad (38)$$

$$x_\perp = x - \langle x \rangle_x, \quad (39)$$

$$y_\perp = y - \langle y \rangle_x, \quad (40)$$

which is also known as the participant eccentricity $\varepsilon_{\text{part}}$ or eccentricity with respect to the participant plane. To keep our terminology consistent with the terminology in literature, we define participant plane as the plane spanned by a unit vector pointing to direction $\Phi_2 - \pi/2$, and the beam axis. Taking a real part of Eq. (36) instead of its absolute value, one obtains the anisotropy with respect to the reaction plane, also known as the standard eccentricity ε_{std} (although with an opposite sign),

$$\varepsilon_2\{\text{RP}\} = -\varepsilon_{\text{std}} = \frac{\Re\langle \mathbf{r}_\perp^2 e^{i2\varphi} \rangle_x}{\langle \mathbf{r}_\perp^2 \rangle_x} = \frac{\langle x_\perp^2 - y_\perp^2 \rangle_x}{\langle x_\perp^2 + y_\perp^2 \rangle_x}. \quad (41)$$

MC-KLN and MC-Glauber models create an ensemble of initial distributions for event-by-event calculations, but it is also possible to construct an averaged density profile which includes some effects of fluctuations. This is done by rotating each distribution by its orientation angle Φ_n around its centre of mass, shifting the distributions so that the origin of the coordinates is at its centre of mass, ($\langle x \rangle_x, \langle y \rangle_x$), and averaging over these shifted and rotated distributions. In the literature the required angle is often defined as in Ref. [194]:

$$\tan 2\psi_2 = \frac{2\sigma_{xy}}{\sigma_y^2 - \sigma_x^2}, \quad (42)$$

$$\sigma_x^2 = \langle x^2 \rangle_x - \langle x \rangle_x^2, \quad (43)$$

$$\sigma_y^2 = \langle y^2 \rangle_x - \langle y \rangle_x^2, \quad (44)$$

$$\sigma_{xy} = \langle xy \rangle_x - \langle x \rangle_x \langle y \rangle_x, \quad (45)$$

where the angle ψ_2 is related to the orientation angle Φ_2 defined in Eq. (37) as $\Phi_2 = -\psi_2$. As was described in the introduction, elliptic flow arises when the system expands preferentially along its participant plane. In this procedure the participant planes of various events are aligned and set equal to the reaction plane. That such an initial state contains some effects of eccentricity fluctuation even though the profile is smooth is manifested in the finite eccentricity even in most central collisions where the impact parameter is zero. We call this initialisation model ‘‘B’’. Compared with this, the procedure averaging over many initial distributions without shift or rotation corresponds to a conventional initialisation without the effect of eccentricity fluctuation and is called model ‘‘A’’. When we use the averaged initial conditions of models ‘‘A’’ and ‘‘B’’, called later the smooth initial profiles, we assume longitudinal boost invariance and calculate observables only at midrapidity. In particular, in the case of the MC-KLN model, we evaluate gluon production at midrapidity using Eq. (32), and assume it to be the same at all rapidities. In actual hydrodynamic simulations, we prepare the lattice in the longitudinal direction up to $\eta_s = 6$ and solve hydrodynamic equations with boost invariant initial conditions. We have checked that the boundary of the lattice does not affect the boost invariant solutions.

In models A and B centrality is defined using the number of events as a function of N_{part} . One can categorise the whole events into sub events from top 5%, 5-10% and so on according to N_{part} . In Table 2, we show the maximum and minimum numbers of participants for each centrality bin in Au+Au, U+U, Cu+Cu collisions at the RHIC energy and in Pb+Pb collisions at the LHC energy.

Figure 14 (left) shows the initial eccentricity with respect to participant plane (model ‘‘B’’) in Au+Au and U+U collisions at $\sqrt{s_{NN}} = 200$ GeV as a function of the number of participants. At each

Table 2: Centrality definition using N_{part} in Au+Au, U+U and Cu+Cu collisions at $\sqrt{s_{NN}} = 200$ GeV and in Pb+Pb collisions $\sqrt{s_{NN}} = 2.76$ TeV .

Centrality(%)	0-5	5-10	10-15	15-20	20-30	30-40	40-50	50-60	60-70	70-80
Au+Au $N_{\text{part,max}}$	394	327	279	237	202	144	99	65	39	21
Au+Au $N_{\text{part,min}}$	327	279	237	202	144	99	65	39	21	10
U+U $N_{\text{part,max}}$	476	389	330	281	239	170	117	77	46	25
U+U $N_{\text{part,min}}$	389	330	281	239	170	117	77	46	25	12
Cu+Cu $N_{\text{part,max}}$	126	102	88	75	65	47	33	22	14	9
Cu+Cu $N_{\text{part,min}}$	102	88	75	65	47	33	22	14	9	5
Pb+Pb $N_{\text{part,max}}$	416	356	305	261	223	161	112	74	46	25
Pb+Pb $N_{\text{part,min}}$	356	305	261	223	161	112	74	46	25	12

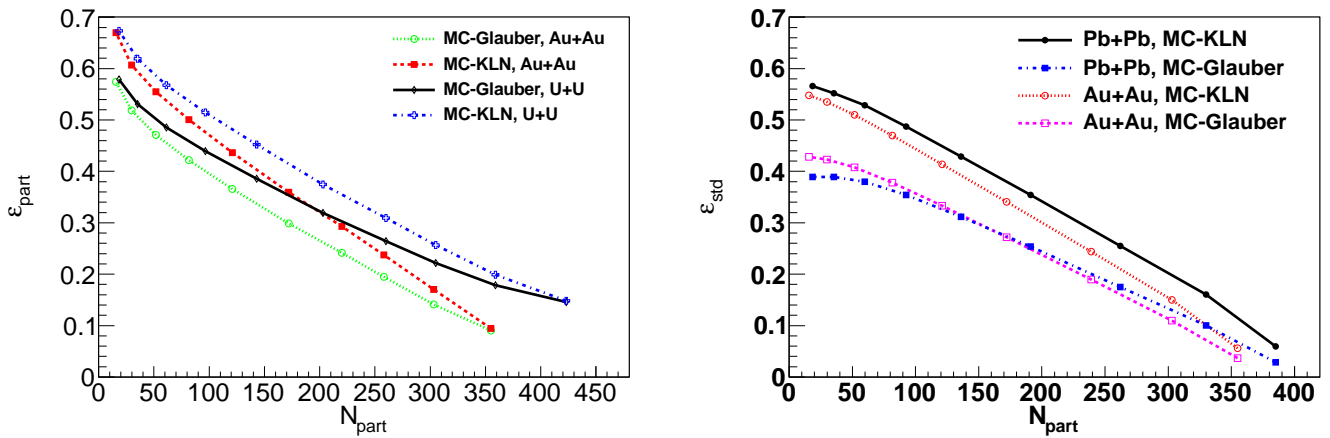


Figure 14: The second order anisotropy with respect to participant plane (model “B”) in Au+Au and U+U collisions at $\sqrt{s_{NN}}=200$ GeV (left) and with respect to reaction plane (model “A”) in Au+Au collisions at $\sqrt{s_{NN}}=200$ GeV and in Pb+Pb collisions at $\sqrt{s_{NN}}=2.76$ TeV (right). Results from the MC-KLN and MC-Glauber models are compared with each other. Figures are taken from Refs. [53, 54]

of the ten centrality bins the average eccentricity and the average number of participants $\langle N_{\text{part}} \rangle$ were calculated using both the MC-Glauber and the MC-KLN models. Since the eccentricity is measured in the participant plane, it is finite even in the very central (0-5%) Au+Au collisions. As previously known, the MC-KLN model leads to $\sim 20\text{-}30\%$ larger eccentricity than the MC-Glauber model except in the most central events [125, 159]. In most central 5% of U+U collisions eccentricity reaches 0.146 in the MC-Glauber model and 0.148 in the MC-KLN model. The eccentricity is larger in U+U than in Au+Au collisions. Due to the deformed shape of uranium nucleus, this holds not only at fixed number of participants, but also at fixed centrality. The difference, however, decreases with decreasing centrality, and there is almost no difference in the very peripheral events (70-80%).

Shown in Fig. 14 (right) is the initial eccentricity with respect to reaction plane (model “A”) as a function of N_{part} in Pb+Pb collisions at $\sqrt{s_{NN}} = 2.76$ TeV and in Au+Au collisions at $\sqrt{s_{NN}} = 200$ GeV. Again, the k_t -factorised formula of KLN model generates larger eccentricity than the Glauber model does [125, 159]. In the MC-KLN model, eccentricity in Pb+Pb collisions at $\sqrt{s_{NN}} = 2.76$ TeV is apparently larger than that in Au+Au collisions at $\sqrt{s_{NN}} = 200$ GeV when N_{part} is fixed. However, at a fixed centrality, the difference between them is very small [53]. On the other hand, in the MC-Glauber

model, eccentricity in Pb+Pb collisions at $\sqrt{s_{NN}} = 2.76$ TeV is slightly smaller than that in Au+Au collisions at $\sqrt{s_{NN}} = 200$ GeV for a fixed centrality.

This is due to the smearing process we use to obtain a smooth initial profile for hydrodynamic evolution [85]. As mentioned, we use the inelastic cross section in $p + p$ collisions, σ_{in} , when converting the positions of collision points to densities, and this effectively smears the distributions. This cross section is ~ 1.5 times larger at LHC than at RHIC, and thus the smearing area, $S = \sigma_{\text{in}}$ [55, 56], is also larger at LHC, and the eccentricity is reduced. Our smearing procedure also leads to a smaller eccentricity than the PHOBOS MC-Glauber model¹⁰. The effect of smearing is smaller in the MC-KLN initialisation, and we have checked that the eccentricity at LHC turns out to be essentially the same as at RHIC when the smearing area is the same.

Instead of shifting, rotating or averaging transverse profiles, we directly use each individual initial density given by these Monte-Carlo approaches to perform event-by-event hydrodynamic simulations. In these event-by-event calculations, we perform full three dimensional hydrodynamic simulations without assuming boost invariance. In the case of MC-KLN Eq. (32) provides the rapidity distribution of density as well. On the other hand, the Glauber model does not tell the longitudinal structure of the density distribution. Motivated by analyses in Refs. [195, 196], we parametrise initial entropy density distribution as [125]

$$\begin{aligned} s_0(\tau_0, \eta_s, \mathbf{r}_\perp) &= \frac{dS}{\tau_0 d\eta_s d^2 r_\perp} \\ &= \frac{C}{\tau_0} \theta(Y_b - |\eta_s|) f^{pp}(\eta_s) \left[\frac{1 - \alpha}{2} \left(\frac{Y_b - \eta_s}{Y_b} \rho_A(\mathbf{r}_\perp) + \frac{Y_b + \eta_s}{Y_b} \rho_B(\mathbf{r}_\perp) \right) + \alpha \rho_{\text{coll}}(\mathbf{r}_\perp) \right], \end{aligned} \quad (46)$$

where Y_b is the beam rapidity and f^{pp} is a parametrisation of the shape of rapidity distribution in pp collisions,

$$\begin{aligned} \frac{dS^{pp}}{d\eta_s} &= \int d^2 r_\perp \frac{dS^{pp}}{d\eta_s d^2 r_\perp} = C \theta(Y_b - |\eta_s|) f^{pp}(\eta_s) \\ &= C \theta(Y_b - |\eta_s|) \exp \left[-\theta(|\eta_s| - \Delta\eta) \frac{(|\eta_s| - \Delta\eta)^2}{\sigma_\eta^2} \right], \end{aligned} \quad (47)$$

where $\Delta\eta$ and σ_η are adjustable parameters. Equation (46) is designed so that the density is independent of the space-time rapidity η_s only around midrapidity when the densities of participating nucleons are the same in both nuclei, $\rho_A(\mathbf{r}_\perp) = \rho_B(\mathbf{r}_\perp)$. Equation (46) reduces to Eq. (29) when one plugs in $\eta_s = 0$. We call this parametrisation as the modified BGK model [125]. As mentioned, we do not consider fluctuation of particle production processes and, consequently, longitudinal profile becomes a smooth function. Therefore, there exists some correlation of particle production in the rapidity direction.

Initial parameters in the modified BGK model in Au+Au collisions at $\sqrt{s_{NN}} = 200$ GeV are chosen to reproduce $dN_{\text{ch}}/d\eta_s$ measured by PHOBOS Collaboration [197]. The resultant parameters are $\Delta\eta = 1.3$ and $\sigma_\eta = 2.1$. At the time of this writing, the measured pseudorapidity dependence of multiplicity in Pb+Pb collisions at $\sqrt{s_{NN}} = 2.76$ TeV is still preliminary. The parameters $\Delta\eta = 1.9$ and $\sigma_\eta = 3.2$ are chosen to give in central $0 < b < 5$ fm events an average $dN_{\text{ch}}/d\eta$ similar to the value obtained using the MC-KLN initialisation. Once the experimental data is finalised, we can adjust these parameters again.

Throughout this work, initial flow velocity is chosen as the Bjorken flow $u^\tau = 1$ and $u^x = u^y = u^{\eta_s} = 0$ [198]. In actual simulations, initial energy density is also needed. One calculates it from the initial entropy density utilising numerical table of EoS, $\epsilon = \epsilon(s)$. Note that we have neglected baryon density in our calculations.

¹⁰In the MC-Glauber model in the literature [28], one assumes δ function profile for each collision point in ρ_{part} distribution rather than a box-like profile in the present work.

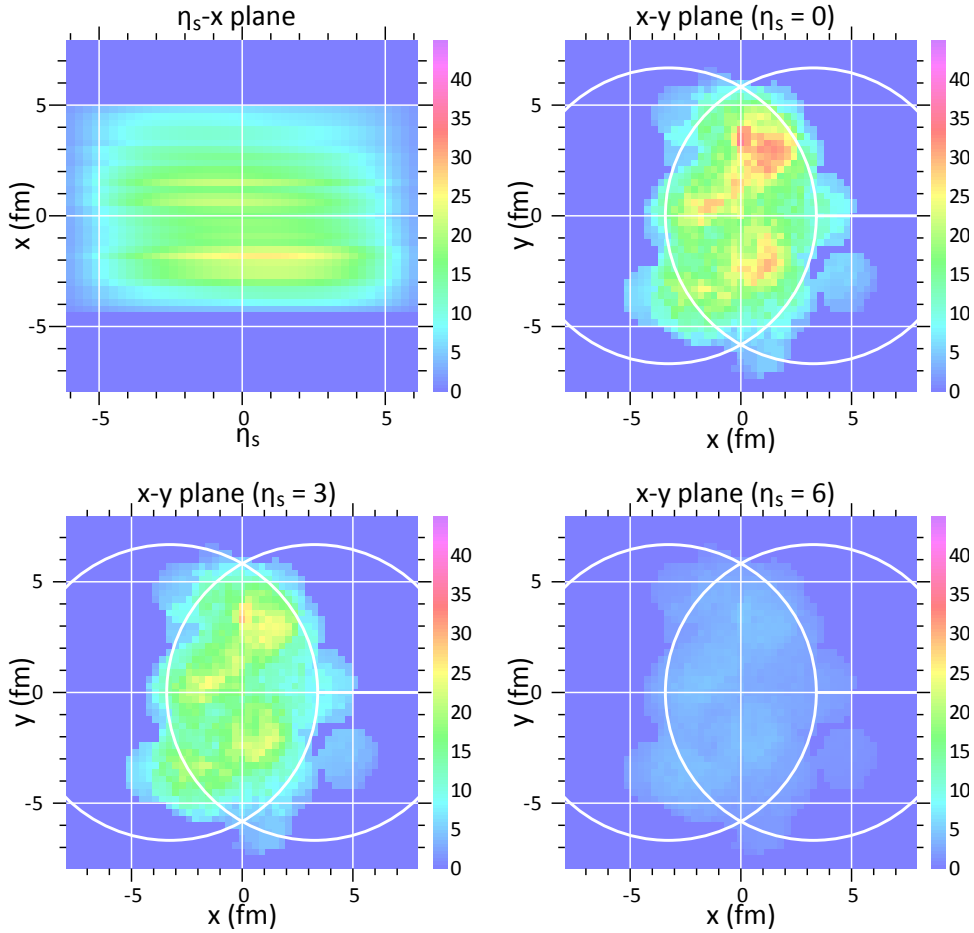


Figure 15: An example of initial condition in Pb+Pb collisions at $\sqrt{s_{NN}}=2.76$ TeV from the MC-KLN model. Initial entropy distribution (scaled down by 8.5) is shown in a plane at $y = \langle y \rangle_x$ (top-left), $\eta_s = 0$ (top-right), $\eta_s = 3$ (bottom-left) and $\eta_s = 6$ (bottom-right). Both circles with a radius $r_0 = 6.68$ fm represent a colliding nucleus.

Figures 15 and 16 show a sample of the initial profile in Pb+Pb collisions at $\sqrt{s_{NN}} = 2.76$ TeV from the MC-KLN model and the MC-Glauber model, respectively. Longitudinal streak-like structures are seen in $y = \langle y \rangle_x$ fm (top-left panel in both figures), where $\langle y \rangle_x$ has been averaged over space-time rapidity. This structure comes simply from smooth longitudinal profiles at the collision point in the transverse plane described in Eqs. (32) or (46). Due to this, similar transverse profiles are seen at all space-time rapidities: Hot spots are always located in the same position in the transverse plane.

Figure 17 (left) shows the centrality dependence of the average orientation angle $\cos(n\Phi_n)$. Harmonics with even n do not vanish, which is expected from an almond-like geometry of non-central collisions. The second and the sixth orientation angles negatively correlate with the reaction plane, whereas the fourth orientation angle shows positive correlation. On the other hand, $\langle \cos n\Phi_n \rangle$ for the odd n vanishes, which results from a fact that there is no correlation between $\Phi_n (n = 3, 5)$ and the reaction plane shown in Fig. 17 (right). In Fig. 17 (right) the number of events as a function of the absolute value of the orientation angle $|n\Phi_n|$ is shown for a sample of 10^5 minimum bias events. These events are binned according to the orientation angle of the initial state measured from the reaction plane. As clearly seen, $|2\Phi_2|$ has a prominent peak at π , which comes from a fact that initial profile looks like an almond shape elongated in the y -direction on average. Note that the angle Φ_2 thus gives the angle between the major

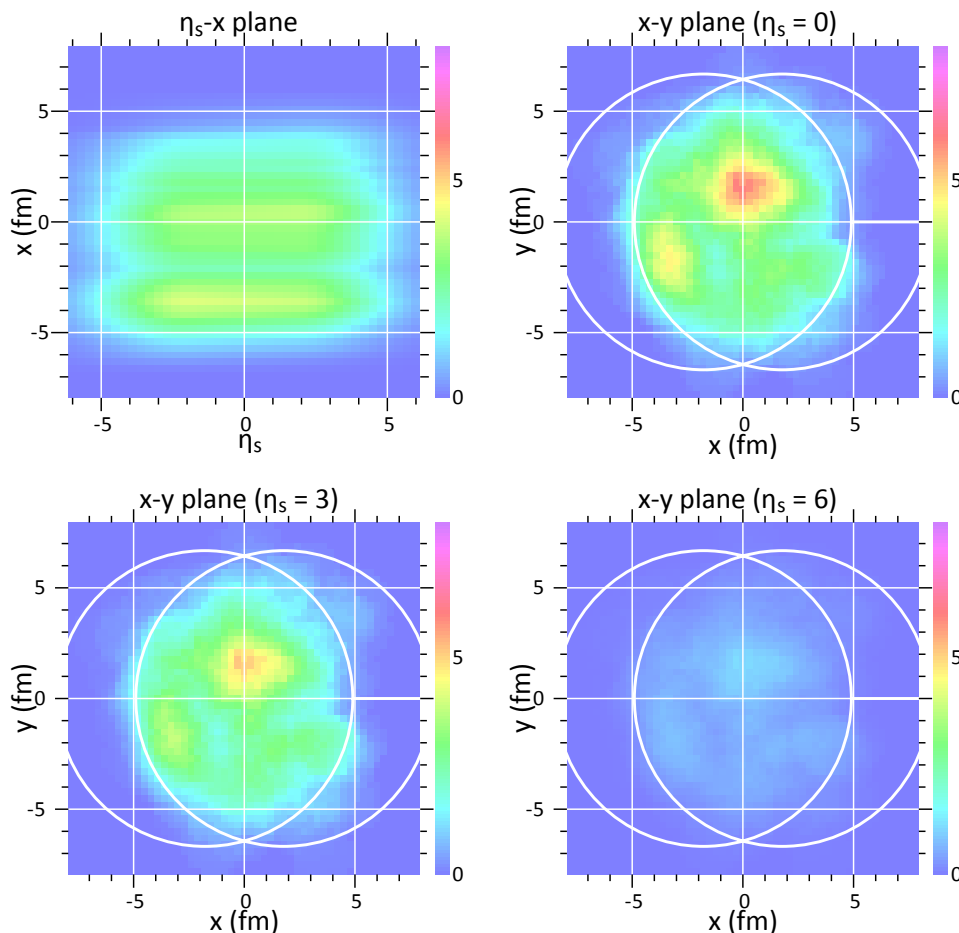


Figure 16: An example of initial condition in Pb+Pb collisions at $\sqrt{s_{NN}}=2.76$ TeV from the MC-Glauber model with an extension using the BGK model. Initial entropy distribution (scaled down by 25) is shown in a plane at $y = \langle y \rangle_x$ (top-left), $\eta_s = 0$ (top-right), $\eta_s = 3$ (bottom-left) and $\eta_s = 6$ (bottom-right). Both circles with a radius $r_0 = 6.68$ fm represent a colliding nucleus.

axis of the almond and the reaction plane. Other even harmonics, $4\Phi_4$ and $6\Phi_6$, have broad peaks at 0 and π , respectively. Orientation angles with odd n are randomly distributed due to absence of any correlation with respect to the reaction plane. The width of event distribution might be important in understanding the fluctuation of the anisotropies of the particle distribution, δv_n , although we postpone this study to a future work.

Figures 18 and 19 show space-time rapidity dependences of $\varepsilon_n\{\text{PP}\}$ and $\varepsilon_n\{\text{RP}\}$, respectively, using the MC-KLN model, and Figures 20 and 21 using the MC-Glauber model (extended in the longitudinal direction using the BGK model). The anisotropies ε_n are evaluated in 0-10% (left), 30-40% (middle) and 60-70% (right) centrality classes in Pb+Pb collisions at $\sqrt{s_{NN}} = 2.76$ TeV. Since the density profiles are smooth and have a streak-like structure in the longitudinal direction as shown in Figs. 15 and 16, $\varepsilon_n\{\text{PP}\}$ are almost independent of η_s . For MC-KLN initialization $\varepsilon_n\{\text{PP}\}$ for $n = 3, 5,$ and 6 are close to each other at all centralities, whereas the values differ for MC-Glauber initialization. This indicates different origin of fluctuations in these two models. If v_n was roughly proportional to $\varepsilon_n\{\text{PP}\}$, v_n would be independent of rapidity. However, it is not the case at least for $v_2(\eta)$ at RHIC. Even though ε_2 is almost independent of space-time rapidity [21], final v_2 has a broad peak at midrapidity due to relatively larger hadronic dissipative effects in forward/backward rapidity regions [125]. This

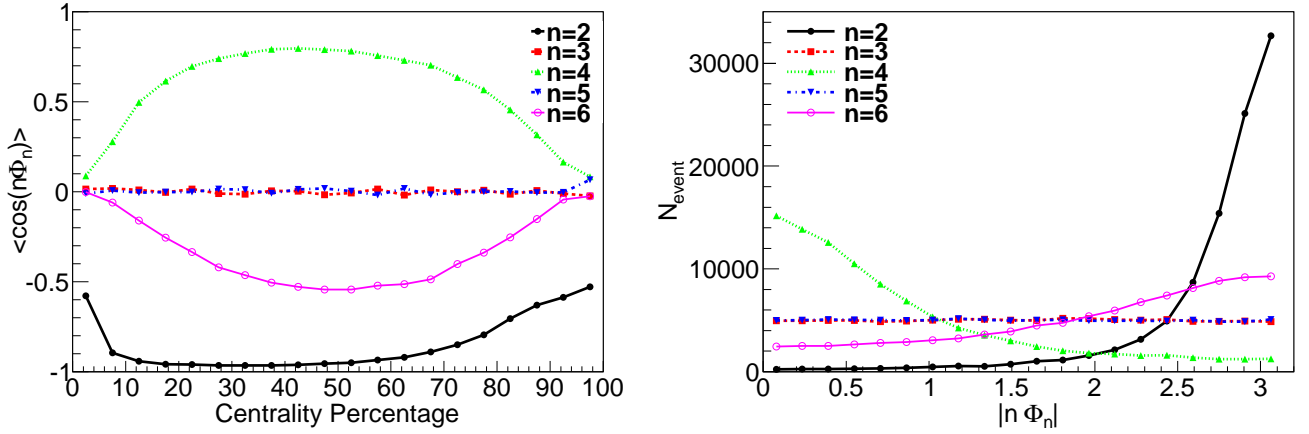


Figure 17: Centrality dependence of average orientation angle (left) and event distribution of orientation angle (right). The total number of events is 10^5 and the number of bins is 20.

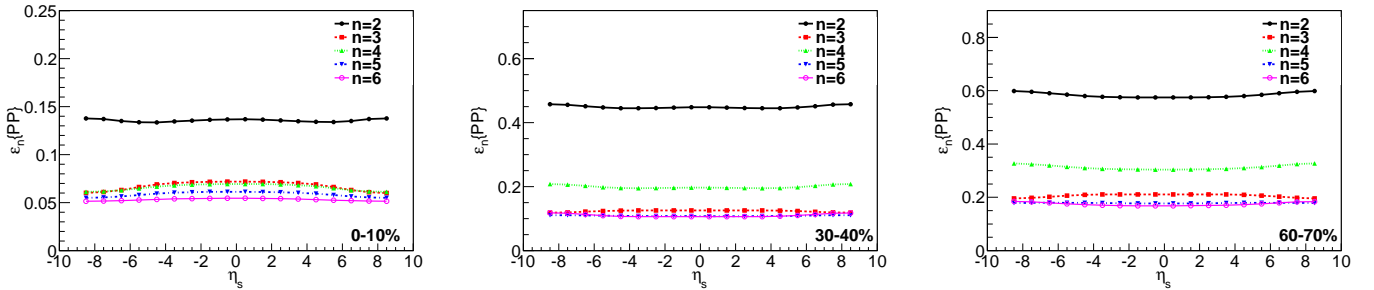


Figure 18: Space-time rapidity dependences of $\varepsilon_n\{\text{PP}\}$ in 0-10% (left), 30-40% (middle) and 60-70% (right) centrality at LHC energy using the MC-KLN initialisation.

can be also interpreted as follows. v_2 increases during the QGP evolution and does not so much in the hadronic evolution. So rapidity dependence of v_2 is a key to understand longitudinal structure of the QGP. Since $\varepsilon_n\{\text{PP}\}$ does not depend on space-time rapidity as shown in Fig. 18, $v_n(\eta)$ should contain the direct information about the longitudinal structure of the QGP. We will discuss (pseudo-)rapidity dependence of v_n later. The negative $\varepsilon_2\{\text{RP}\}$ in Figs. 19 and 21 is due to our definition of $\varepsilon_n\{\text{RP}\}$, Eq. (41), which has a different sign than the usual definition of eccentricity. Compared with finite $\varepsilon_n\{\text{PP}\}$, $\varepsilon_n\{\text{RP}\}$ vanishes for odd n since odd harmonics result solely from initial fluctuations and do not correlate with reaction plane. Although longitudinal profiles, Eqs. (46) and (47), in the MC-Glauber model gives similar rapidity and centrality dependence to the MC-KLN model, absolute values of $\varepsilon_n\{\text{PP}\}$ and $\varepsilon_n\{\text{RP}\}$ are different except for $n = 3$ as shown in Fig. 22.

2.7 Brief overview of event-by-event initial conditions

In this subsection, we review hydrodynamic modelling of relativistic heavy ion collisions by focusing particularly on initial conditions on an event-by-event basis.

One of the first works along these lines were the boost-invariant calculations by Gyulassy *et al.* [199] where HIJING [105, 106, 107, 108] event generator was used to evaluate the initial conditions. At collider energies, mini-jets were expected to become one of the dominant sources of fluctuations. In HIJING, particle production is modelled by string excitation and its decay into hadrons by using Lund

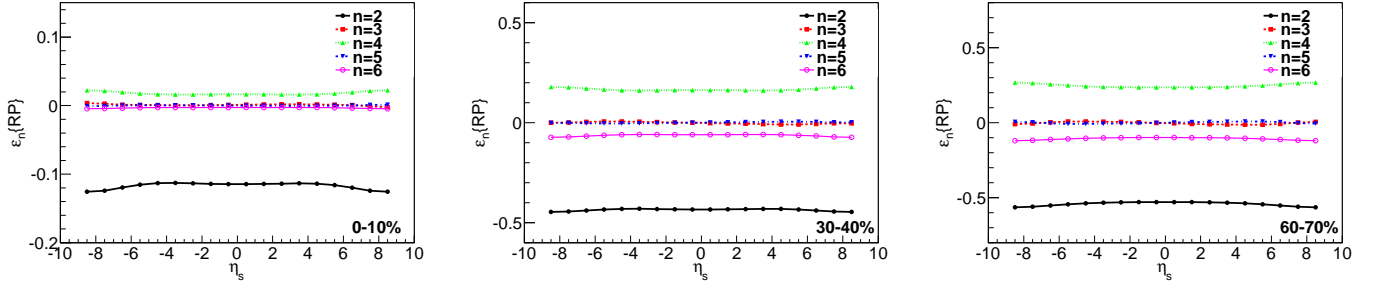


Figure 19: The same as Fig. 18 but for $\varepsilon_n\{\text{RP}\}$.

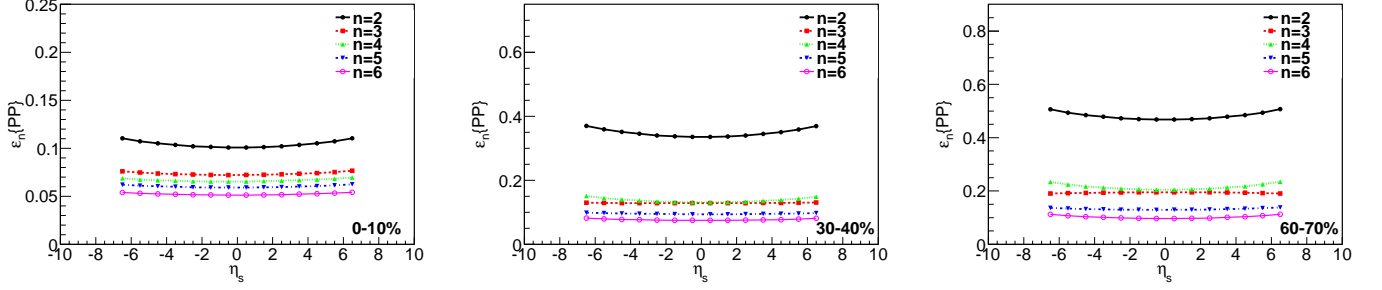


Figure 20: The same as Fig. 18 but using the MC-Glauber initialisation.

jet fragmentation scheme for soft processes, and hard pQCD processes are generated based on an eikonal multiple collision formalism and PYTHIA event generator [113].

Another pioneering work was done by the Rio and Sao Paulo groups, who used NeXus event generator [200] to calculate initial condition of fully (3+1) dimensional ideal hydrodynamic simulations [201, 202, 203, 204, 205, 206, 207]. They were the first to point out the importance of initial state fluctuations when interpreting the elliptic flow data. Namely, the calculated v_2 is different depending on whether one first evaluates an average initial state, evolves it hydrodynamically, and calculates the v_2 , or whether one evolves the initial states event-by-event, calculates v_2 in every event, and averages these calculated values [204, 205]. NeXus is a Monte-Carlo event generator based on the Gribov-Regge theory and the pQCD parton model. To convert the output of NeXus to the initial state of hydrodynamic evolution, they calculate the energy momentum tensor and conserved currents using the kinetic theory definitions. Obviously, energy momentum tensor obtained in this way is far from the one in equilibrium. Nevertheless, the energy momentum tensor can be decomposed and energy density and

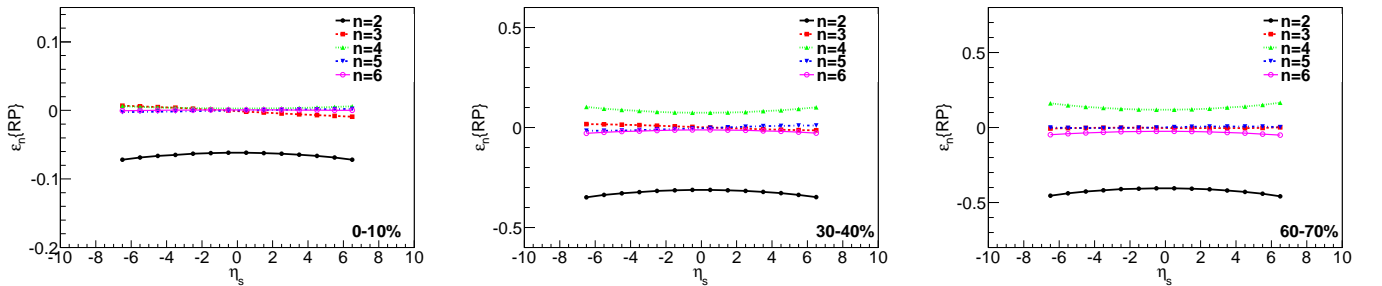


Figure 21: The same as Fig. 19 but using the MC-Glauber initialisation.

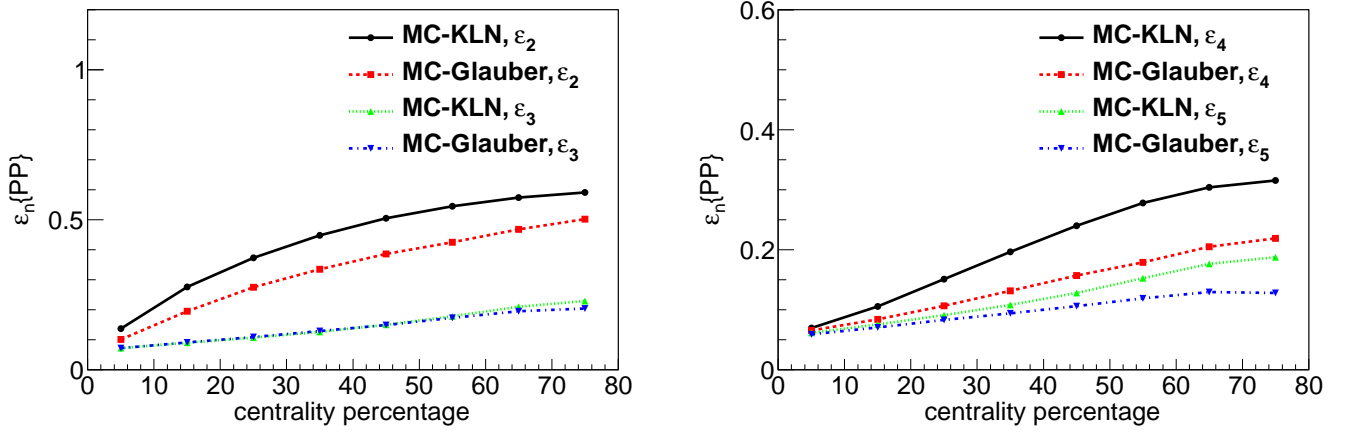


Figure 22: Centrality dependence of ε_2 and ε_3 (left) and ε_4 and ε_5 (left) for charged hadrons at midrapidity ($0 < \eta_s < 1$) in Pb+Pb collisions at $\sqrt{s_{NN}} = 2.76$ TeV. Results from the MC-KLN model are compared with the ones from the MC-Glauber model.

velocity obtained *a. la.* Landau

$$T^\mu{}_\nu u^\nu = \epsilon u^\mu. \quad (48)$$

Using u^μ , one can also obtain baryon density from baryon current $n_B = u_\mu N_B^\mu$. Once ϵ and n_B are obtained, pressure is calculated by using the equation of state $P = P(\epsilon, n_B)$. Energy momentum tensor for perfect fluids is then based on this energy density, pressure and flow velocity, and the non-ideal terms in the original energy-momentum tensor are ignored. A drawback of this procedure is that energy and momentum are not strictly conserved [208] because the non-ideal terms are ignored and the EoS of the fluid may be different from the EoS of NeXus. Figure 23 shows initial energy density in a single event (left) and that averaged over 30 events (right). The bumpy structure in a single event is smeared by taking event averages in the initial condition.

The NeXus event generator and hydrodynamic approach was further utilised to evaluate two-pion correlation functions on event-by-event basis by Ren *et al.* [209]. The main motivation to consider initial fluctuations was to understand RHIC HBT data $R_{\text{out}}/R_{\text{side}} \sim 1$ [210, 211].

Later, the Jyväskylä group performed boost-invariant event-by-event ideal hydrodynamic simulations [212] using Monte-Carlo Glauber initialisation [28], and applied their results to analyse thermal photon spectra [213] and jet quenching [214]. With an option of eWN (energy density using wounded nucleons), initial energy density is calculated as

$$\epsilon(x, y) = \frac{K}{2\pi\sigma^2} \sum_{i=1}^{N_{\text{part}}} \exp \left[-\frac{(x - x_i)^2 + (y - y_i)^2}{2\sigma^2} \right]. \quad (49)$$

Here (x_i, y_i) is the transverse position of a participant from Monte-Carlo Glauber simulations. σ is a smearing parameter of the collision point being either 0.4 fm or 0.8 fm in this model. A parameter K controls the absolute value of particle yields. In most hydrodynamical calculations the elliptic flow parameter v_2 has been evaluated with respect to either reaction plane or participant plane. The Jyväskylä group were the first to use the event plane method to evaluate the hydrodynamically calculated v_2 , and thus to follow the experimental procedure as closely as possible. See, *e.g.*, Fig. 24 (left). They also analyse distribution of difference of angle at the second order (elliptic flow) between event and reaction/participant planes as shown in Fig. 24 (right).

The Monte-Carlo Glauber and KLN models were employed to initialise ideal [215] and viscous [216] fluid evolution also by the Ohio State group. In their MC-Glauber initialization they assumed that

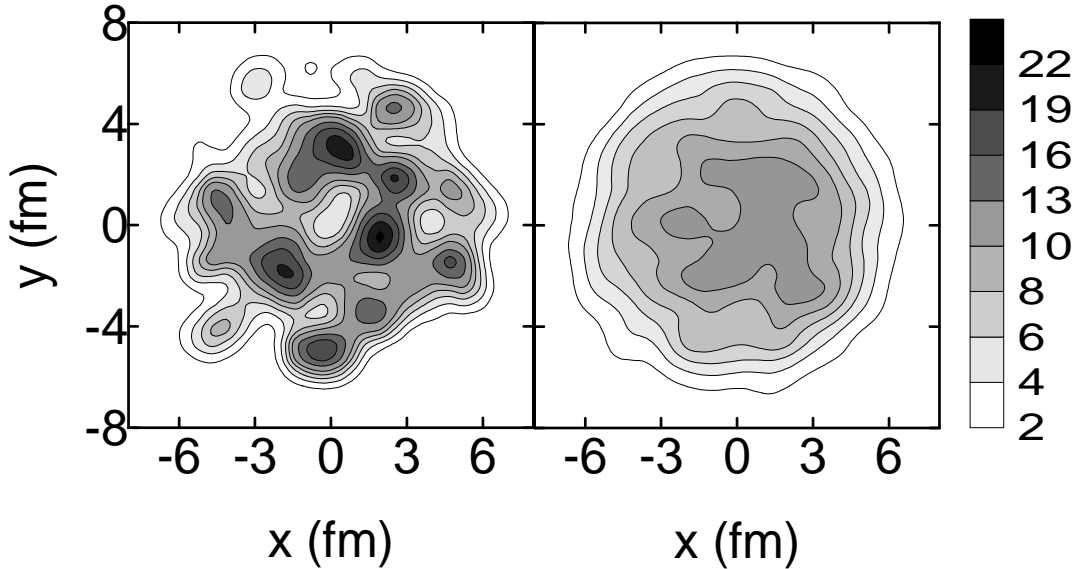


Figure 23: Examples of initial conditions in central Au+Au collisions given by NeXus at midrapidity. The energy density is plotted in units of GeV/fm^3 . (Left) Example of an event. (Right) Average over 30 events. Figure taken from Ref. [203].

initial entropy density profile, rather than energy density profile like in Eq. 49, is proportional to linear combination of soft wounded nucleon distribution and hard binary collision distribution. Correlations between the participant and the event plane angles [215], between the two participant plane angles and between the two event plane angles [216] were extensively studied by using event-by-event hydrodynamic simulations in (2+1) dimension assuming boost invariance in the longitudinal direction. Relations between different orders of harmonics were first discussed in Ref. [216] and will be discussed in detail in Sec. 4. Figure 25 shows centrality dependences of correlation between different order of event plane angles at the LHC energy using event-by-event viscous hydrodynamic simulations. Although there are small deviations from the ATLAS data [217], overall tendency is reproduced in this approach.

As mentioned in Sec. 2.5, the Frankfurt group has developed an integrated hybrid model based on fully (3+1) dimensional ideal hydrodynamics and UrQMD. In their model UrQMD is utilised both for generating the initial conditions and for describing the evolution in the hadronic phase [93, 130, 131, 132, 133, 134, 135]. Hydrodynamic simulations as well as UrQMD are performed in the three-dimensional Cartesian coordinate. At initial time t_{start} at which two colliding nuclei are maximally overlapped, $t_{\text{start}} = 2R/\gamma v$, where R (v) is a radius (velocity) of a colliding nucleus, initial energy density in the computational frame is calculated as

$$\epsilon(x, y, z) = \sum_p \frac{\gamma_z}{(2\pi)^{3/2} \sigma^2} E_p \exp \left[-\frac{(x - x_p)^2 + (y - y_p)^2 + \gamma_z^2 (z - z_p)^2}{2\sigma^2} \right], \quad (50)$$

where E_p is the total energy of a particle (also in the computational frame) from string fragmentations and γ_z Lorentz gamma factor in the beam direction. The width of the Gaussian is chosen to be $\sigma = 1$ fm as a default value, which is a little larger compared with other approaches. Consequently the resultant initial energy density distribution is smoother than in other Monte-Carlo approaches requiring smearing. See, *e.g.*, Fig. 26.

Werner *et al.* [137, 138, 139, 140] utilised the EPOS event generator [218] to generate the initial conditions for (3+1) dimensional ideal fluid evolution. EPOS is the successor of NeXus and is based on Pomerons and partons. Nuclear effects such as Cronin effect, parton saturation, and screening are introduced into EPOS. Energy momentum tensor is calculated from four-momenta of string segments

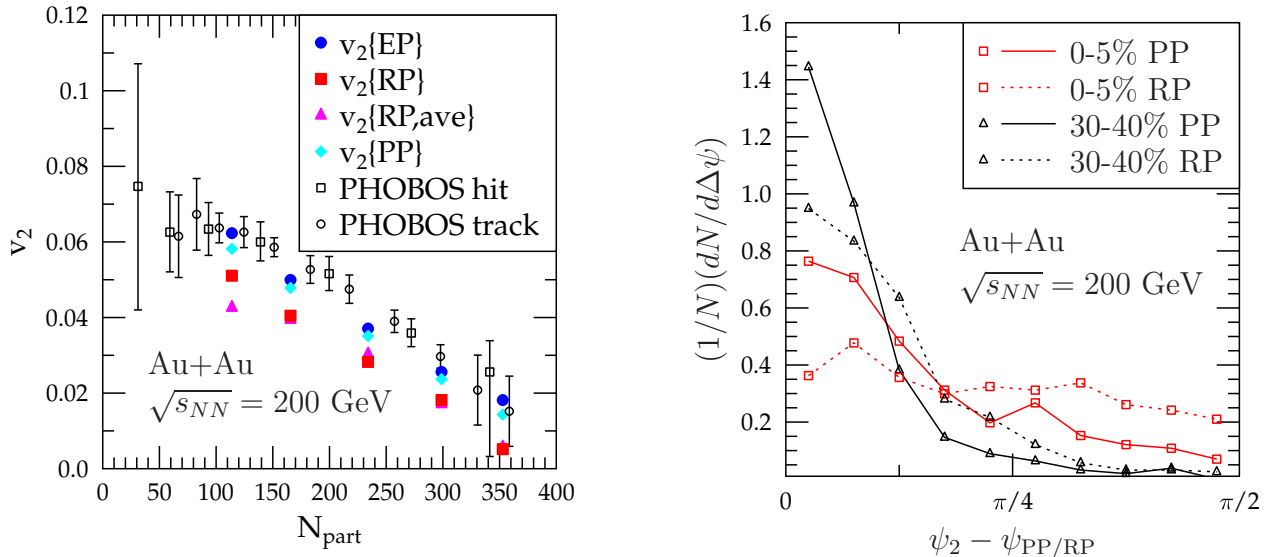


Figure 24: (Left) Elliptic flow parameter v_2 with $\sigma = 0.4$ fm in Au+Au collisions at $\sqrt{s_{NN}} = 200$ GeV are compared with the PHOBOS data. (Right) Distribution of difference of angles between event and reaction planes and event and participant planes in central (0-5%) and semicentral (30-40%) collisions. Figures are taken from Ref. [212].

δp^μ

$$T^{\mu\nu}(x) = \sum_i \frac{\delta p_i^\mu \delta p_i^\nu}{\delta p_i^0} g(x - x_i), \quad (51)$$

where the summation is taken over for each i -th segment and g is a Gaussian type smearing function with a width 0.25 fm. The energy momentum tensor is then converted to energy density and velocity using a similar procedure than what the Rio and Sao Paulo groups use. Since these string segments decayed from flux tubes correlate in the longitudinal direction, transverse profiles look quite similar at each space-time rapidity. Consequently, this leads to the so-called ridge structure in the di-hadron correlation function as shown in Fig. 27.

Parametrised initial conditions including higher order deformation were used in viscous hydrodynamic simulations to discuss triangular flow by Alver *et al.* [190]. This is not actually an event-by-event hydrodynamic simulation. Nevertheless, it captures some features of higher order deformation in the initial profiles. An idea behind this is quite similar to the model ‘‘B’’ explained in the previous subsection in our study. Initial energy density in the transverse plane is parametrised as

$$\epsilon(x, y) = \epsilon_0 \exp \left\{ -\frac{r^2 [1 + \epsilon_n \cos n(\phi - \psi_n)]}{2\rho^2} \right\}, \quad (52)$$

where $r = \sqrt{x^2 + y^2}$ is radial and ϕ is azimuthal angle in the polar coordinate. ϵ_n is the magnitude of the deformation and ψ_n is a reference angle. ρ is roughly root-mean-square radius of the produced matter and taken to be 3 fm. The deformation ϵ_n is estimated by either the MC-Glauber or the MC-KLN model. They tuned η/s to reproduce centrality dependence of v_2 at the RHIC energy. Resultant values are $\eta/s = 0.08$ and 0.16 for the MC-Glauber and the MC-KLN model, respectively. Using this parameter, they could reproduce v_3 as a function of N_{part} in the MC-Glauber model. Whereas, their v_3 using the MC-KLN model with $\eta/s = 0.16$ are significantly smaller than the v_3 data. Thus

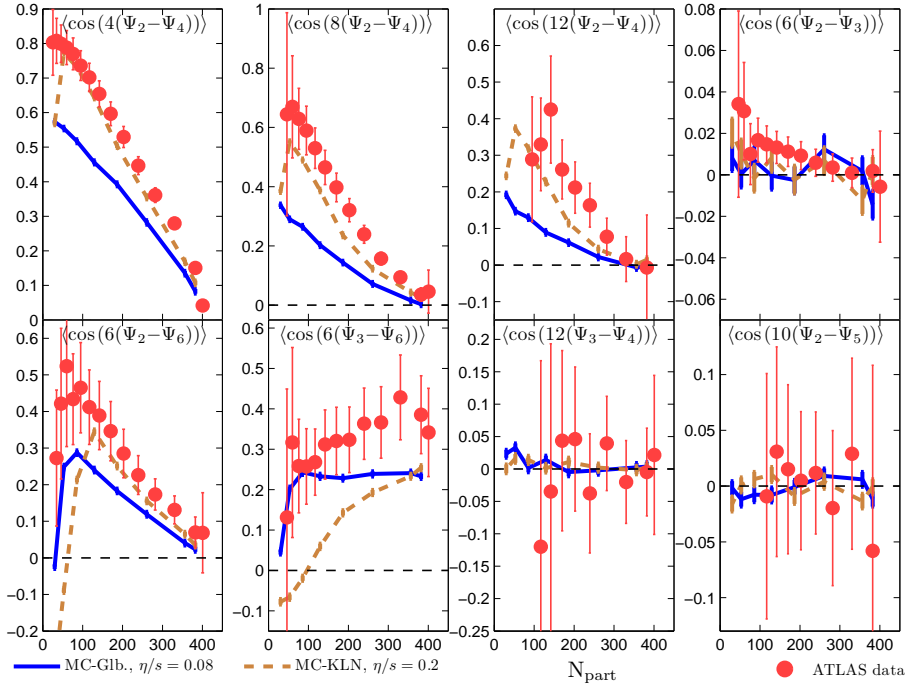


Figure 25: Centrality dependences of correlation between different order of event plane angles are compared with the ATLAS data [217]. The MC-Glauber (solid) and MC-KLN (dashed) initial profiles are propagated using viscous hydrodynamics with $\eta/s = 0.08$ and 0.2 , respectively. Figure is taken from Ref. [216].

they concluded v_3 data set a severe constraint to the initialisation model in viscous hydrodynamic simulations.

Fully (3+1) dimensional viscous hydrodynamic simulations on an event-by-event basis were performed by Schenke *et al.* [219, 220]. They have also recently evaluated fluctuating Glasma initial conditions by solving classical Yang-Mills equations, and used them as the initial state for hydrodynamical calculations [221, 222]. In their first papers they utilise the MC-Glauber model and initialise the energy density distribution in the transverse plane as in Eq. (49) [219]. In the longitudinal direction, they assume the energy density follows Bjorken scaling solution near midrapidity and falls like a half Gaussian near beam rapidity [219]. Recently, the IP-Glasma model [221, 222, 223] was employed to initialise energy density in hydrodynamic simulations. The IP-Glasma model solves the classical Yang-Mills equations in which initial charge distributions of two colliding nuclei are sampled from a Gaussian distribution with impact parameter and Bjorken x dependent color charge distributions. Parametrization of x and impact parameter dependence of saturation scale is taken from the IP-Sat (Impact Parameter Saturation) model [224, 225]. In this model event-by-event energy distribution exhibits the expected negative binomial distribution and it described the observed multiplicity distribution up to a constant scaling factor [223]. Quite remarkably it correctly predicts the event-by-event distribution of v_2 , v_3 and v_4 [222], which should be important in understanding initial fluctuations. Fluctuations in the IP-Glasma model have a length scale of the order of the inverse of the saturation scale $Q_s^{-1}(\mathbf{x}_\perp) \sim 0.1-0.2$ fm which is smaller than typical length scales $0.4 \lesssim \sigma \lesssim 1$ fm in other calculations. Figure 28 shows comparison of initial energy density distribution among the IP-Glasma, MC-KLN and MC-Glauber models. Finer structure is seen in the result from the IP-Glasma model.

A simple parametrisation for initial energy density was employed by Chaudhuri in his (2+1)-

2.83 fm Energy density distribution

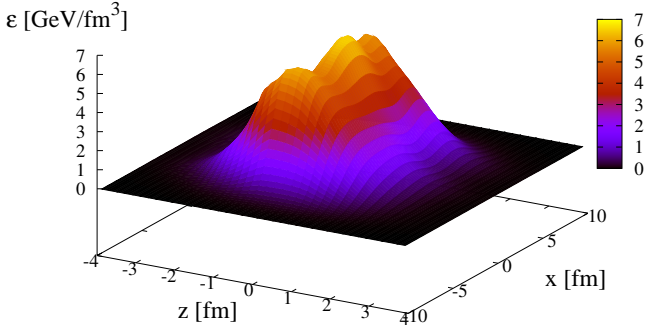


Figure 26: (Left) Initial energy density distribution in the reaction plane of single central event in Pb+Pb collisions at $E_{\text{lab}} = 40A$ GeV from UrQMD. Figure taken from Ref. [93].

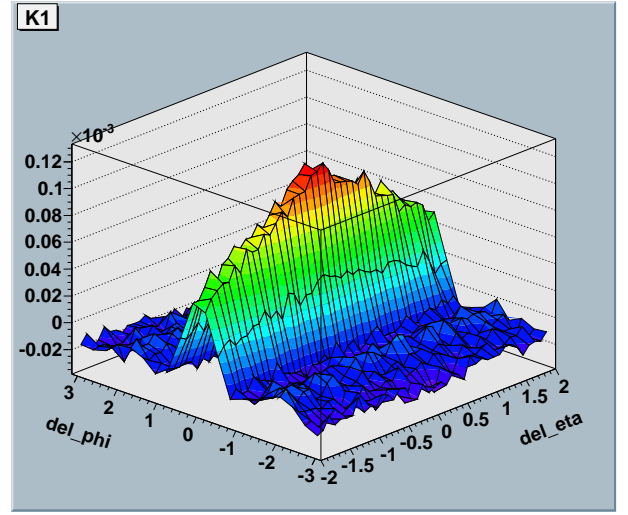


Figure 27: (Right) Dihadron correlation in $\Delta\eta$ - $\Delta\phi$ plane in central Au+Au collisions at $\sqrt{s_{NN}} = 200$ GeV from event-by-event EPOS+ideal hydrodynamic simulations. Figure taken from Ref. [137].

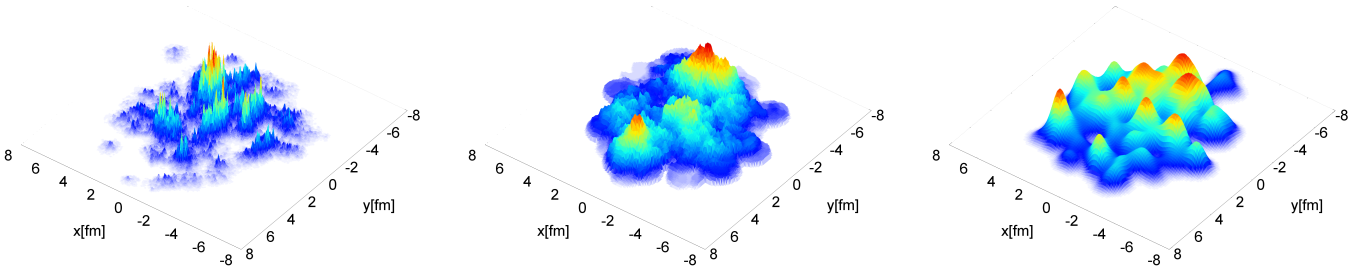


Figure 28: Examples of initial energy density distribution from the IP-Glasma model at $\tau = 0$ fm (left), the MC-KLN model (middle) and the MC-Glauber model (right). Figures are taken from Ref. [221]

dimensional viscous hydrodynamic simulations [226, 227]

$$\epsilon(x, y) = \epsilon_0 \sum_{i=1}^{N_{\text{part}}} \exp \left[-\frac{(\mathbf{r} - \mathbf{r}_i)^2}{2\sigma^2} \right]. \quad (53)$$

The width is set to $\sigma = 1$ fm and ϵ_0 is chosen to reproduce multiplicity in the experimental data. N_{part} is calculated using the optical Glauber model, and the positions of the hotspots, \mathbf{r}_i , are assumed to be Gaussian distributed. It is noted that, since the hot-spot would originate from a pair of participating nucleons, a scheme to randomly sample independent position of hot-spots using averaged distribution of N_{part} in the transverse plane does not capture the actual distribution of correlated hot-spots from the MC-Glauber model. Later, the effect of choice of smearing profile on final v_2 and v_3 in the context of the MC-Glauber model was examined by choosing the Wood-Saxon profile instead of the Gaussian one [228]. They found that the anisotropy coefficients v_2 and v_3 were not affected by the form of the smearing profile nor by the value of the smearing parameter, whereas coefficients v_4 and v_5 showed some sensitivity to the smearing.

Bozek *et al.* employed Monte-Carlo Glauber model GLISSANDO [29] for initialisation in their event-by-event full (3+1)-dimensional viscous hydrodynamic simulations [229]. Initialization of the entropy profile in the transverse plane is quite similar to others:

$$s(x, y) = \kappa \sum_i g_i(x, y)[(1 - \alpha) + N_i^{\text{coll}}\alpha], \quad (54)$$

$$g_i(x, y) = \frac{1}{2\pi w^2} \exp \left[-\frac{(x - x_i)^2 + (y - y_i)^2}{2w^2} \right]. \quad (55)$$

Here the summation is taken over participants and N_i^{coll} is the number of collisions of the i -th participant. Similar to other groups, the transverse position of nucleons is smeared from a point-like source to a Gaussian profile with a width $w = 0.4$ fm. Soft-hard mixture $\alpha = 0.125$ leads to reproduction of centrality dependence of $dN_{\text{ch}}/d\eta$ at the top RHIC energy within the full (3+1)-dimensional viscous hydrodynamic simulations. Note that, since the Glauber approach tells us only profiles in the transverse plane, longitudinal profiles of the produced matter have to be also modeled by taking account of momentum conservation among colliding nucleons at certain transverse position [229].

$$f_{\pm}(\eta_s) = \left(1 \pm \frac{\eta_s}{y_{\text{beam}}} \right) f(\eta_s), \quad (56)$$

$$f(\eta_s) = \exp \left[-\frac{(\eta_s - \eta_0)^2}{2\sigma_{\eta}^2} \theta(|\eta_s| - \eta_0) \right], \quad (57)$$

where y_{beam} is the beam rapidity. Using this model, they calculated transverse momentum fluctuations at the RHIC energy and found the experimental data can be explained by the event-by-event fluctuations of initial profiles.

Recently, Pang *et al.* employed the AMPT event generator for initialisation in event-by-event (3+1)-dimensional ideal hydrodynamic simulations [230]. Information about phase space density from the AMPT simulation at some initial time τ_0 is used to calculate local energy-momentum tensor

$$T^{\mu\nu}(\tau_0, x, y, \eta_s) = K \sum_i \frac{p_i^{\mu} p_i^{\nu}}{p_i^{\tau}} \frac{1}{2\pi\sigma_r^2} \exp \left[-\frac{(x - x_i)^2 + (y - y_i)^2}{2\sigma_r^2} \right] \frac{1}{\tau_0 \sqrt{2\pi\sigma_{\eta_s}^2}} \exp \left[-\frac{(\eta_s - \eta_{s,i})^2}{2\sigma_{\eta_s}^2} \right], \quad (58)$$

where $p^{\tau} = m_T \cosh(Y - \eta_s)$ for the i -th parton. The widths in transverse and longitudinal directions are chosen as being $\sigma_r = 0.6$ fm and $\sigma_{\eta_s} = 0.6$, respectively. They allowed one parameter K to reproduce experimentally-measured multiplicity at midrapidity. In actual calculations at the LHC energy, $K = 1.6$ and $\tau_0 = 0.2$ fm. Through this approach, one can include fluctuations of the density profile in the longitudinal direction as well as in the transverse plane and of flow velocities in the initial conditions. They found that initial fluctuations in rapidity distributions lead to expanding hot spots in the longitudinal direction and that fluctuations in the initial flow velocities lead to harder transverse momentum spectra of final hadrons due to non-vanishing initial radial flow velocities.

Zhang *et al.* investigated the effect of initial fluctuation on jet energy loss using (2+1) dimensional ideal hydrodynamic model [231]. They found that, compared with smooth initial conditions, a jet loses slightly more energy in the expanding QGP with fluctuating initial conditions.

Table 3 summarises current status of event-by-event hydrodynamic simulations by focusing on initialisation models and dimension of hydrodynamic simulations. Note that there are many more models for initializing the event-by-event calculations than there are hadronic cascade models used in the hydro + cascade models (Table 1).

3 Results from smooth initial profile

In this section, we show results from the integrated dynamical model starting from conventional smooth initial entropy density distributions to describe a high-energy heavy ion reaction as a whole at LHC

Table 3: Event-by-event hydrodynamic simulations.

Authors and References	Initialisation Model	Dimension	Ideal/Viscous
Gyulassy <i>et al.</i> [199]	HIJING	(2+1)-D	Ideal
Aguiar <i>et al.</i> [202, 203, 204, 205, 206, 207]	NeXus	(3+1)-D	Ideal
Ren <i>et al.</i> [209]	NeXus	(3+1)-D	Ideal
Holopainen <i>et al.</i> [212, 213, 214]	MC-Glauber	(2+1)-D	Ideal
Qiu and Heinz [215]	MC-Glauber, MC-KLN	(2+1)-D	Ideal
Petersen <i>et al.</i> [93, 130, 131, 132, 133, 134, 135]	UrQMD	(3+1)-D	Ideal
Werner <i>et al.</i> [137, 138, 139, 140]	EPOS	(3+1)-D	Ideal
Alver <i>et al.</i> [190]	Parametrisation	(2+1)-D	Viscous
Schenke <i>et al.</i> [219, 220, 221]	MC-Glauber, IP-Glasma	(3+1)-D	Viscous
Chaudhuri <i>et al.</i> [226, 228]	Parametrisation	(2+1)-D	Viscous
Bozek and Broniowski [229]	MC-Glauber	(3+1)-D	Viscous
Pang <i>et al.</i> [230]	AMPT	(3+1)-D	Ideal
Zhang <i>et al.</i> [231]	MC-Glauber	(2+1)-D	Ideal
This study	MC-Glauber, MC-KLN	(3+1)-D	Ideal

and RHIC. We show p_T spectra for pions, kaons and protons, v_2 for charged hadrons as functions of centrality and p_T and $v_2(p_T)$ for identified hadrons. For the models of initialisations, MC-KLN and MC-Glauber models are employed and the results obtained using them are compared with each other. We will compare some of these results with those from event-by-event hydrodynamic simulations later.

3.1 Results at RHIC

In Figs. 29 and 30 we show transverse momentum distributions of positive pions and kaons, and the average of protons and antiprotons around midrapidity ($|\eta| < 0.35$) in $\sqrt{s_{NN}} = 200$ GeV Au+Au collisions. The results calculated using the KLN model and Glauber model initial conditions (Figs. 29 and 30, respectively) are compared with the PHENIX data [67]. Although initial conditions are taken from “Model B” in both cases, results from “Model A” (simple average over many samples) are almost identical to these. In central collisions, we reproduce the PHENIX data [67] well up to $p_T \sim 3$ GeV/ c . The p_T region where the model works well becomes smaller as going to peripheral collisions: For example, in 70-80% centrality, we reproduce p_T spectrum for pions up to $p_T \sim 1$ GeV/ c and, beyond this, other components such as recombination and/or jet fragmentation, which are missing in the current integrated model, may be dominant. p_T slopes from the KLN model are a little harder than those from the Glauber model. It should be noted here that we chose the switching temperature $T_{sw} = 155$ MeV to obtain the observed particle ratios of these identified hadrons, not to reproduce p_T slope. Final particle spectra are expected to be independent of a choice of the switching temperature. However, this is not the case in the current calculations: The particle yields depend on the switching temperature and thus it can be fixed using the particle ratios. Similar sensitivity to the value of T_{sw} was seen also in Ref. [85], where a systematic analysis of switching temperature dependence was made.

In Fig. 31 (left), v_2 in Au+Au collisions is compared with v_2 in U+U collisions at $\sqrt{s_{NN}} = 200$ GeV. Here initial conditions are taken from “Model B” and the momentum distribution is integrated over $|\eta| < 1$ and the whole p_T region. Since larger eccentricity leads to larger momentum anisotropy and v_2 , the systematics of $v_2(N_{part})$ is similar to that of $\varepsilon_{part}(N_{part})$ as shown in Fig. 14 (left). v_2 is larger in U+U collisions than in Au+Au collisions, and KLN initialisation leads to larger v_2 than Glauber initialisation. v_2 first increases with decreasing N_{part} , which reflects increasing initial eccentricity. When N_{part} falls below ~ 50 , v_2 , however, begins to decrease. This is due to the short lifetime of the system

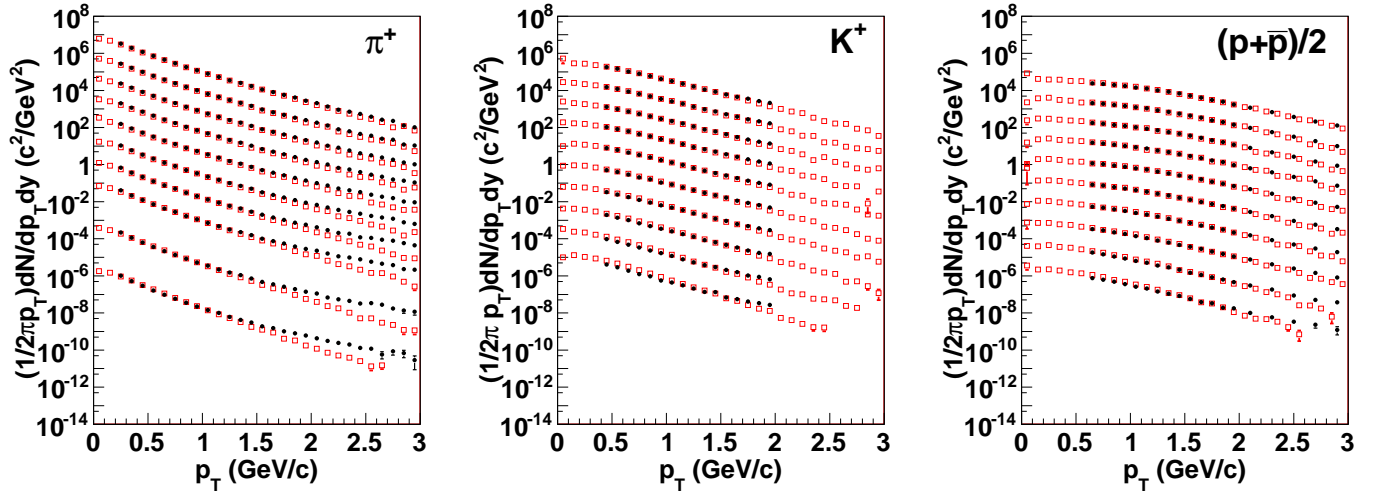


Figure 29: Transverse momentum distributions of π^+ (left), K^+ (middle) and $(p+\bar{p})/2$ (right) in $\sqrt{s_{NN}} = 200$ GeV Au+Au collisions at 0-5, 5-10, 10-15, 15-20, 20-30, 30-40, 40-50, 50-60, 60-70 and 70-80% centralities from top to bottom. Both the PHENIX data [67] (filled circle) and results calculated using the KLN initial conditions (open square) are shown. To show all these results, each spectrum is multiplied by 10^n with $n = 4, 3, 2, \dots, -5$ from top to bottom for kaons and protons. For pions, $n = 4, 3, 2, \dots, -3, -5$ and -7 .

which does not allow the flow to fully build up, and to the large fraction of the lifetime spent in the hadronic phase where dissipative effects are large.

In Au+Au collisions, results from the Glauber initialisation almost reproduce the PHOBOS data [9]. This indicates that there is little room for QGP viscosity in the model calculations. On the other hand, apparent discrepancy between the results from the KLN initialisation and the PHOBOS data means that viscous corrections during the fluid evolution are required. Figure 31 (right) shows a comparison of results with the PHOBOS data in Cu+Cu collisions [32]. Again, the Glauber model initialisation almost reproduces PHOBOS data, while the KLN initialisation leads to larger v_2 than the PHOBOS data.

As expected, the system in U+U collisions at $\sqrt{s_{NN}} = 200$ GeV is denser than in Au+Au collisions at the same energy. At initial time $\tau_0 = 0.6$ fm/c, the maximum temperature (energy density) in the most central 5% of U+U collisions is $T_0 = 367$ MeV ($e_0 = 33.4$ GeV/fm³) and $T_0 = 361$ MeV ($e_0 = 31.4$ GeV/fm³) in the Au+Au collisions of the same centrality. This corresponds to charged particle transverse densities of 25.4 and 24.1, respectively, which means that the transverse density in U+U collisions is indeed larger, but only by $\sim 6\%$.¹¹

Figure 32 shows again the centrality dependences of v_2 in Au+Au (left) and Cu+Cu (right) collisions at $\sqrt{s_{NN}} = 200$ GeV. Here initial conditions are taken from Model “B” and the momentum distribution is integrated over $|\eta| < 1$ and $0.15 < p_T < 2$ GeV/c according to experimental setup in STAR [79, 232]. Experimental data in Au+Au collisions [79] have been corrected to subtract non-flow effects [233] and, thus, all data sets from various flow analysis methods coincide with each other. Notice that the data have not been corrected yet in Cu+Cu collisions [232]. Similar to the results in Fig. 31, the Glauber initialisation little overshoots the STAR data, while the KLN initialisation leads to larger v_2 than the Glauber initialisation clearly overshooting the STAR data.

¹¹With sufficient statistics, one may make more severe centrality cut (e.g., 0-3%) to obtain larger transverse particle density. Multiplicity fluctuation in the centrality cut, which we do not take into account, could also enhance the transverse particle density.

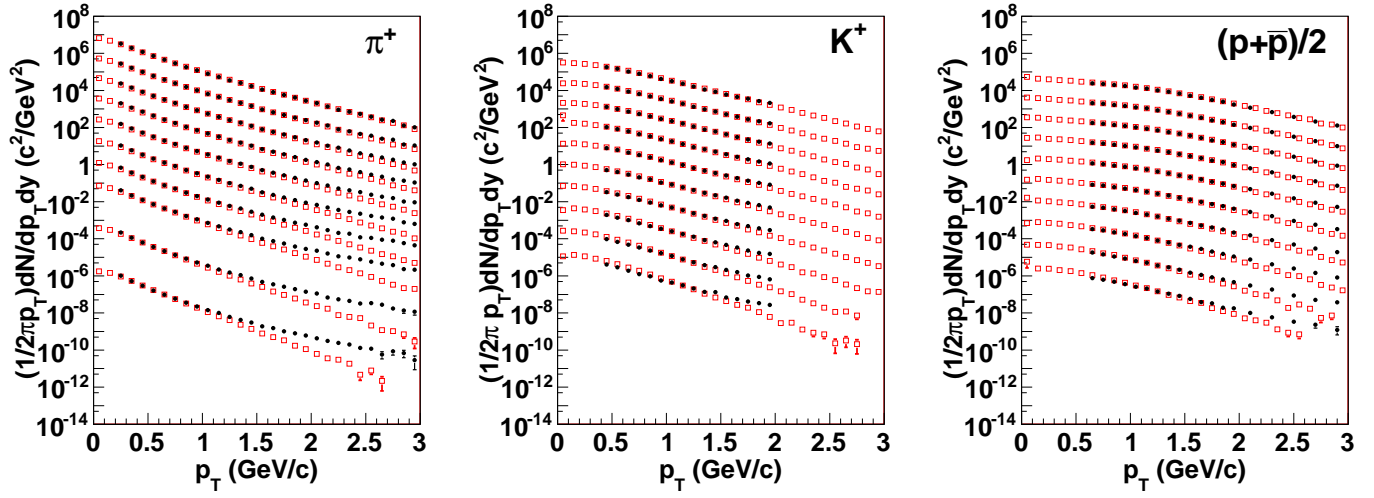


Figure 30: The same as Fig. 29 but using the Glauber model initial conditions.

In Figure 33 the calculated $v_2(p_T)$ for charged hadrons in $\sqrt{s_{NN}} = 200$ GeV Au+Au collisions is compared with the PHENIX [234] and STAR [79] data in 0-10% (top left), 10-20% (top middle), 20-30% (top right), 30-40% (bottom left), 40-50% (bottom middle) and 50-60% (bottom right) centralities. The calculation was done using the Glauber model initial state in the model “B” setting. In 0-10% central collisions, results from the model is almost identical to the PHENIX $v_2\{\text{BBC}\}$ data. However, the data deviate from theoretical results as going to peripheral collisions, which suggests the importance of viscous effects in peripheral collisions where the transverse flow is more anisotropic and the size of the system is smaller than in central collisions.

As shown in Fig. 34, $v_2(p_T)$ pattern in Au+Au collisions is quite similar to that in Cu+Cu collisions even though the size of the system in the latter case is smaller than in the former case. Experimental data are taken from PHENIX [235] and STAR [232].

As already seen in the integrated v_2 in Figs. 31 and 32, the KLN model gives a larger v_2 than the Glauber model does. This is again seen in $v_2(p_T)$ in Figs. 33 and 35: The slope of $v_2(p_T)$ from the KLN initialisation is slightly steeper than that from the Glauber initialisation.

In Fig. 36, $v_2(p_T)$ for identified hadrons using the Glauber initialisation are compared with the PHENIX data. Mass splitting pattern, which is known to come mainly from hadronic rescattering effects [126], is seen in both theoretical results and experimental data. In low p_T region up to ~ 1 GeV/c, we reasonably reproduce the PHENIX data. However, the data gradually deviate from the theoretical results above $p_T \sim 1$ GeV/c, which suggests again the necessity of viscous corrections. As already seen in the $v_2(p_T)$ for charged hadrons, v_2 for pions overshoots the data in semi-central collisions.

It might be also interesting to analyse v_2 for ϕ mesons in low p_T region: Since ϕ mesons hardly rescatter with pions in the late hadronic stages, these particles do not participate in mass splitting pattern [126]. A hint of this behaviour has been already seen in recent STAR data [236].

3.2 Results at LHC

Figure 37 shows a comparison of transverse momentum distributions of charged hadrons between RHIC and LHC energies at 10-20% and 40-50% centralities. As clearly seen from figures, the slope of the p_T spectra becomes flatter as collision energy and, consequently, pressure of produced matter increases. To quantify this, we calculate mean p_T of charged hadrons. In the MC-Glauber initialisation, mean p_T increases from RHIC to LHC by 21% and 19% in 10-20% and 40-50% centrality, respectively. On

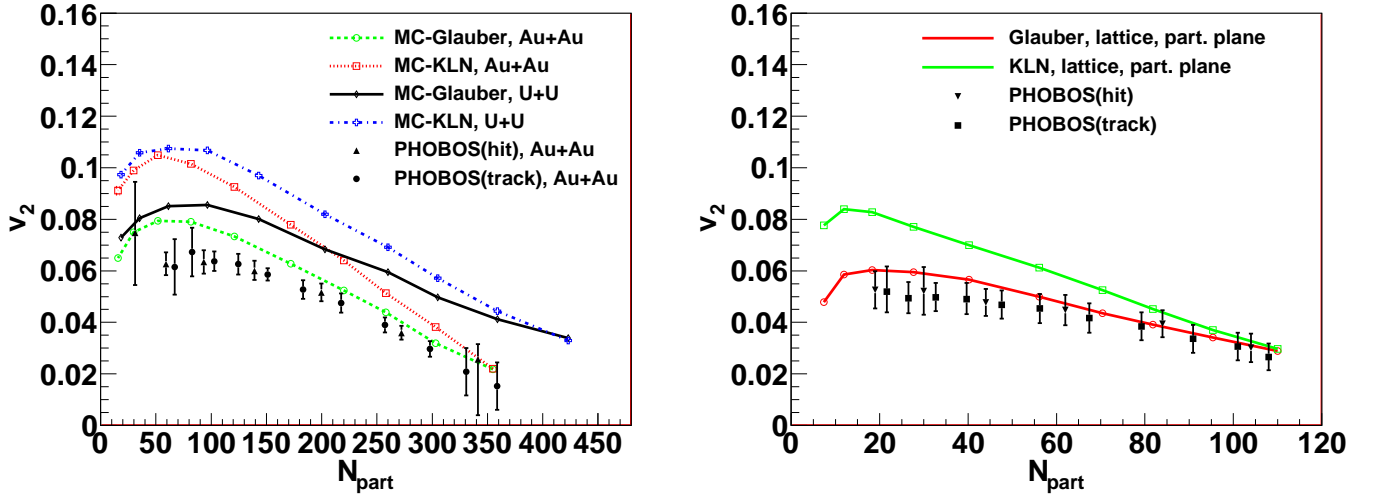


Figure 31: N_{part} dependence of v_2 evaluated using model “B” (see the text) in Au+Au (left) and Cu+Cu (right) collisions at $\sqrt{s_{NN}} = 200$ GeV are compared with the PHOBOS data [9, 32]. Predictions in U+U collisions at $\sqrt{s_{NN}} = 200$ GeV are also shown in the left figure (taken from Ref. [53]).

the other hand, the corresponding relative increases are 25% and 24% in the MC-KLN initialisation. Since our calculations at RHIC were tuned to reproduce the p_T -spectra, this means that at LHC the spectra calculated using the MC-KLN initialisation are slightly flatter than those calculated using the MC-Glauber initialisation.

We compare the integrated v_2 for charged hadrons with respect to reaction plane with the ALICE [11] and STAR [79] $v_2\{4\}$ data in Fig. 38. When evaluating the integrated v_2 , we take account of both transverse momentum and pseudorapidity acceptance as done in the experiments, *i.e.* $0.2 < p_T < 5.0$ GeV/ c and $|\eta| < 0.8$ for ALICE, and $0.15 < p_T < 2.0$ GeV/ c and $|\eta| < 1.0$ for STAR. We want to emphasise that, not only the p_T cut [237], but also the pseudorapidity cut plays an important role in a consistent comparison with the data. Due to the Jacobian for the change of variables from rapidity y to pseudorapidity η , $v_2(y = 0) < v_2(\eta = 0)$ for positive elliptic flow [127].¹² In the case of the MC-Glauber (MC-KLN) initialisation in 40-50% centrality, v_2 integrated over the whole p_T region is $\sim 14\%$ ($\sim 10\%$) larger at $\eta = 0$ than at $y = 0$.

When the MC-Glauber model is employed for initial profiles, centrality dependence of integrated v_2 from the hybrid approach almost agrees with both ALICE and STAR data. Since eccentricity fluctuation contributes little and negatively to $v_2\{4\}$ in a non-Gaussian distribution of eccentricity fluctuation [233, 238], this indicates there is only little room for the QGP viscosity in the model calculation. On the other hand, apparent discrepancy between the results from the MC-KLN initialisation and the ALICE and STAR data means that viscous corrections during the hydrodynamic evolution are required.

From RHIC to LHC, the p_T -integrated $v_2(|\eta| < 0.8)$ increases by 24% and 25% in 10-20% and 40-50% centrality, respectively, in the MC-Glauber initialisation. On the other hand, in the MC-KLN initialisation, the increase reaches 42% and 44% in 10-20% and 40-50% centrality, respectively. Since eccentricity does not change significantly (at most $\pm 6\%$ in 40-50% centrality) from RHIC to LHC as shown in Fig. 14 (right), the significant increase of integrated v_2 must be attributed to a change in transverse dynamics.

Finally, we compare $v_2(p_T)$ of charged hadrons with ALICE [11] and STAR [79] data in 10-20% (Fig. 39 (left)) and 40-50% (Fig. 39 (right)) centrality. Interestingly, the data at LHC agrees with

¹²Notice that even if one assumes the Bjorken scaling solution, one has to consider the pseudorapidity acceptance since $v_2(\eta)$ is not constant even if $v_2(y)$ is [127].

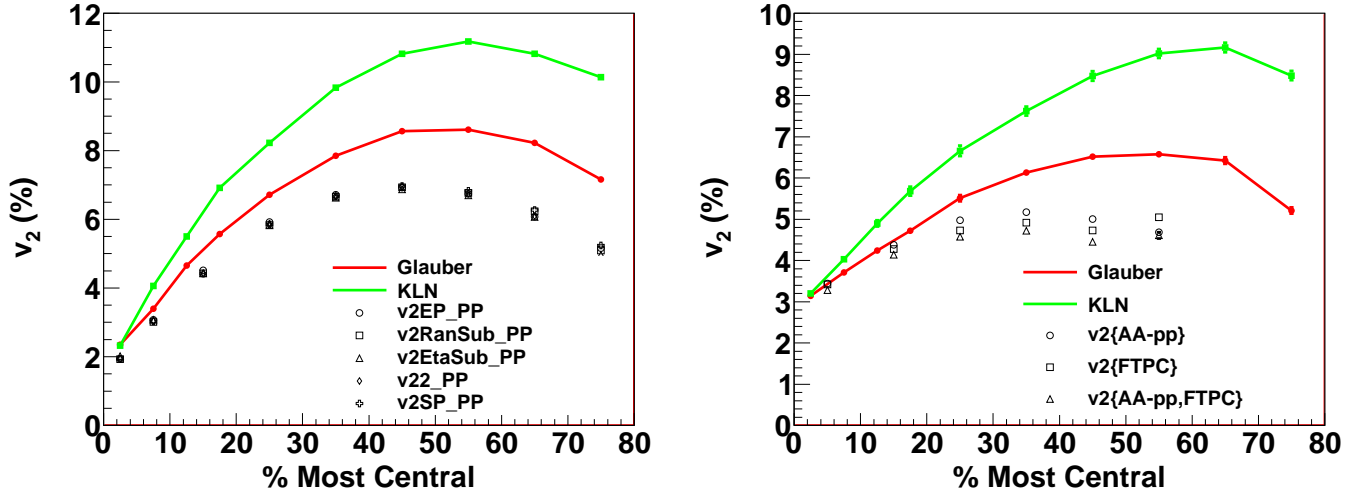


Figure 32: Centrality dependence of v_2 with respect to participant plane (model “B”) in Au+Au (left) and Cu+Cu (right) collisions at $\sqrt{s_{NN}} = 200$ GeV are compared with the STAR data [79, 232] ($0.15 < p_T < 2$ GeV/c and $|\eta| < 1$). Experimental data in Au+Au collisions are as corrected in Ref. [233].

the data at RHIC within errors. The calculated $v_2(p_T)$ shows similar independence of collision energy when MC-Glauber initialisation is used, whereas MC-KLN initialisation leads to a slightly larger $v_2(p_T)$ at the larger energy. For MC-Glauber results, the fit to the data is fair below $p_T \sim 1.5$ GeV/c and $p_T \sim 0.8$ GeV/c momenta in the 10-20% and 40-50% centralities, respectively. Results from the MC-KLN initialisation at both energies are significantly larger than experimental data in the whole p_T region, which again indicates the necessity of viscous corrections in hydrodynamic evolution. For both initialisations the difference between the data and the calculated $v_2(p_T)$ is larger in more peripheral collisions. This too can be understood as an indication of viscosity, since the more peripheral the collision, the smaller the system and the more anisotropic its shape, and both of these qualities enhance the dissipative effects.

Due to the relationships among the p_T spectrum, p_T averaged v_2 , and p_T differential $v_2(p_T)$, the flatter the p_T spectrum, the larger the v_2 even if $v_2(p_T)$ stays the same. It is also worth noticing that the steeper the slope of $v_2(p_T)$, the larger the increase in v_2 for the same increase in mean p_T . This is the main reason why quite a similar increase of mean p_T for both MC-Glauber and MC-KLN initialisations leads to much larger increase of v_2 for MC-KLN than for MC-Glauber initialisation.

Song *et al.* calculated v_2 as a function of centrality and p_T using viscous hydrodynamics by employing almost the same initial conditions as we did [141, 142, 85, 143] (see also Sec. 2.7). So it is interesting to see how much viscosity is required to reproduce these data in their analyses. As shown in Fig. 12, $\eta/s \sim 0.08$, which is almost identical to the conjectured minimum value [144], leads to reproduction of the v_2/ε data at RHIC in the MC-Glauber initialisation, whereas $\eta/s \sim 0.16$ in the MC-KLN initialisation [141]. Within the MC-KLN initialisation, they also calculated v_2 at the LHC energy and found that $\eta/s \sim 0.20$ - 0.24 is required to describe the data. This increase tendency of the specific shear viscosity with temperature is qualitatively consistent with expectation from results based on finite temperature QCD [239]. Temperature dependent shear viscosity was also discussed in [141, 240, 241]. It turned out that extracting the temperature dependence of η/s from the data is demanding, since at RHIC the value of η/s in the plasma phase does not affect the observed anisotropies. Only the minimum value reached in the transition region and viscosity in the hadronic phase do. At LHC the situation is better, but even there the hadronic viscosity affects the results as much as the plasma

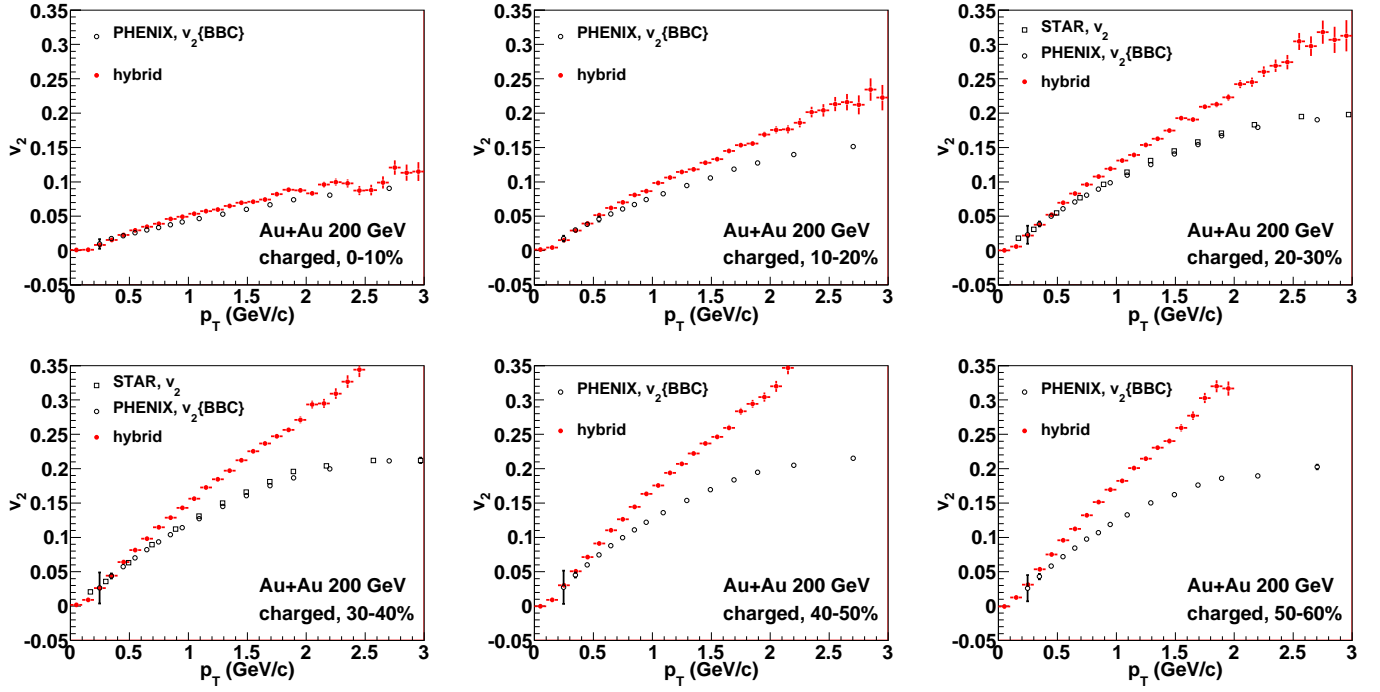


Figure 33: Transverse momentum dependence of v_2 of charged hadrons in $\sqrt{s_{NN}} = 200$ GeV Au+Au collisions in 0-10% (top left), 10-20% (top middle), 20-30% (top right), 30-40% (bottom left), 40-50% (bottom middle) and 50-60% (bottom right) centralities. Results calculated with respect to the participant plane (model “B”) using the Glauber model initial conditions are compared with the PHENIX [234] and STAR data.

viscosity does [240, 241].

4 Results from event-by-event hybrid simulations

We perform hydrodynamic simulations on an event-by-event basis and calculate observables using $\sim 10^5$ “minimum bias” events (events with $N_{\text{part}} \geq 2$ in our theoretical definition) for each initial parameter set. In this section, we especially focus on higher order harmonics using several flow analysis methods. We first overview the flow analysis methods employed in this study. Using these methods, we analyse final particle distributions to obtain azimuthal anisotropy coefficients. Most of the results are obtained using the MC-KLN initialisation at the LHC energy. We also compare these results with the ones obtained using the MC-Glauber initialisation.

4.1 Event plane method

In the event plane method [63], the event plane is first determined using the anisotropy of the emitted particles. The event plane is in general defined by

$$n\Psi_n^{\text{EP}} = \arg \sum_{j \neq i} \omega_j e^{in\phi_j}, \quad (59)$$

where ω_i is an weight and ϕ_i is an azimuthal angle for each particle. The sum is taken over an ensemble of particles which do not coincide with particles which v_n one wants to obtain.

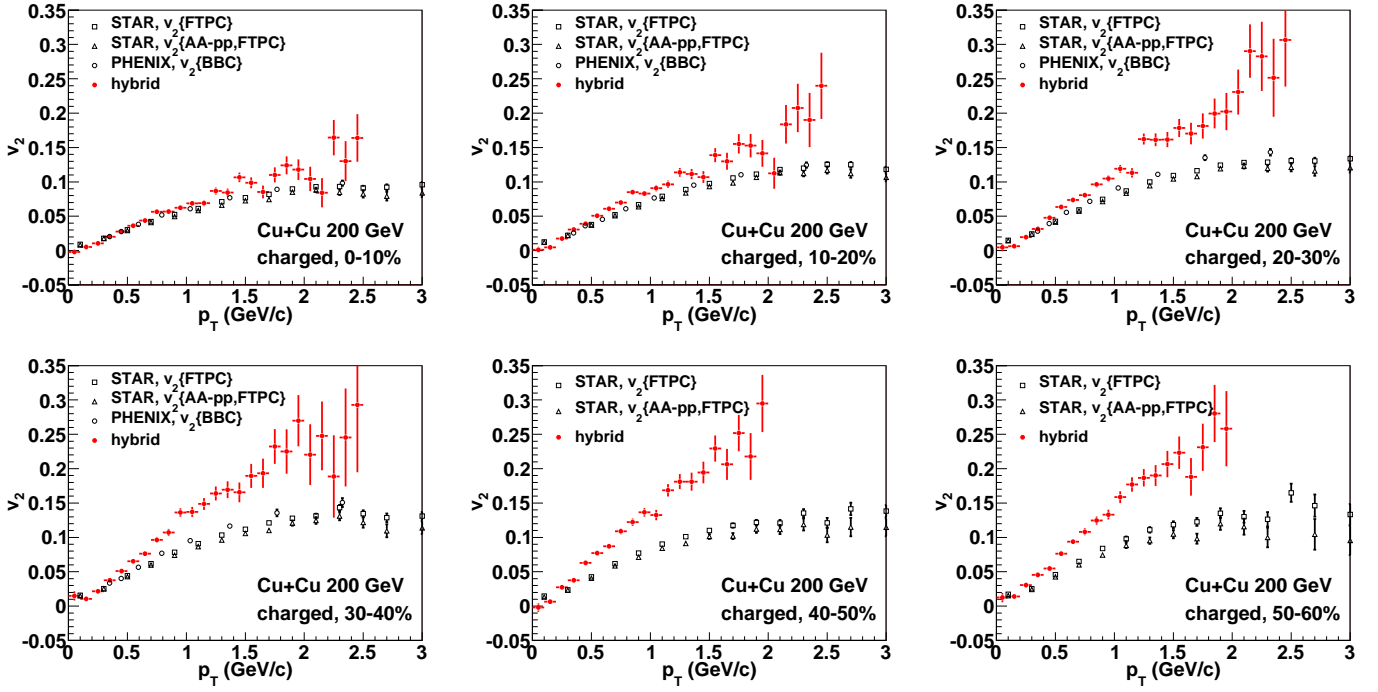


Figure 34: The same as Fig. 33 but in Cu+Cu collisions. Data are from PHENIX [235] and STAR [232].

In fact, there have been various event plane methods for the different detector setups. For example, one can randomly divide measured particles in a pseudorapidity region into two subgroups. Then when one wants to obtain flow parameters for particles in one subgroup, particles in the other subgroup are used to determine the event plane. One can also choose two groups of particles separated in pseudorapidity to determine the event plane, which can eliminate short range correlations.

In what follows, we demonstrate the flow analysis according to the event plane method by the ATLAS Collaboration [12].¹³ In this analysis method, the event planes are determined using particles in the two regions, A: $3.2 < \eta < 4.8$ and B: $-4.8 < \eta < -3.2$. ω_i is taken as transverse mass m_T^i for each particle. When the harmonics v_n is calculated in positive (negative) rapidity region, particles in the region B (the region A) are used to determine the event plane Ψ_n^B (Ψ_n^A) to avoid the non-flow effect from the autocorrelation. Centrality is defined using the total transverse energy of charged particles deposited in these rapidity regions, as prescribed by the ATLAS Collaboration [12].

In the “ η -subevent” method, non-flow effects can be eliminated at midrapidity when event plane angle is determined away from midrapidity. On the other hand, one naively anticipates the correlation between the event plane angle determined in the large rapidity region and the one in the whole rapidity region gets weaker [134]. As will be shown, this can be corrected by taking account of event plane resolution in the “ η -subevent” method.

Event plane angles for the n -th harmonics is thus calculated using the particles in the regions A and B as

$$n\Psi_n^A = \arg \sum_A m_T^i e^{in\phi_i}, \quad (60)$$

$$n\Psi_n^B = \arg \sum_B m_T^i e^{in\phi_i}, \quad (61)$$

¹³ The method employed here is categorised in the event plane method in a broad sense. However, this is sometimes called the “ η -subevent” method.

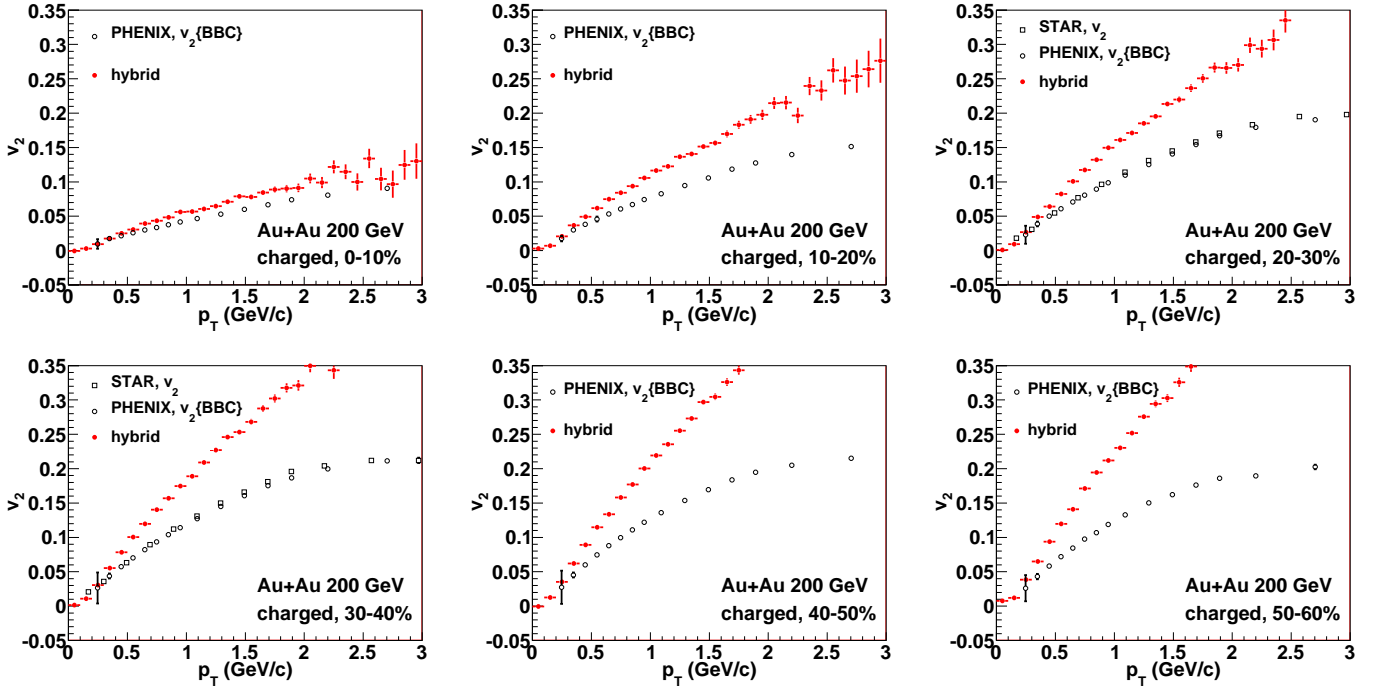


Figure 35: The same as Fig. 33 but using the KLN model initial conditions.

Using these angles, one obtains n -th harmonics

$$v_n^{\text{obs}} = \frac{1}{\langle N^P + N^N \rangle} \left\langle \sum_P \cos n(\phi_i - \Psi_n^B) + \sum_N \cos n(\phi_i - \Psi_n^A) \right\rangle \quad (62)$$

where $\langle \dots \rangle$ denotes the event average. N^P (N^N) is the number of particles in the positive (negative) rapidity region. Since the finite number of measured particles limits resolution in estimating the event plane angle Ψ_n , one has to consider the so-called resolution parameter \mathcal{R}_n

$$\mathcal{R}_n = \langle \cos n(\Psi_n - \Psi_n^{\text{true}}) \rangle, \quad (63)$$

where Ψ_n is the event angle estimated using the measured particle and Ψ_n^{true} is an ideal event plane angle corresponding to the infinite number of measured particles. In this event plane method, the resolution

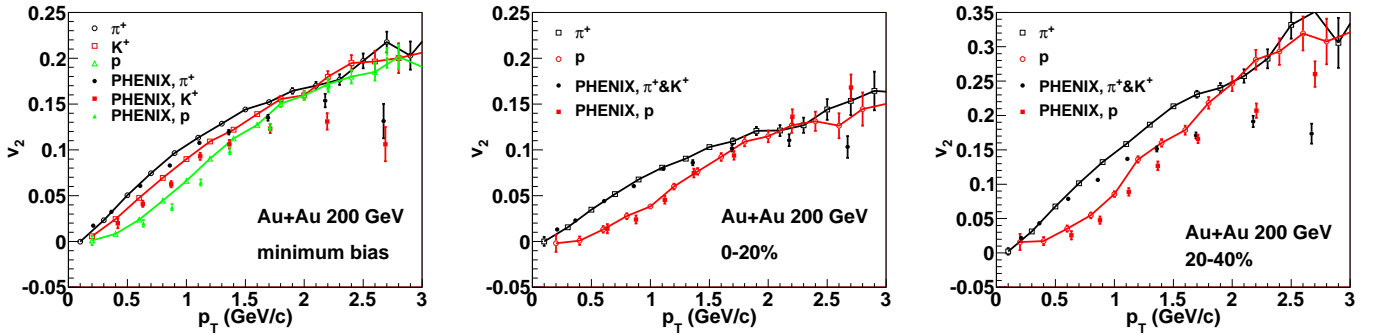


Figure 36: Transverse momentum dependence of v_2 of identified hadrons with respect to participant plane using the Glauber model initial conditions are compared with the PHENIX data [6] in minimum bias (left), and in 0-20% (middle) and 20-40% (right) centralities.

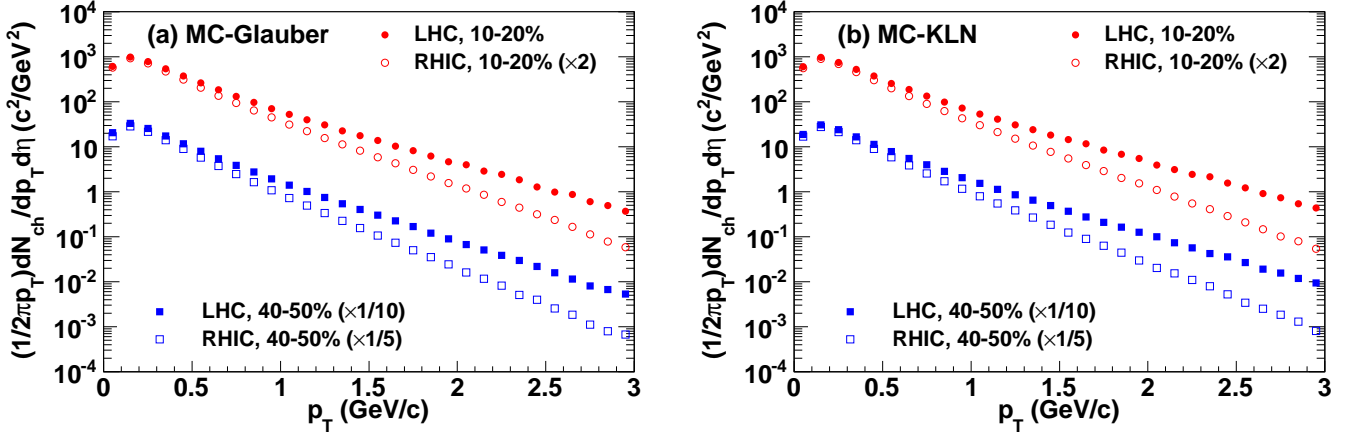


Figure 37: Transverse momentum distribution of charged hadrons at 10-20% (circles) and 40-50% (squares) centralities in Pb+Pb collisions at $\sqrt{s_{NN}} = 2.76$ TeV (filled symbols) and in Au+Au collisions at $\sqrt{s_{NN}} = 200$ GeV (open symbols). Results were calculated using (a) the MC-Glauber initialisation and (b) the MC-KLN initialisation. For the sake of comparison and visibility, the spectra are scaled by 2, 1/10, and 1/5 for 10-20% at RHIC, 40-50% at LHC and 40-50% at RHIC, respectively. Figures are from Ref. [54].

factor can be estimated as

$$\begin{aligned}
\langle \cos n(\Psi_n^A - \Psi_n^B) \rangle &= \langle \cos n(\Psi_n^A - \Psi_n^B) \rangle \\
&= \langle \cos n(\Psi_n^A - \Psi_n^{\text{true}} + \Psi_n^{\text{true}} - \Psi_n^B) \rangle \\
&= \langle \cos n(\Psi_n^A - \Psi_n^{\text{true}}) \cos n(\Psi_n^B - \Psi_n^{\text{true}}) \rangle - \langle \sin n(\Psi_n^A - \Psi_n^{\text{true}}) \sin n(\Psi_n^B - \Psi_n^{\text{true}}) \rangle \\
&= \langle \cos n(\Psi_n^A - \Psi_n^{\text{true}}) \rangle \langle \cos n(\Psi_n^B - \Psi_n^{\text{true}}) \rangle \\
&= \mathcal{R}_n^2
\end{aligned} \tag{64}$$

Here we have assumed that the two groups are symmetrically located with respect to midrapidity like the pseudorapidity regions A and B so that multiplicities in the two groups are almost equal and independent in a sense that two-particle correlation function between a particle from region A and the one from region B can be factorised into two one-particle distribution functions. Thus,

$$\langle \cos n(\Psi_n^A - \Psi_n^{\text{true}}) \rangle = \langle \cos n(\Psi_n^B - \Psi_n^{\text{true}}) \rangle \equiv \mathcal{R}_n \tag{65}$$

Thus the anisotropic parameters using the event plane method become

$$v_n\{\text{EP}\} = \frac{v_n^{\text{obs}}}{\mathcal{R}_n}, \tag{66}$$

$$\mathcal{R}_n = \sqrt{\langle \cos n(\Psi_n^A - \Psi_n^B) \rangle}. \tag{67}$$

Figure 40 (left) shows the resolution parameter \mathcal{R}_n ($n = 2, 3, 4$ and 5) as a function of centrality. Event plane resolution for the second harmonics reaches almost unity in mid central collisions (20-30 %) and is relatively better than the others as expected from the almond-like geometry on average. The other event plane resolutions become worse as decreasing multiplicity and increasing the order n . To understand the origin of the event plane, we also calculate correlation of angles between the orientation angle Φ_n (see Eg. (37)) and the true event plane

$$\begin{aligned}
\mathcal{C}_n(\Psi_n^{\text{true}}, \Phi_n) &= \langle \cos n(\Psi_n^{\text{true}} - \Phi_n) \rangle \\
&= \frac{\langle \cos n(\Psi_n^{A/B} - \Phi_n) \rangle}{\mathcal{R}_n}.
\end{aligned} \tag{68}$$

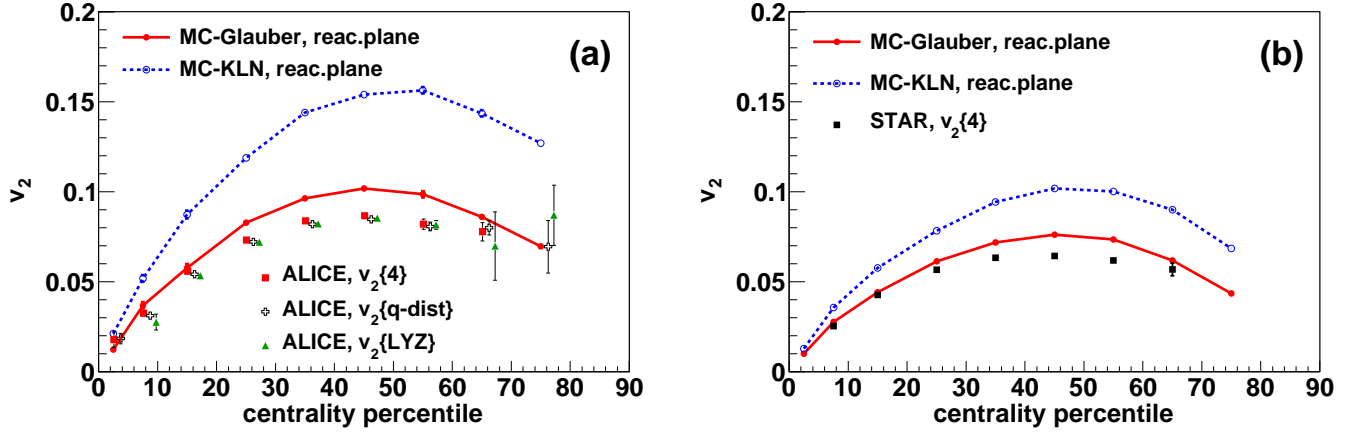


Figure 38: Centrality dependence of v_2 for charged hadrons with respect to reaction plane (model “A”) in Pb+Pb collisions at $\sqrt{s_{NN}} = 2.76$ TeV (left) and in Au+Au collisions at $\sqrt{s_{NN}} = 200$ GeV (right) is compared with the ALICE [11] ($0.2 < p_T < 5$ GeV/ c and $|\eta| < 0.8$). and STAR $v_2\{4\}$ data ($0.15 < p_T < 2$ GeV/ c and $|\eta| < 1$), respectively. Figures are from Ref. [54].

Since the number of produced particles is finite, the resolution parameter to correct $\Psi_n^{A/B}$ plays again an essential role in evaluating \mathcal{C}_n . When the anisotropic flow is generated by anisotropic pressure gradient in the transverse plane, the correlation becomes ~ -1 : In the case of positive elliptic flow generated from a conventional smooth almond-like profile elongated in y direction, $\Psi_2^{\text{true}} \sim 0$ and $\Phi_2 \sim \pi/2$ and, consequently, $\mathcal{C}_2 \sim -1$. Figure 40 (right) shows \mathcal{C}_n ($n=2, 3, 4$ and 5) as a function of centrality. \mathcal{C}_n for $n=2$ and 3 are close to -1 . So one can interpret anisotropic flow v_n ($n=2$ or 3) as generated by the corresponding anisotropy ε_n of the pressure gradient. While \mathcal{C}_4 and \mathcal{C}_5 start from -1 in very central collisions, increase with centrality percentile and even become positive above 30% centrality. This indicates the possibility of having finite v_n owing to ε_m ($m \neq n$).

To further investigate the origin of the event plane, we also calculate mixed correlations

$$\begin{aligned} \mathcal{C}_{nm}(\Psi_n^{\text{true}}, \Phi_m) &= \langle \cos n(\Psi_n^{\text{true}} - \Phi_m) \rangle, \\ \mathcal{C}_{nn} &= \mathcal{C}_n. \end{aligned} \quad (69)$$

Figure 41 shows \mathcal{C}_{42} together with \mathcal{C}_2 and \mathcal{C}_4 in Pb+Pb collisions at $\sqrt{s_{NN}} = 2.76$ TeV. If v_4 is generated solely by ε_2 , $|\Psi_4 - \Phi_2|$ is expected to be either 0 or $\pi/4$ due to symmetry in the transverse plane and, consequently, $\mathcal{C}_{42} = 1$ or -1 . In central collisions where the reaction zone is almost cylindrical on average, there is almost no correlation between Ψ_4 and Φ_2 . However, the correlation between them increases towards unity as increasing centrality percentage, which indicates $\Psi_4 \approx \Phi_2 \pm n\pi/2$ (n : integer) and v_4 is partly generated by ε_2 like positive elliptic flow in non central collisions [133, 215, 242].

Relations between initial geometry fluctuation and final anisotropic flow were discussed in Ref. [133]. They found that v_4 decreases with increasing ε_2 and changes its sign from positive to negative (see Fig. 17 in Ref. [133]). The behaviour is quite similar to our finding that the centrality dependence of \mathcal{C}_{42} changes also its sign. Distributions of $\Psi_n - \Phi_n$ for $n=4$ and 5 at the RHIC energy were investigated in Fig. 8 in Ref. [215]. Contrary to the cases for $n=2$ and 3 , the distributions for $n=4$ and 5 have a peak at $\Psi_n - \Phi_n = 0$ only in central collisions. Peak structure gradually disappears as moving to peripheral collisions and eventually another peak appears at $\Psi_n - \Phi_n = \pi/n$ in the peripheral collisions (50-60% centrality). These results also suggest that v_n s at least $n=4$ and 5 are generated by other order of initial geometry ε_m ($m \neq n$).

Before showing detailed results from event-by-event hydrodynamic simulations, we make two remarks here: Since the event plane is often determined using particles in forward and backward rapidity regions

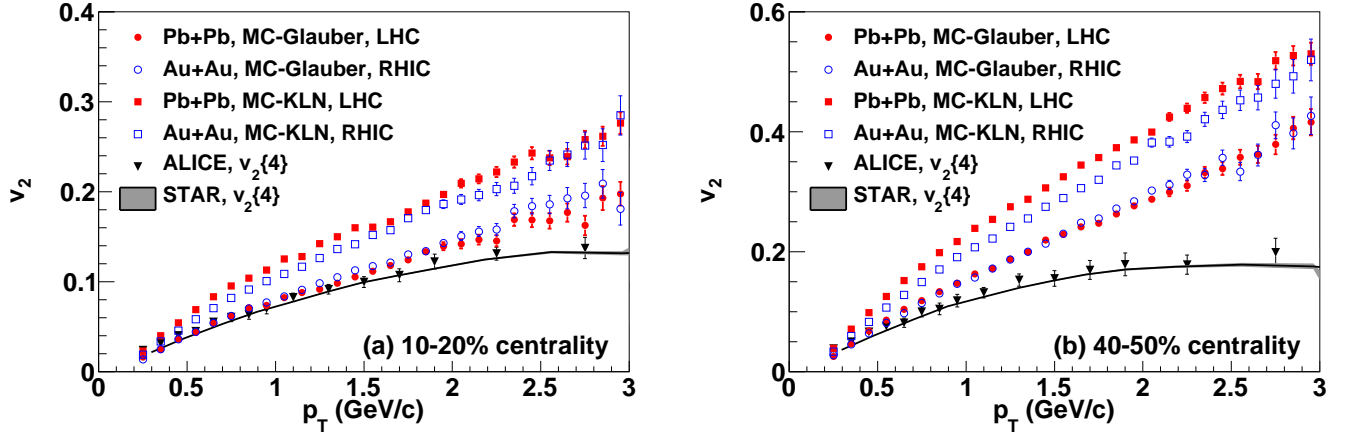


Figure 39: Transverse momentum dependence of v_2 of charged hadrons with respect to reaction plane in $\sqrt{s_{NN}} = 2.76$ TeV Pb+Pb collisions in 10-20% (left) and 40-50% (right) centralities. Figures are from Ref. [54].

(also known as “ η -subevent method”), full three dimensional dynamical simulations are essential if one wants to do the flow analysis in the same way than in experiments. For example, the PHENIX Collaboration at RHIC utilises the Beam Beam Counter (BBC) or the reaction plane detector (RxnP) in forward and backward rapidity regions to determine event planes. If one assumes boost invariance in dynamical calculations, one cannot perform this kind of flow analysis exactly.

Second, the effect of experimental event plane resolution cannot be properly evaluated unless one samples a finite number of particles at particleisation. The Cooper-Frye formula [86] has been conventionally used to calculate particle spectra in hydrodynamic calculations, but it gives smooth and continuous function of momentum distributions. This corresponds to the N times over-sampling of particles from a fluid element with $N \rightarrow \infty$ limit, which is, however, not adequate if event-by-event hydrodynamic simulations are supposed to describe actual events.

4.2 Multi-particle cumulants

In the previous subsection, we described the method to calculate anisotropic parameters with respect to the event plane. In this subsection, we discuss how to calculate anisotropic parameter using the particle ensemble itself, namely, the multi-particle cumulant method [64, 65].

We first define a $2p$ -particle correlation to calculate the n -th order of higher harmonics as

$$c_n\{2p\} = \langle \exp[in(\phi_1 + \phi_2 + \dots + \phi_p - \phi_{p+1} - \dots - \phi_{2p})] \rangle \quad (70)$$

where ϕ_i is azimuthal angle of the i -th particle under consideration. In this subsection, $\langle \dots \rangle$ means an average taken in two steps: First, one averages over all possible permutations of p particles in the same event, then one averages over all events. For example, two-particle correlations can be written as $c_n\{2\} = \langle e^{in(\phi_1 - \phi_2)} \rangle$.

We next define the corresponding cumulant. Correlations among $2p$ particles can be in general decomposed into a sum of correlations among smaller number of particles and cumulants. The simplest example is two-particle cumulant

$$\begin{aligned} c_n\{2\} &= d_n\{2\} + \langle e^{in\phi_1} \rangle \langle e^{-in\phi_2} \rangle \\ &= \langle e^{in(\phi_1 - \phi_2)} \rangle. \end{aligned} \quad (71)$$

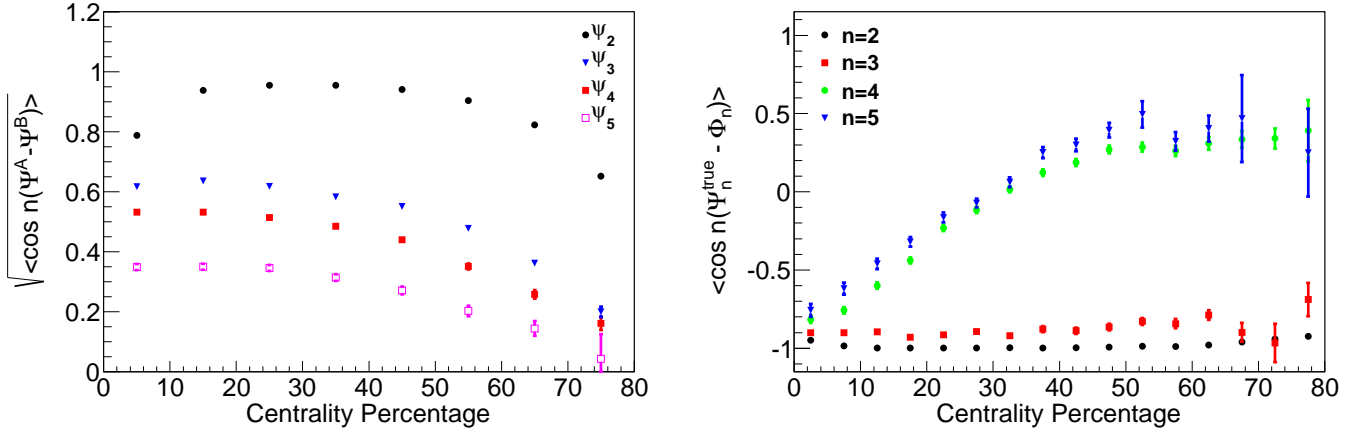


Figure 40: (Left) Resolution parameter defined in Eq. (67) for $n = 2, 3, 4$ and 5 as a function of centrality. (Right) Correlation $\langle \cos n(\Psi_n^{\text{true}} - \Phi_n) \rangle$ between the true event plane and the participant plane as a function of centrality in Pb+Pb collisions at $\sqrt{s_{NN}} = 2.76$ TeV.

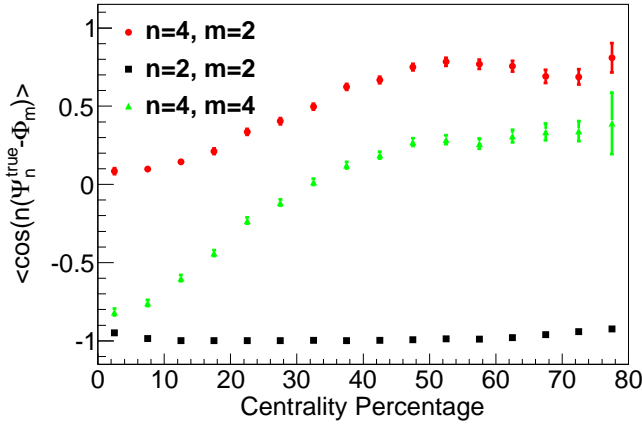


Figure 41: Mixed correlation between the true event plane Ψ_n^{true} and the orientation angle Φ_m as a function of centrality in Pb+Pb collisions at $\sqrt{s_{NN}} = 2.76$ TeV.

Due to symmetry, a term $\langle e^{in\phi_1} \rangle$ should vanish. As we see, a two-particle cumulant reduces to the corresponding two-particle correlation. This quantity contains correlation from collective flow as well as the so-called non-flow effects such as two-body decays of resonance particles. The next non-trivial and important example is four-particle cumulant:

$$\begin{aligned}
 c_n\{4\} &= \langle \exp[in(\phi_1 + \phi_2 - \phi_3 - \phi_4)] \rangle \\
 &= \langle e^{in(\phi_1 - \phi_3)} \rangle \langle e^{in(\phi_2 - \phi_4)} \rangle + \langle e^{in(\phi_1 - \phi_4)} \rangle \langle e^{in(\phi_2 - \phi_3)} \rangle + d_n\{4\} \\
 &= 2c_n\{2\}^2 + d_n\{4\}.
 \end{aligned} \tag{72}$$

Although $d_n\{4\}$ still contains non-flow effects of correlations among four particles, this does not contain non-flow effects from two-particle correlations and, consequently, is expected to contain much information about the anisotropic flow. In fact, it was shown in Ref. [65] that these cumulants are related with higher order anisotropic flow. So one can define higher order anisotropic parameter using $2p$ -particle

cumulants as

$$v_n\{2\}^2 = d_n\{2\}, \quad (73)$$

$$v_n\{4\}^4 = -d_n\{4\}. \quad (74)$$

Since this method requires many particles to take correlations/cumulates, the statistical errors tend to be large. Even 10^5 events are not enough: It happens that error bars are too large to show the results in our statistics, which indicates the necessity of massive numerical simulations.

In the actual calculations, we evaluate the above correlations as follows: We first calculate the following two quantities:

$$q_n = \frac{1}{\sqrt{M}} \sum_{i=1}^M e^{in\phi_i}, \quad (75)$$

$$u_n = \frac{1}{M} \sum_{i=1}^M e^{in\phi_i}. \quad (76)$$

q_n is a flow vector and u_n is the one with different normalisation. When the non-flow effects can be neglected, $v_n \approx \sqrt{u_n^* u_n}$. In the case of $2p$ -particle correlations, one needs to average over all possible permutations excluding self-correlation terms and take a sum such as

$$\begin{aligned} \sum_{(i,j)} &= \sum_{i=1}^M \sum_{j=1}^M (1 - \delta_{ij}) \\ &= \sum_{i=1}^M \sum_{j=1}^M - \sum_{i=j=1}^M, \end{aligned} \quad (77)$$

$$\begin{aligned} \sum_{(i,j,k)} &= \sum_{(i,j)} \sum_{k=1}^M (1 - \delta_{ki} - \delta_{kj}) \\ &= \sum_i \sum_j \sum_k - \sum_{i=j=1}^M \sum_{k=1}^M - \sum_{j=k=1}^M \sum_{i=1}^M - \sum_{k=i=1}^M \sum_{j=1}^M + 2 \sum_{i=j=k=1}^M, \end{aligned} \quad (78)$$

$$\sum_{(i,j,k,l)} = \sum_{(i,j,k)} \sum_{l=1}^M (1 - \delta_{li} - \delta_{lj} - \delta_{lk}). \quad (79)$$

In this way, correlation functions reduce to [94]

$$\begin{aligned} c_n\{2\} &= \frac{\langle \sum_{i=1}^M e^{in\phi_i} \sum_{j=1}^M e^{in\phi_j} - \sum_{i=j=1}^M e^{in(\phi_i - \phi_j)} \rangle}{\langle M(M-1) \rangle} \\ &= \frac{\langle |u_n|^2 M^2 - M \rangle}{\langle M^2 - M \rangle}, \end{aligned} \quad (80)$$

$$\begin{aligned} c_n\{4\} &= \frac{\langle U_4 M^4 - 6U_3 M^3 + 11U_2 M^2 - 6M \rangle}{\langle M(M-1)(M-2)(M-3) \rangle}, \\ &= \frac{\langle U_4 M^4 - 6U_3 M^3 + 11U_2 M^2 - 6M \rangle}{\langle M^4 - 6M^3 + 11M^2 - 6M \rangle}, \end{aligned} \quad (81)$$

where

$$U_4 = |u_n|^4, \quad (82)$$

$$6U_3 = 4|u_n|^2 + u_{2n}^* u_n^2 + u_{2n} u_n^{*2}, \quad (83)$$

$$11U_2 = 8|u_n|^2 + |u_{2n}|^2 + 2. \quad (84)$$

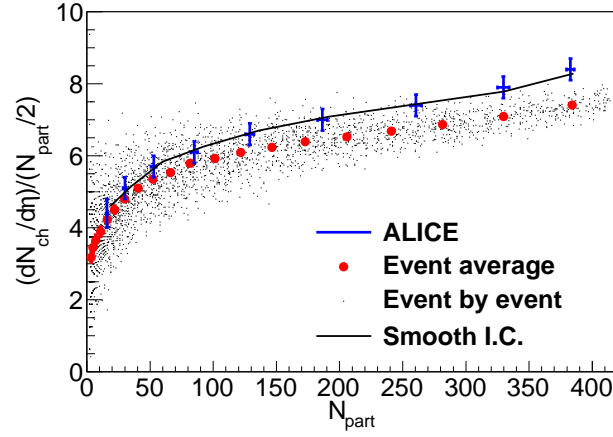


Figure 42: $(dN_{\text{ch}}/d\eta)/(N_{\text{part}}/2)$ in $|\eta| < 0.8$ as a function of N_{part} in Pb+Pb collisions at $\sqrt{s_{NN}} = 2.76$ TeV for each event and for events averaged over every 5% centrality. Here we use impact parameter to categorise the centrality for simplicity and plot results at $\langle N_{\text{part}} \rangle$ for each centrality. To exhibit how this quantity distributes event-by-event, results from 3000 minimum bias events are shown. Result from the smooth initial condition with the same initial parameter set is also shown in thin solid line. Experimental data are from ALICE Collaboration [183].

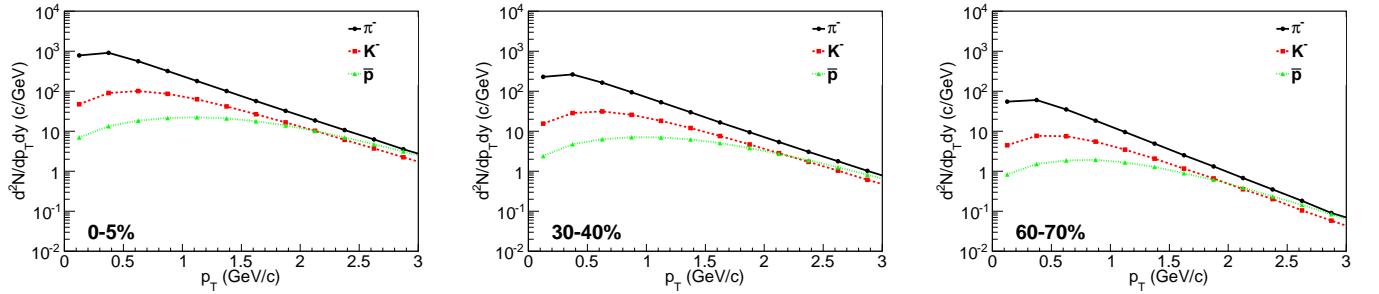


Figure 43: p_T distribution of identified hadrons at midrapidity in Pb+Pb collisions at $\sqrt{s_{NN}} = 2.76$ TeV at 0-5% (left), 30-40% (middle) and 60-70% (right) centralities.

4.3 Results

First, in Fig. 42, we show $(dN_{\text{ch}}/d\eta)/(N_{\text{part}}/2)$ as a function of N_{part} from event-by-event hydrodynamic simulations employing MC-KLN initialisation and compare them with ALICE data [183]. For comparison, we average over these events at every 5 % centrality. Although we used the same, adjusted parameter set as in the smooth initial conditions using the MC-KLN initialisation which reproduces the ALICE data reasonably well, results are systematically smaller than the data, in particular, in central events. In this paper, we do not try to fine-tune initial parameters. It would be interesting to see how the effects of the fluctuations of the gluon production itself would change this behaviour. In principle these fluctuations can be included using the negative binomial distribution (N.B.D.) [133, 166, 167, 175], but since the rapidity dependence of the required N.B.D. is not known, it is not clear how to implement these fluctuations in a fully three dimensional calculations.

In Fig. 43, p_T distributions of π^- , K^- and \bar{p} using the MC-KLN initialisation in Pb+Pb collisions at the LHC energy are shown at 0-5%, 30-40% and 60-70% centralities. Anti-proton yield becomes comparable with negative pion yields at $p_T \sim 3$ GeV/c in all these results, which is consistent with

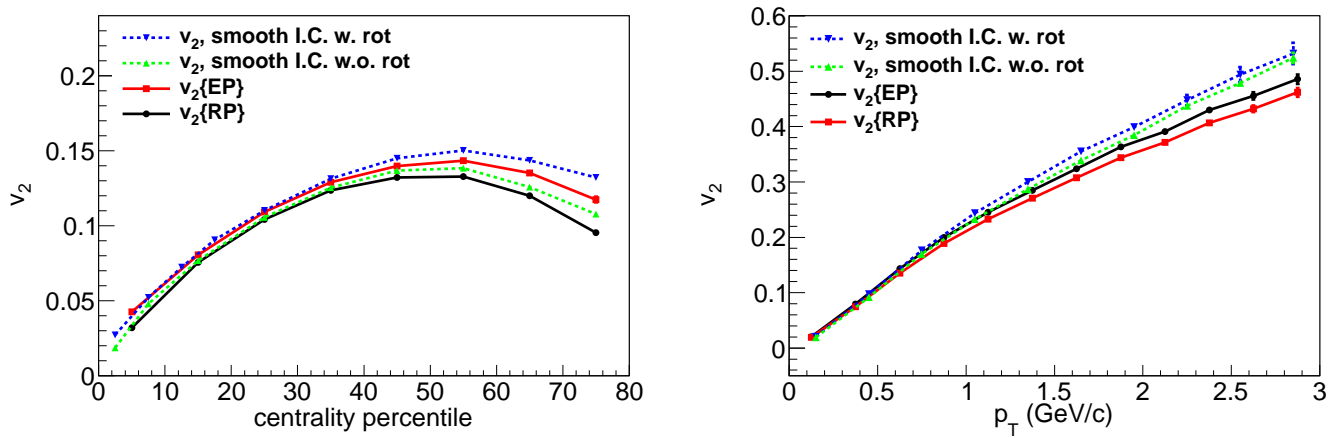


Figure 44: Centrality (left) and transverse momentum (right) dependences of v_2 of charged hadrons in Pb+Pb collisions at $\sqrt{s_{NN}} = 2.76$ TeV using smooth initial conditions with (inverse triangle) or without (triangle) shifting the centre of mass and rotation to match participant plane angle. These are compared with $v_2\{\text{EP}\}$ (square) and $v_2\{\text{RP}\}$ (circle) (see the text). Transverse momentum dependence is shown at 40-50% centrality.

the preliminary ALICE data [69]. Thus the switching temperature $T_{\text{sw}} = 155$ MeV, which affects both particles yields and the slopes of the p_T spectra, and was adjusted to reproduce particle ratios of identified hadrons at RHIC, works reasonably well at the LHC energy too. Detailed comparison of these results with the data would give more precise information about the switching temperature.

We compare the results of v_2 from event-by-event hydrodynamic simulations with those from hydrodynamic simulations with conventional, smooth initial conditions. Figure 44 (left) shows centrality dependence of p_T -integrated v_2 ($0 < \eta < 1$) of charged hadrons in Pb+Pb collisions at $\sqrt{s_{NN}} = 2.76$ TeV using MC-KLN initialisation. Although the difference between $v_2\{\text{EP}\}$ and v_2 from event-averaged initial conditions with shift of the centre of mass and rotation of participant plane discussed in the previous section is hardly seen in central to semi-central collisions (0 - 40%), the two results deviate from each other above $\sim 40\%$: $v_2\{\text{RP}\}$, which is v_2 with respect to the reaction plane in event-by-event simulations (reaction plane method), is slightly smaller than v_2 from event averaged initial conditions and the difference increases with increasing centrality percentile. This is also the case for the difference between $v_2\{\text{RP}\}$ and v_2 from event-averaged initial conditions without shift of the centre of mass or rotation of participant plane. Figure 44 (right) shows p_T dependence of v_2 for charged hadrons in the same collision system at 40-50% centrality. In both cases, there is almost no difference between event-by-event simulations and simulations with event-averaged initial conditions in the low p_T region. However, results deviate from each other gradually with increasing p_T above ~ 1 GeV/c [205]. From a point of view of conventional hydrodynamic simulations with smooth initial conditions, event-by-event simulations mimic shear viscous effects since shear viscosity reduces p_T -integrated v_2 and v_2 at high p_T [243].

Figure 45 shows event anisotropies v_n ($n=2, 3, 4$ and 5) by various flow analysis methods employed in this study. Centrality dependences of $v_n\{\text{EP}\}$ are almost identical to those of $v_n\{2\}$. $v_3\{\text{RP}\}$ and $v_5\{\text{RP}\}$ vanish as they should. $v_4\{\text{RP}\}$ is non-zero only in mid-central collisions (20-70% centrality). Since v_n using the four particle cumulant method demands higher statistics, we only show $v_2\{4\}$ and $v_3\{4\}$. Although $v_3\{4\}$ has large error bars, it seems to increase with increasing centrality percentage. This is contrary to $v_3\{\text{EP}\}$ and $v_3\{2\}$ which first increase up to 50-60% centrality, but begin to decrease in more peripheral collisions. This emphasises the importance of employing the same flow analysis method both in the theory calculations and in the experimental data analysis.

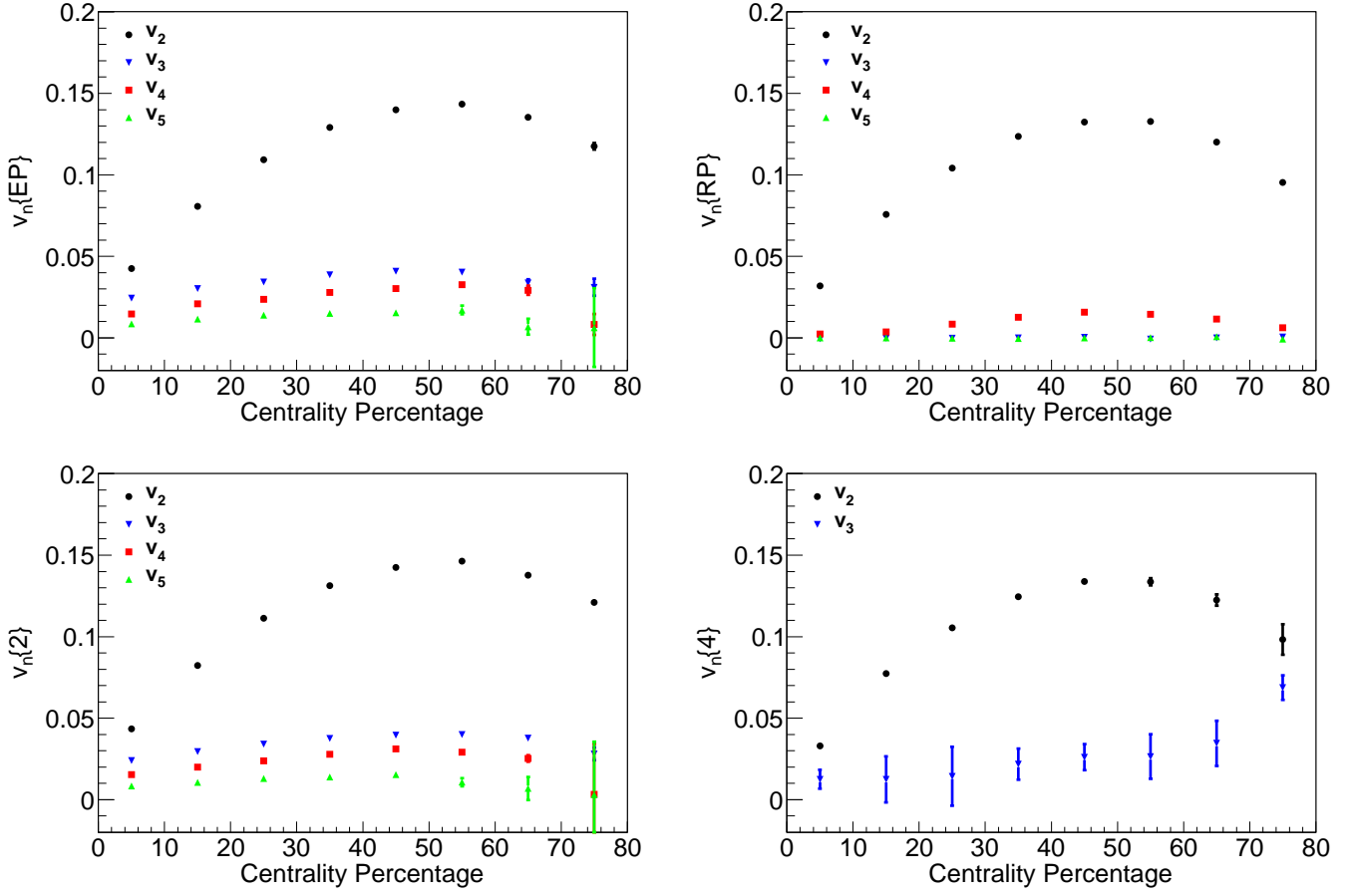


Figure 45: v_n using the event plane method (upper left), v_n using the reaction plane method (upper right) v_n using the two particle cumulant method (lower left) and v_n using the four particle cumulant method (lower right). $v_4\{4\}$ and $v_5\{5\}$ are omitted due to less statistics.

Figure 46 (left) shows the centrality dependence of v_2 compared with the ALICE data [11]. It has been known that ideal hydrodynamics with the CGC based initial state overshoots the data by 50-60%. The deviation could have been understood as viscous effects, which we do not discuss in this paper. It should be noted that the data do not contain charged hadrons below $p_T = 0.15$ GeV/c but that the hydrodynamic results do. If we took account of momentum cut of the ALICE setup, the calculated results would have become larger. Ratios of v_2 to $v_2\{EP\}$ are shown to see the difference among the various flow analysis methods in Fig. 46 (right). $v_2\{2\}$ is almost identical to $v_2\{EP\}$. On the other hand, $v_2\{RP\}$ almost traces $v_2\{4\}$. In central (0-10%) and peripheral (60-80%) collisions, $v_2\{RP\}$ and $v_2\{4\}$ are 10-20% smaller than $v_2\{EP\}$ and $v_2\{2\}$, which can be understood as a consequence of eccentricity fluctuations shown in Fig. 14. On the other hand, the difference between $v_2\{EP\}$ and $v_2\{RP\}$ is $\sim 5\%$ in semi-central collisions. Correspondences of between $v_2\{2\}$ and $v_2\{EP\}$ and between $v_2\{4\}$ and $v_2\{RP\}$ are also discussed using UrQMD in Ref. [244].

Figure 47 shows centrality dependence of v_3 (left) and its ratio to $v_3\{EP\}$ (right). If odd harmonics are generated solely by fluctuation in initial transverse profiles, $v_3\{RP\}$ should vanish since the initial fluctuation does not correlate with the reaction plane. This is, in fact, seen in Fig. 47. As seen in v_2 , $v_3\{EP\}$ is almost identical to $v_3\{2\}$. Due to poor statistics, $v_3\{4\}$ has large errors. Nevertheless, it seems to be finite and smaller than $v_3\{EP\}$ and $v_3\{2\}$ up to $\sim 60\%$ centrality: $v_3\{4\}$ is roughly half of $v_3\{2\}$ and $v_3\{EP\}$ [191, 192]. Ratios of v_3 to $v_3\{EP\}$ as functions of centrality are shown in Fig. 47 to see the dependence of v_3 on flow analysis methods more clearly. It would be interesting to gain more

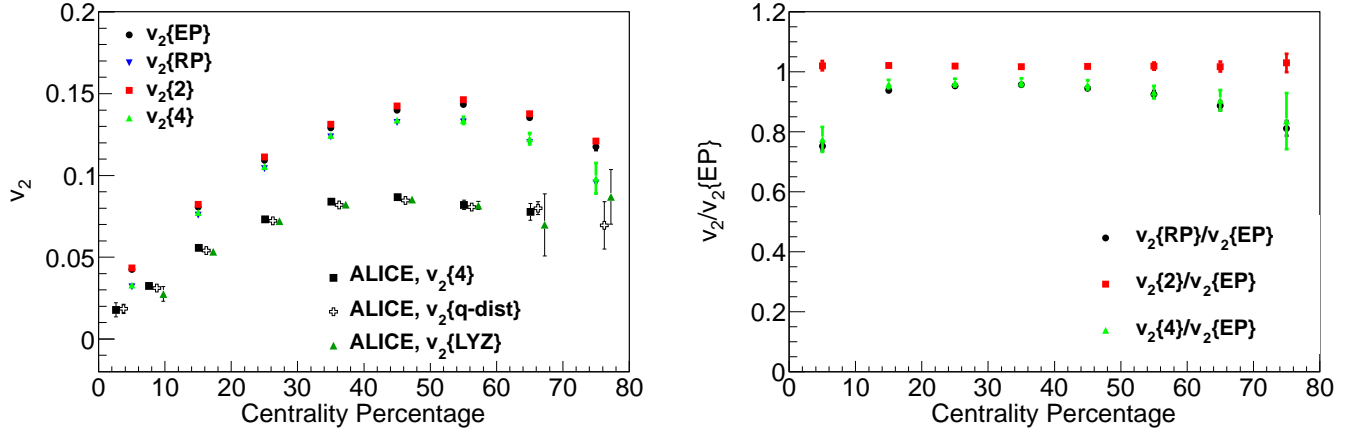


Figure 46: (Left) Centrality dependence of v_2 using the event plane method, the reaction plane method, the two particle cumulant and the four particle cumulant in MC-KLN initialisation compared with the ALICE data [11]. (Right) Ratio of v_2 to $v_2\{\text{EP}\}$ as a function of centrality.

statistics to confirm whether $v_3\{4\}$ differs from the other v_3 .

Figure 48 shows centrality dependence of ratios of fourth (left) and fifth (right) harmonics. Due to poor statistics, harmonics using the four particle cumulant method are omitted. Although $v_4\{2\}$ and $v_5\{2\}$ have large error bars, they seem to agree with the harmonics evaluated using the event plane method, in the same way $v_2\{2\}$ and $v_3\{2\}$ do. $v_4\{\text{RP}\}$ is finite, while $v_5\{\text{RP}\}$ vanishes as already seen in Fig. 45.

Figures 49, 50 and 51 show pseudorapidity dependence of higher order harmonics in 0-10%, 40-50% and 70-80% centrality, respectively. The second harmonics v_2 , which are shown in the left panels, always have a maximum at midrapidity and decrease as moving away from midrapidity although ε_2 is almost constant as a function of η_s . This triangular shape was also measured at the RHIC energy. As we discussed in Sec. 2.5 the rapidity dependence is easy to understand as a consequence of the space-time rapidity dependence of the initial energy density even if the initial eccentricity hardly depends on η_s (Fig. 18). The larger the initial density, the longer the lifetime of the low viscosity QGP phase where v_2 is built up much more efficiently than in the highly dissipative hadronic phase, see Fig. 7 and related discussion on page 15.

Difference between $v_2\{\text{EP}\}$ and $v_2\{\text{RP}\}$ is relatively large in central (0-10%) and peripheral (70-80%) collisions, whereas the difference is very small in semi-central collisions (30-40%). This difference at midrapidity was already shown in Fig. 46, but it persists up to $|\eta| \sim 5$. $v_4\{\text{EP}\}$ also depends on η even if $\varepsilon_4\{\text{PP}\}$ is almost independent of η_s as shown in Fig. 18.

Odd harmonics ($n=3$ and 5) shown in the right panel are finite near midrapidity when event plane method is used to evaluate them, whereas they vanish when the reaction plane method is used. The $v_3\{\text{EP}\}$ and $v_5\{\text{EP}\}$ have a broad peak at midrapidity, decrease as moving away from midrapidity and eventually vanish near the beam rapidity. Note that v_5 has large error bars in the 70-80% centrality due to small multiplicity. It should be noted that all $v_n\{\text{EP}\}(\eta)$ have almost no boost invariant region which is in good contrast to $\varepsilon_n(\eta_s)$ shown in Fig. 18. As mentioned, this can be understood as the space-time rapidity dependence of the lifetime of the QGP fluid.

Transverse momentum dependences of v_2 evaluated using the four methods described in this study are compared with the ALICE $v_2\{4\}$ data [11] at 40-50% centrality in Pb+Pb collisions at $\sqrt{s_{NN}} = 2.76$ TeV in Fig. 52. Up to $p_T \sim 1.5$ GeV/ c where, in the M -particle cumulant methods, at least M particles are binned in all events in this centrality, the difference among the four methods is very small. Above this, the difference between $v_2\{\text{EP}\}$ and $v_2\{\text{RP}\}$ is visible but still not so significant.

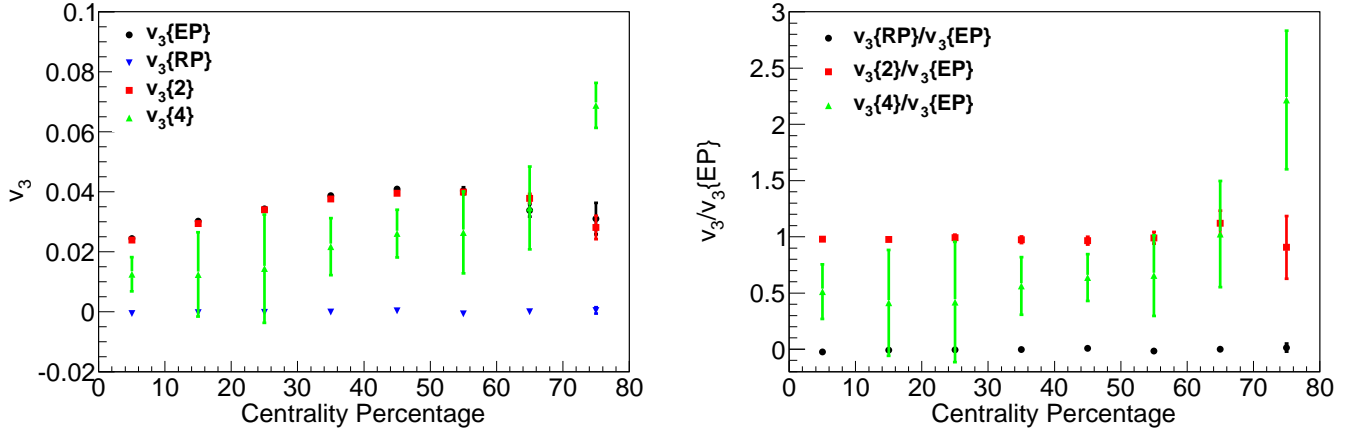


Figure 47: (Left) Centrality dependence of v_3 using the event plane method, the reaction plane method, the two particle cumulant and the four particle cumulant. (Right) Ratio of v_3 to $v_3\{\text{EP}\}$ as a function of centrality.

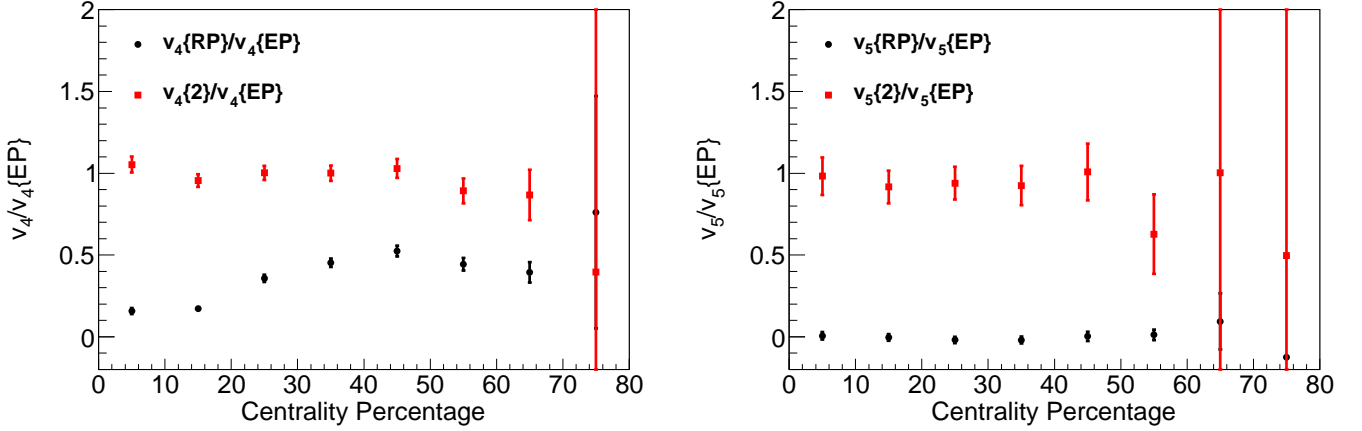


Figure 48: (Left) Ratio of v_4 to $v_4\{\text{EP}\}$ as a function of centrality. (Right) Ratio of v_5 to $v_5\{\text{EP}\}$ as a function of centrality.

Transverse momentum dependence of v_2 using the event plane method is compared with the ATLAS v_2 data [12] in Pb+Pb central (0-10%), semi-central (40-50%) and peripheral (70-80%) collisions in $0 < |\eta| < 1$ (top), $1 < |\eta| < 2$ (middle) and $2 < |\eta| < 2.5$ (bottom) at $\sqrt{s_{NN}} = 2.76$ TeV in Fig. 53. We emphasise here that we employ the same flow analysis method as the ATLAS Collaboration [12]. v_2 from event-by-event ideal hydrodynamic simulations overshoots the ATLAS data at all centralities regardless of the pseudorapidity regions.

Transverse momentum dependences of v_n ($n=2, 3, 4$ and 5) of charged hadrons at midrapidity are shown at 0-10% (Fig. 54), 40-50% (Fig. 55) and 70-80% (Fig. 56) centralities in Pb+Pb collisions at $\sqrt{s_{NN}}=2.76$ TeV. In each figure, results using the event plane method, the reaction plane method and the two-particle cumulant method are compared with each other. Due to the poor statistics, we omit the results from the four-particle cumulant method. In central collisions (0-10% centrality), all $v_n\{\text{EP}\}$ are close to each other. The magnitude and the order of $v_n\{2\}$ are almost identical to those of $v_n\{\text{EP}\}$. However, in the case of the reaction plane method, only v_2 is finite and the other harmonics vanish in $0 < p_T < 3$ GeV/c. In semi-central collisions (40-50% centrality), v_2 deviates from other harmonics,

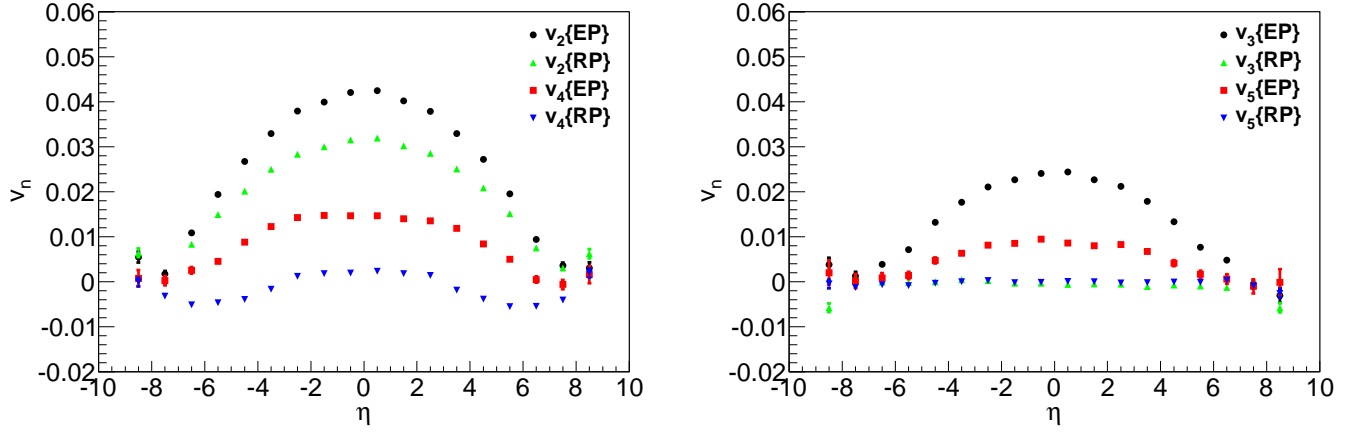


Figure 49: Pseudorapidity dependence of v_2 and v_4 (left) and v_3 and v_5 (right) at 0-10% centrality. Harmonics evaluated using the event plane method are compared with those evaluated with respect to the reaction plane.

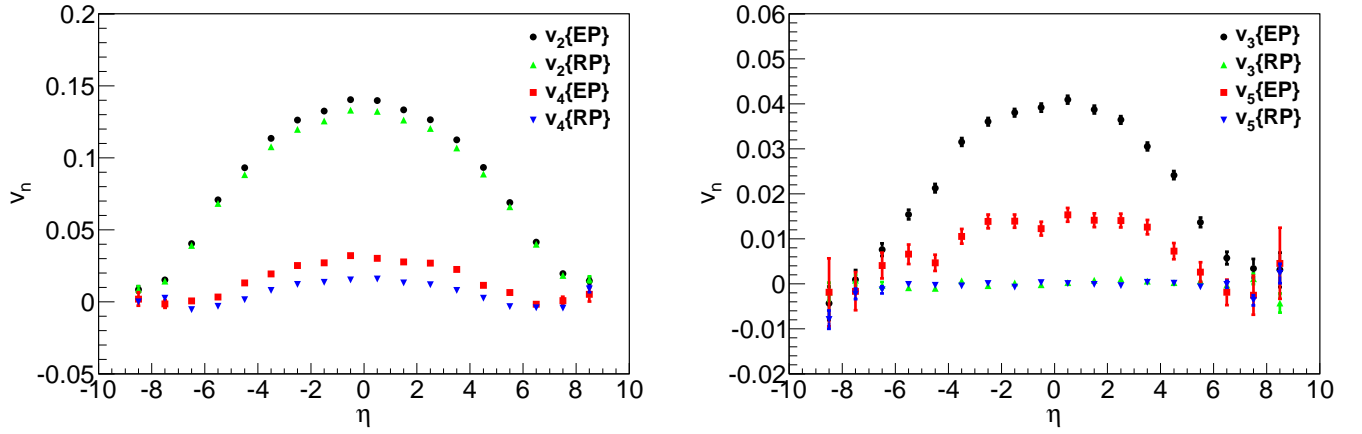


Figure 50: The same as Fig. 49 but at 40-50% centrality.

which reflects the almond like average geometry in non-central collisions. Again, the pattern of $v_n\{2\}$ is quite similar to that of $v_n\{EP\}$. v_2 using these three methods is almost the same, v_3 and v_5 vanish when the reaction plane method is used as expected from an argument of fluctuating initial conditions,¹⁴ whereas $v_4\{RP\}$ becomes finite although its magnitude is rather smaller than $v_4\{EP\}$ and $v_4\{2\}$. The sensitivity of v_4 on the analysis methods indicates that measured v_4 contains both fluctuation and geometry effects. In peripheral collisions, it is quite hard to obtain higher order harmonics with small errors for the given number of events since not only the number of events but also the number of measured particles do matter. In the event plane method, resolution parameter becomes worse with decreasing centrality, which, in turn, increases the errors of v_n^{obs} .

We also show $v_2\{EP\}$ and $v_3\{EP\}$ of identified hadrons (π^- , K^- and \bar{p}) in Figs. 57 and 58, respectively, at midrapidity ($|\eta| < 0.8$) at three centralities (0-5%, 30-40% and 60-70%) in Pb+Pb collisions at the LHC energy. Mass splitting pattern, namely $v_n^\pi > v_n^K > v_n^p$ for $n = 2$ and 3, is clearly seen in all results except in v_3 at 60-70% centrality where, due to smaller multiplicity, resolution is poor and,

¹⁴ Regarding v_5 , a more precise reason is still not clear since the correlation between Ψ_5 and Φ_5 is non-trivial as shown in Fig. 40.

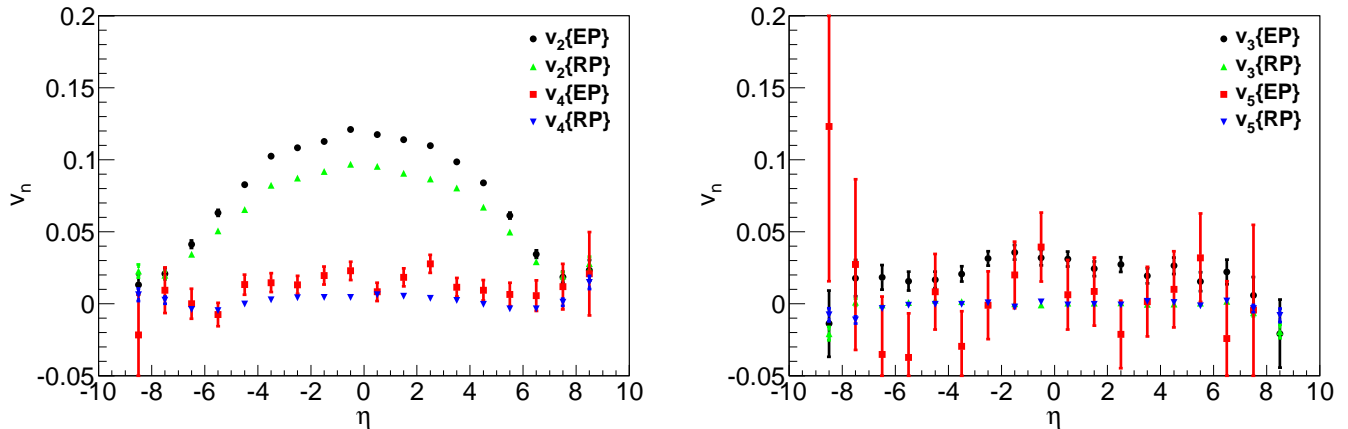


Figure 51: The same as Fig. 49 but at 70-80% centrality.

consequently, errors are very large. Similar mass splitting pattern was also found in Ref. [135], where it was pointed out that the mass splitting pattern is not necessarily a consequence of the existence of the QGP.

When radial flow is sufficiently large, v_2 of protons could be negative in the low p_T region [18]. However, this cannot be clearly seen even though radial flow at the LHC energy is expected to be larger than that at the RHIC energy. $v_n(p_T)$ for identified hadrons would give further constraints for the dynamical modelling at the LHC energy as well as at the RHIC energy.

So far we have shown the results obtained using the MC-KLN initialisation. We next compare these results with the ones obtained using the MC-Glauber initialisation. As already seen in the previous section, the MC-KLN model gives a larger eccentricity ε_2 than the MC-Glauber model and, consequently, leads to larger v_2 . This is again seen in Fig. 59 (left). Regardless of different models, v_3 using the MC-KLN model is almost identical to v_3 using the Glauber model. This is due to the fact that, in both models, v_3 is generated by triangular anisotropic shape of the reaction zone, ε_3 and that ε_3 is determined by the granular structure of the colliding nuclei as shown in Fig. 22. On the other hand, one cannot see the similarity of v_n ($n = 4, 5$) between the MC-KLN model and the MC-Glauber model in Fig. 59 (right). In semi-central collisions (10-60% centrality) v_n ($n = 4, 5$) using the MC-KLN model are systematically larger than the ones using the MC-Glauber model. In spite of a fact that higher order flow coefficients such as v_4 and v_5 are correlated with lower order flow coefficients as demonstrated in Fig. 41, simultaneous analyses of v_n ($n \lesssim 5$) can be used to discriminate between the CGC and Glauber pictures for the initial conditions and would thus help to provide useful information about the transport properties of the QGP. Although the simultaneous analysis of v_2 and v_3 revealed the MC-KLN model apparently contradicts to the PHENIX data [245], these calculations lack multiplicity fluctuations which would affect ε_n [175] and thus improve the fit to the data.

5 Conclusion

In this paper, we have performed simulations of relativistic heavy ion collisions at RHIC and LHC energies using an integrated approach of dynamical modelling, in which Monte-Carlo calculations of initial collisions based on the colour glass condensate or the Glauber pictures, a fully (3+1)-dimensional ideal hydrodynamic model with the state-of-the-art lattice QCD equation of state, and a hadronic cascade are combined.

We employed the Monte-Carlo versions of the Kharzeev-Levin-Nardi model and the Glauber model

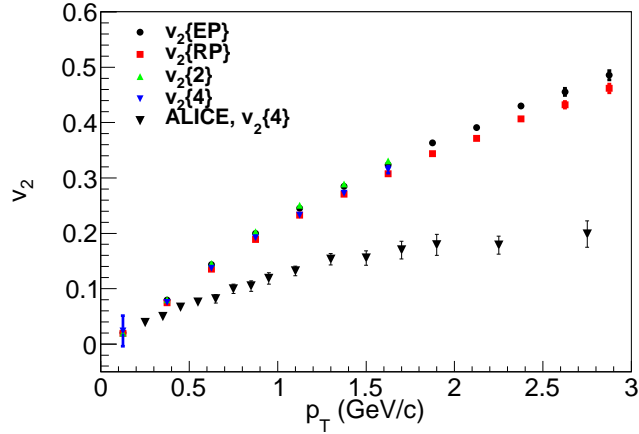


Figure 52: Transverse momentum dependence of v_2 using the event plane method, the reaction plane method, the two particle cumulant and the four particle cumulant calculated using MC-KLN initialisation compared with the ALICE $v_2\{4\}$ data at 40-50% centrality [11]. Due to the lack of statistics, results are shown up to 1.625 GeV/c for the two particle cumulant and the four particle cumulant methods.

and, using them, generated many events to obtain initial conditions for the subsequent hydrodynamic evolution. We had two options for initial conditions: One is the single smooth initial condition for a given centrality as we take an average of the entropy profiles in each centrality class. By rotating each initial profile to match its participant plane with the reaction plane, we obtained initial conditions containing some fluctuation effects. It turned out that these initial conditions are necessary to obtain large elliptic flow parameter in small systems, such as the matter created in Cu+Cu collisions, and in systems which are almost cylindrical on average, such as central events in Au+Au collisions. However, these initial conditions did not contain higher odd harmonic components and, therefore, could not lead to reproduction of anisotropic flow parameters with odd harmonics. We neglected the longitudinal structure of the created matter in this option and assumed boost invariance. Therefore, we could not discuss (pseudo-)rapidity dependence of observables.

The other option is to utilise each initial profile from the Monte-Carlo calculations on event-by-event basis. Since the entropy production in the primary nucleon-nucleon collision happens when the two nucleons in the colliding nuclei are sufficiently close in the transverse plane, the entropy density profile contains fluctuations from configuration of nucleons in the colliding nuclei. The resultant example of initial conditions exhibits a bumpy structure and contains also odd spatial anisotropies unlike in the first option. In this option, we also considered space-time rapidity dependence of initial conditions. The KLN model gives rapidity distribution of produced gluons through the k_T factorisation formulation. We simply identified the momentum rapidity distribution with the space-time rapidity distribution in the transverse plane to obtain initial conditions in the whole configuration space. The Glauber model does not tell us anything about the longitudinal structure of entropy production. We modelled initial longitudinal structure of entropy profile based on a string picture, which we called a modified BGK (Brodsky-Gunion-Kühn) model. In this model, the space-time rapidity dependence of entropy density was calculated using the numbers of participants and that of binary collisions as given by the Glauber model.

Using these initial conditions, we performed ideal hydrodynamic simulations solving the expansion numerically in all three dimensions using the Milne coordinates (τ, x, y, η_s) . For the equation of state, we used a model in which the lattice QCD results in high temperature regions are smoothly connected with a resonance gas equation of state with the same hadrons than the event generator JAM. The

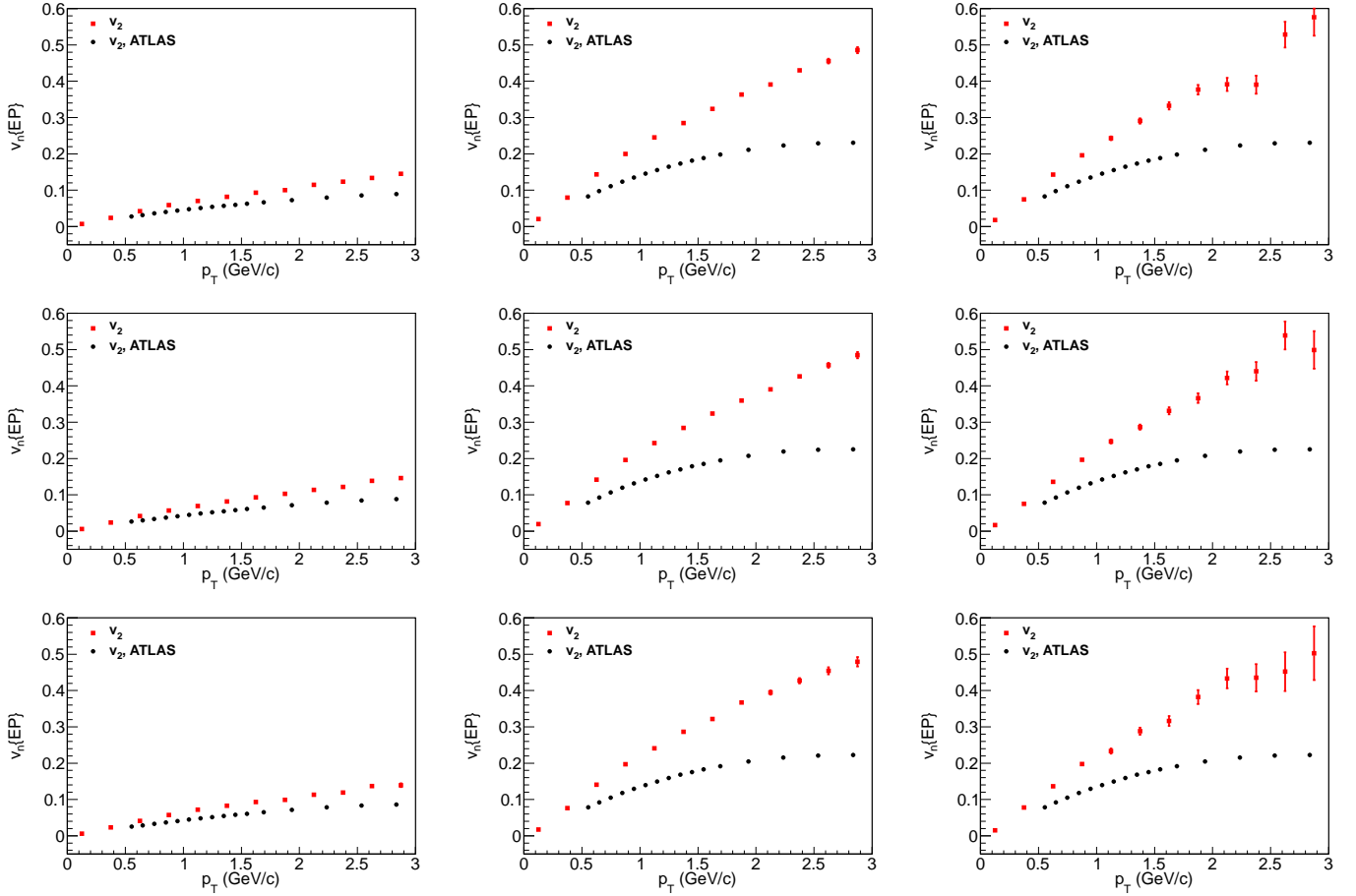


Figure 53: Transverse momentum dependence of v_2 of charged hadrons in $0 < |\eta| < 1$ (top), $1 < |\eta| < 2$ (middle) and $2 < |\eta| < 2.5$ (bottom) using the event plane method, and compared with the ATLAS data [12] at 0-10% (left), 40-50% (middle) and 70-80% (right) centralities.

resultant equation of states exhibits a crossover behaviour rather than a phase transition. We employed the Piecewise Parabolic Method to solve the hydrodynamic equations. This method has been known as a robust algorithm against strong shock waves, and is thus ideal for simulating fluid evolution starting from bumpy initial conditions on an event-by-event basis. We described the space-time evolution of the QGP fluids all the way down to the switching temperature. The switching temperature was chosen to reproduce the final particle ratios of pions, kaons and protons at the full RHIC energy. With the subsequent hadronic evolution, we found $T_{sw} = 155$ MeV leads to a good description of yields and slopes in transverse momentum distribution for identified hadrons at RHIC. From a macroscopic hydrodynamic picture to a microscopic particle picture at T_{sw} , we employed the Cooper-Frye formula rejecting in-coming particles which contribute as a negative number in the phase space. By sampling hadrons on the particlisation hypersurface according to this prescription, we obtained “initial” phase space distribution for the subsequent hadronic cascading on an event-by-event basis. We simulated the space-time evolution of hadron gas utilising a hadronic cascade, JAM. Transport models can naturally treat the late low density phase of the system in the heavy ion collision where the system is not expected to be in a local equilibrium any more, and provide a realistic freeze-out which depends on the particle species.

We simulated $\sim 10^5$ “minimum bias” events with $N_{part} \geq 2$ in the event-by-event option for each parameter set. We confirmed the average multiplicity in event-by-event simulations is smaller than the

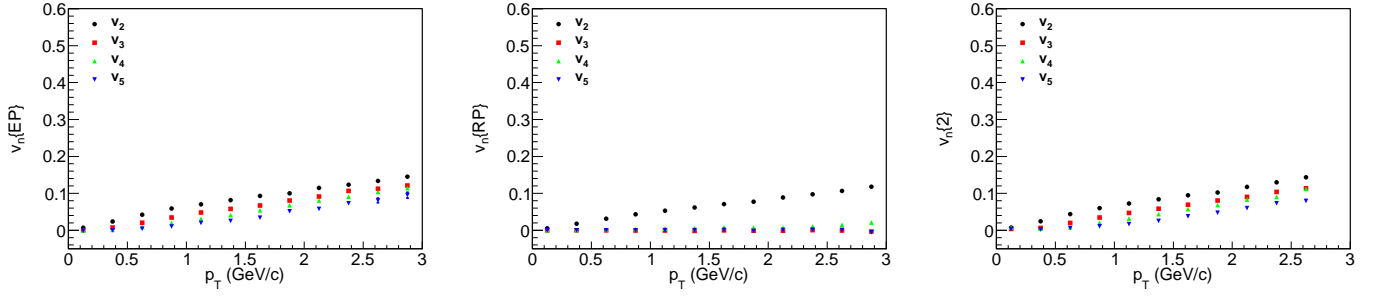


Figure 54: Transverse momentum dependence of harmonics, v_n ($n=2, 3, 4$ and 5), using the event plane method (left), the reaction plane method (middle), and the two particle cumulant method (right) at 0-10% centrality.

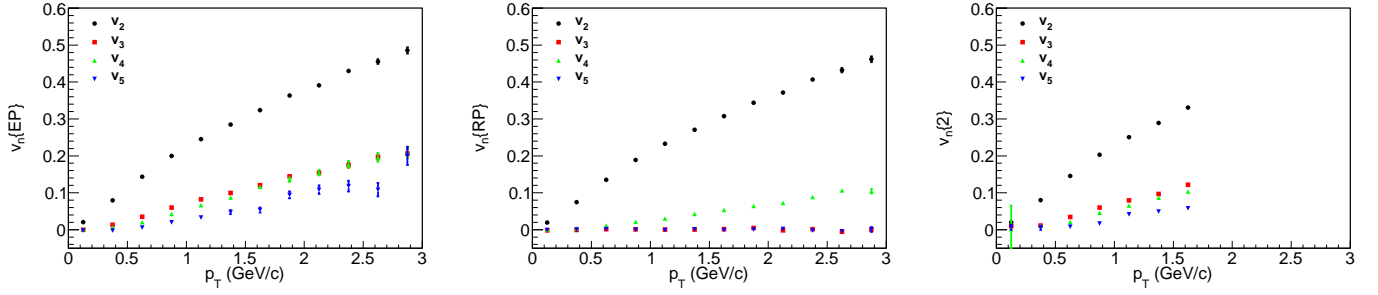


Figure 55: The same as Fig. 54 but at 40-50% centrality.

multiplicity using the smooth averaged initial conditions. We also obtained p_T spectra for identified hadrons and found anti-proton yields become comparable with negative pion yield at $p_T \sim 3$ GeV/c. So far comparisons of theoretical results using a flow analysis method have been made with experimental data obtained using the different flow analysis method. We analysed the final particle distribution in a spirit of performing (almost) the same procedure as the experimentalists have done. We used particle multiplicity in forward rapidity to perform centrality cuts. When we calculated the anisotropic flow parameters, we employed several typical flow analysis methods such as reaction plane method, event plane method and two- and four-particle cumulant methods.

We found that some of the different flow analysis methods lead to almost the same results. For instance, v_n using the event plane method is almost the same as v_n using the two-particle cumulant

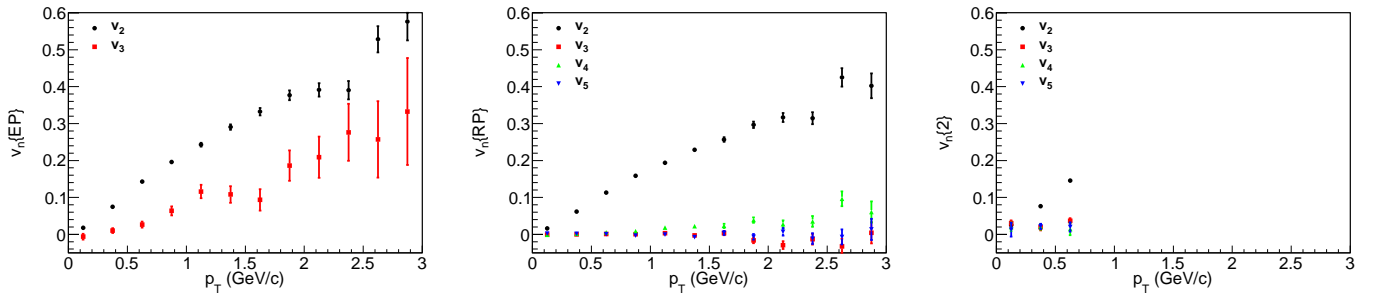


Figure 56: The same as Fig. 54 but at 70-80% centrality. v_4 and v_5 are omitted in the event plane method since the errors are too large due to poor resolution of the event plane angle.

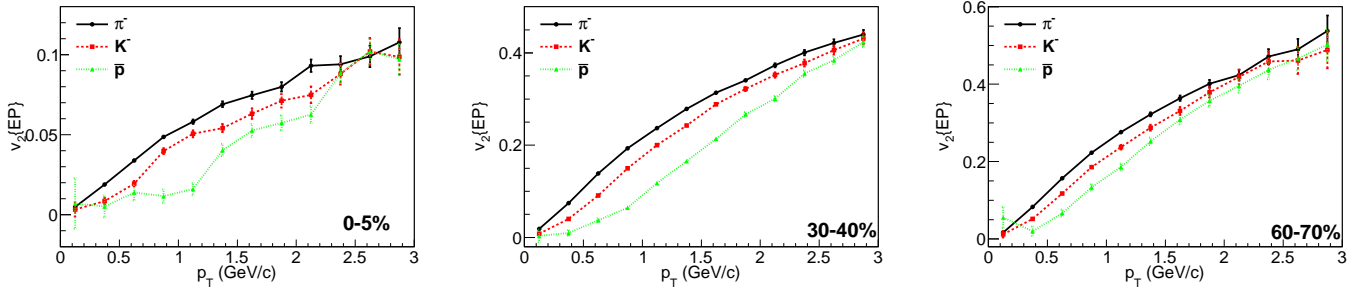


Figure 57: $v_2\{\text{EP}\}$ of identified hadrons in $|\eta| < 0.8$ in Pb+Pb collisions at $\sqrt{s_{NN}} = 2.76$ TeV. Results at 0-5% (left), 30-40% (middle) and 60-70% (right) centralities are shown.

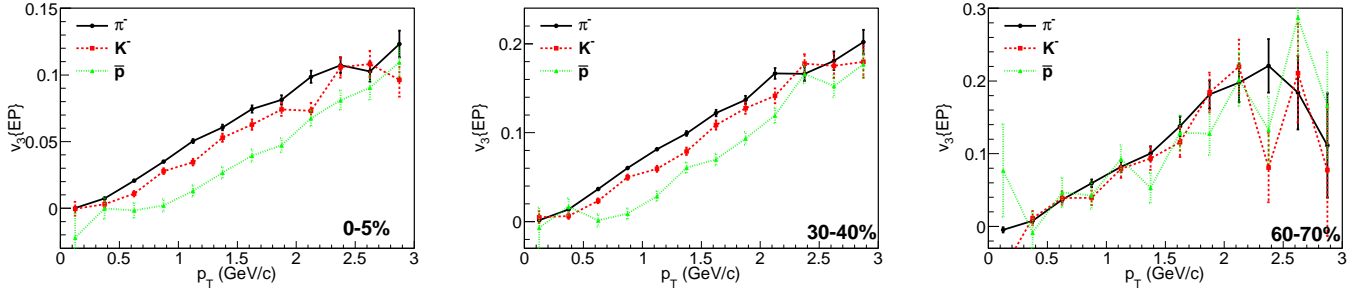


Figure 58: The same as Fig. 57 but for $v_3\{\text{EP}\}$.

method within errors. Notice that contributions from jet fragmentation were missing in our dynamical simulations, which omits one of the major non-flow effects in the two-particle cumulant method. On the other hand, the four-particle cumulant method gives different results. v_2 using the four-particle cumulant method is more like theoretically calculated v_2 with respect to the reaction plane. Although we did not have enough statistics to draw firm conclusions, in our calculations, v_3 using the four particle cumulant method was roughly half of v_3 obtained using the other two methods. v_2 using the event plane method contains effects of participant plane fluctuation: In the limit of vanishing centrality percentage, v_2 using the event plane method stays finite. v_{2n+1} are expected to vanish if measured with respect to the reaction plane. However, v_{2n+1} are finite due to fluctuating initial transverse profiles in the event plane method and the two-particle cumulant method.

We evaluated the correlations between the event plane and the orientation angles to see a possible mechanism of generating higher order anisotropic flow. For v_2 and v_3 , these two angles are strongly correlated: Anisotropic flow is generated mainly by pressure gradient in the direction of short axis in each participant anisotropy. On the other hand, non-trivial correlations are seen in v_4 and v_5 . v_4 is first driven by the fourth spatial anisotropy in central collisions, but could be driven by *elliptic flow* with respect to reaction plane in mid-central to peripheral collisions. This could be seen in the mixed correlation between Φ_2 and Ψ_4 .

We used two models of initial conditions, namely MC-KLN model and MC-Glauber model, and made a systematic comparison between them. Although entropy density profile is different in these two models, both models can lead to almost identical particle yields and p_T spectra. On the other hand, the spatial anisotropy ε_2 from the MC-KLN model is larger than the one from the MC-Glauber model, which leads to discrepancy of v_2 between the MC-KLN model and the MC-Glauber model. Within ideal hydrodynamic simulations, the difference can be seen in all v_2 results. However, ε_3 from the MC-KLN model is almost the same as the one from the MC-Glauber model because it originates

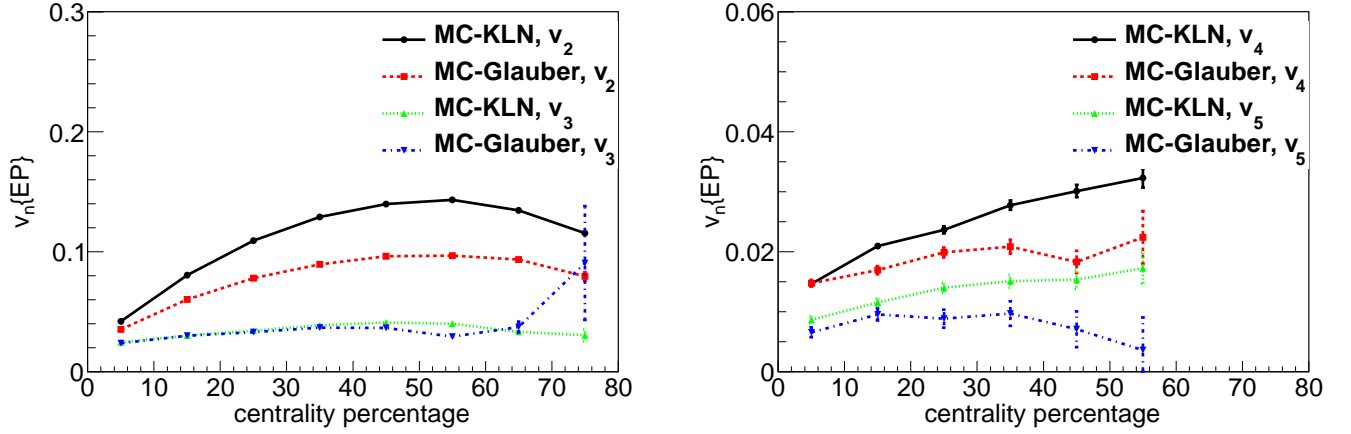


Figure 59: Centrality dependence of v_2 and v_3 (left) and v_4 and v_5 (left) of charged hadrons at midrapidity ($0 < \eta < 1$) in Pb+Pb collisions at $\sqrt{s_{NN}} = 2.76$ TeV. Results obtained using the MC-KLN model are compared with the ones obtained using the MC-Glauber model.

from initial fluctuation of transverse profiles, which is treated in a similar fashion in both models. Consequently, there is almost no difference of v_3 between these two models. As claimed by the PHENIX Collaboration [245], one can use this fact to discriminate the MC-KLN model from the MC-Glauber model. Simultaneous analyses of higher order anisotropies such as v_4 and v_5 , in addition to v_2 and v_3 , would also provide more information about the initial conditions.

In this paper, we restricted our discussion to ideal hydrodynamic description of the QGP fluids. However, to understand the transport properties of the QGP, viscous corrections to both dynamics and particle spectra are mandatory. So far, there have been several viscous hydrodynamic simulations to analyse anisotropic parameters at RHIC and LHC energies. Some of the simulations have been performed in (2+1) dimensional space with an assumption of boost invariance. However, given a fact that event planes are determined in forward rapidity regions in some flow analyses experimentally, fully three dimensional simulations are necessary to describe the actual dynamics.

Final higher harmonics were turned out to be sensitive to the flow analysis method. A good example was the triangular flow v_3 : Although v_3 with respect to the event plane is almost similar to v_3 from the two-particle cumulant method, v_3 from the four-particle cumulant method is roughly a half of them. This has already been confirmed in the experimental data [38]. In the hydrodynamic simulations, one usually obtains smooth distributions using the Cooper-Frye formula. However, Monte-Carlo sampling from these smooth momentum distributions is necessary to perform particle-based analysis method, *i.e.*, event-plane method or multi-particle cumulants methods. Of course, the subsequent hadronic cascading is also important and required to describe the gradual freezeout in the hadronic rescattering stage.

We also showed that, for higher order harmonics ($n \geq 4$), the participant plane defined using initial profiles does not correlate with the event plane defined using final particle samples. This means that calculations using event-averaged initial conditions where the orientation angles of the anisotropy ε_n are matched, are questionable.

The PHENIX Collaboration found [245] that the Glauber initialisation followed by viscous hydrodynamic simulations with $\eta/s = 0.08$ simultaneously reproduced v_2 and v_3 as functions of centrality, while the KLN initialisation with $\eta/s = 0.16$ leads to a reasonable reproduction only of v_2 . After that, it was found that fluctuation of particle production obeying KNO scaling at midrapidity enhances initial spatial anisotropy ε_{2n+1} ($n \geq 1$) at all centralities [175]. The initial conditions including this feature could lead to enhancement of v_{2n+1} with keeping v_2 . This would change our understanding of v_2 and v_3 as functions of centrality above. Although it would be interesting to consider this KNO scaling idea

in the integrated dynamical model, how to formulate it in rapidity direction is an open question.

We assumed that initial entropy production can directly be used as initial conditions in hydrodynamic simulations and neglected the description of any thermalisation processes. As known, thermalisation is one of the outstanding open questions in the physics of relativistic heavy ion collisions.

In the event-by-event hydrodynamic simulations, thermal fluctuations during evolutions might have been important [246]. In this case, hydrodynamic equations (more specifically, constitutive equations) are no longer the deterministic equations, but become the stochastic equations. Since the fluctuation-dissipation relation tells us thermal fluctuation of the energy momentum tensor is intimately related with viscosity, one should include fluctuation in the dynamical evolution, in particular, in the event-by-event simulations.

Switching from a hydrodynamic picture to a particle picture has several open issues. Some procedures adopted in the present study do not respect energy-momentum conservation. We neglected in-coming particles which contribute as negative number in the phase space distribution. This could have been resolved partly by simulating hydrodynamics and hadron cascade simultaneously and by explicitly treating absorption of particles coming inside fluid regions. The negative contributions are an issue for the space-like hypersurface elements, but even for the time-like elements, the sampling of the finite number of particles violates the energy-momentum conservation in an individual event. The conservation recovers only when over-sampling of particles is made.

Regarding a switch from a fluid to a gas, one natural question would be when and how hydrodynamic picture breaks down. In the present study, the switching temperature is just an adjustable parameter to reproduce particle ratios among hadrons. It is interesting to note that the switching temperature $T_{\text{sw}} = 155$ MeV obtained in this study is very close to the pseudocritical temperature of the chiral phase transition. In fact, it has been claimed [247, 248] that bulk viscosity enhanced in the vicinity of cross-over region would trigger this transition from thermalised fluid to individual particles.

Acknowledgment

The authors acknowledge the fruitful discussion with S. Esumi and Y. Hori about the flow analysis methods. T.H. acknowledge a kind hospitality from the nuclear theory group at Lawrence Berkeley National Laboratory where a part of work was done when he visited there on sabbatical. The work of T.H. was supported by Grant-in-Aid for Scientific Research Nos. 22740151 and 22340052, the work of P.H. by BMBF under contract no. 06FY9092, the work of K.M. by JSPS Research Fellowships for Young Scientists, and the work of Y.N. by Grant-in-Aid for Scientific Research No. 20540276.

Appendix

In this Appendix, we show some technical details about momentum integration of the Cooper-Frye formula [86] for the purpose of less numerical costs [94].

Since the number is Lorentz invariant, Equation (15) can be Lorentz-transformed to the local rest frame using four flow velocity u^μ and written as

$$\begin{aligned} \Delta N_\pm &= \int \frac{d^3p}{E} \frac{[p \cdot \Delta\sigma]_\pm}{\exp[(p \cdot u - \mu)/T] - \epsilon} \\ &= \int \frac{d^3\bar{p}}{\bar{E}} \frac{[\bar{p} \cdot \Delta\bar{\sigma}]_\pm}{\exp[(\bar{E} - \mu)/T] - \epsilon} \end{aligned} \quad (85)$$

where $[\dots]_\pm = \Theta(\pm \dots)|\dots|$. Hereafter integral variables $\bar{p} = (\bar{E}, \vec{\bar{p}})$ can be renamed as p . In the following, we discuss only about out-going particles $[\dots]_+$. Results for in-coming particles $[\dots]_-$ can

be easily obtained by replacing $\Delta\bar{\sigma}$ with $-\Delta\bar{\sigma}$. Taking the z axis being parallel to $\Delta\bar{\sigma}$,

$$\begin{aligned} [p \cdot \Delta\bar{\sigma}]_+ &= [E\Delta\bar{\sigma}^0 - p_z |\Delta\bar{\sigma}|]_+ \\ &= [E\Delta\bar{\sigma}^0 - p \cos\theta |\Delta\bar{\sigma}|]_+. \end{aligned} \quad (86)$$

Thus, the above integration becomes

$$\Delta N_+ = \int \frac{dp}{\exp[(E - \mu)/T] - \epsilon} \frac{2\pi p^2 d\cos\theta}{E} [E\Delta\bar{\sigma}^0 - p \cos\theta |\Delta\bar{\sigma}|]_+. \quad (87)$$

When $|\Delta\bar{\sigma}| = 0$, we easily integrate the above equation and the results becomes

$$\Delta N_+ = 4\pi \int \frac{p^2 dp}{\exp[(E - \mu)/T] - \epsilon} [\Delta\bar{\sigma}^0]_+. \quad (88)$$

When $|\Delta\bar{\sigma}| > 0$, a short calculation leads to

$$\begin{aligned} [E\Delta\bar{\sigma}^0 - p \cos\theta |\Delta\bar{\sigma}|]_+ &= p |\Delta\bar{\sigma}| \left[\frac{E\Delta\bar{\sigma}^0}{p |\Delta\bar{\sigma}|} - \cos\theta \right]_+ \\ &= p |\Delta\bar{\sigma}| [A - \cos\theta]_+ \end{aligned} \quad (89)$$

$$A = \frac{E \Delta\bar{\sigma}^0}{|\mathbf{p}| |\Delta\bar{\sigma}|} \quad (90)$$

First, we integrate the above equation with respect to $\cos\theta$

$$\begin{aligned} \int_{-1}^1 d\cos\theta [A - \cos\theta]_+ &= \int_{-1}^1 d\cos\theta (A - \cos\theta) \Theta(A - \cos\theta) \\ &= 2A\Theta(A - 1) + \frac{(A + 1)^2}{2} \Theta(1 - |A|), \end{aligned} \quad (91)$$

where Θ is the Heaviside function. Let us define ‘‘velocity’’ and ‘‘momentum’’ of surface vector as $v_{\bar{\sigma}} = \Delta\bar{\sigma}^0/|\Delta\bar{\sigma}|$ and $p_{\bar{\sigma}} = m|v_{\bar{\sigma}}|/\sqrt{1 - v_{\bar{\sigma}}^2}$, respectively.

Finally we obtain

$$\begin{aligned} \Delta N_+ &= 4\pi \int_0^\infty \frac{p^2 dp}{\exp[(E - \mu)/T] - \epsilon} [\Delta\bar{\sigma}^0]_+ \\ &+ \Theta(1 - |v_{\bar{\sigma}}|) \left(\pi |\Delta\bar{\sigma}| \int_{p_{\bar{\sigma}}}^\infty \frac{p(E^2 v_{\bar{\sigma}}^2 + p^2) dp}{\exp[(E - \mu)/T] - \epsilon} - 2\pi |\Delta\bar{\sigma}^0| \int_{p_{\bar{\sigma}}}^\infty \frac{p^2 dp}{\exp[(E - \mu)/T] - \epsilon} \right). \end{aligned} \quad (92)$$

Remembering that the hypersurface elements have been Lorentz-transformed, we have to Lorentz-transform back to the laboratory frame:

$$\Delta\bar{\sigma}^0 = u \cdot \Delta\sigma \quad (93)$$

$$\begin{aligned} |\Delta\bar{\sigma}|^2 &= (\Delta\bar{\sigma}^0)^2 - \Delta\bar{\sigma} \cdot \Delta\bar{\sigma} \\ &= -(g_{\mu\nu} - u_\mu u_\nu) \Delta\sigma^\mu \Delta\sigma^\nu \end{aligned} \quad (94)$$

Now the three-dimensional integral with a complicated integrand such as $[\dots]_\pm$ reduces to the one-dimensional one and it is easily done numerically.

References

- [1] K. Yagi, T. Hatsuda and Y. Miake, *Quark-gluon plasma: From big bang to little bang*, (Cambridge, 2005).
- [2] C. Adler *et al.* [STAR Collaboration], *Phys. Rev. Lett.* 87 (2001) 182301
- [3] C. Adler *et al.* [STAR Collaboration], *Phys. Rev. C* 66 (2002) 034904
- [4] J. Adams *et al.* [STAR Collaboration], *Phys. Rev. Lett.* 92 (2001) 052302
- [5] K. Adcox *et al.* [PHENIX Collaboration], *Phys. Rev. Lett.* 89 (2002) 212301
- [6] S. S. Adler *et al.* [PHENIX Collaboration], *Phys. Rev. Lett.* 91 (2003) 182301
- [7] S. S. Adler *et al.* [PHENIX Collaboration], *Phys. Rev. Lett.* 94 (2005) 232302
- [8] B. B. Back *et al.* [PHOBOS Collaboration], *Phys. Rev. Lett.* 89 (2002) 222301
- [9] B. B. Back *et al.* [PHOBOS Collaboration], *Phys. Rev. Lett.* 94 (2005) 122303
- [10] B. B. Back *et al.* [PHOBOS Collaboration], *Phys. Rev. C* 72 (2005) 051901
- [11] K. Aamodt *et al.* [ALICE Collaboration], *Phys. Rev. Lett.* 105 (2010) 252302
- [12] G. Aad *et al.* [ATLAS Collaboration], *Phys. Lett. B* 707 (2012) 330
- [13] J. Velkovska [CMS Collaboration], *J. Phys. G* 38 (2011) 124011
- [14] U. Heinz and P. F. Kolb, *Nucl. Phys. A* 702 (2002) 269
- [15] M. Gyulassy, preprint arXiv:nucl-th/0403032
- [16] J. Y. Ollitrault, *Phys. Rev. D* 46 (1992) 229
- [17] P. F. Kolb, P. Huovinen, U. W. Heinz and H. Heiselberg, *Phys. Lett. B* 500 (2001) 232
- [18] P. Huovinen, P. F. Kolb, U. W. Heinz, P. V. Ruuskanen and S. A. Voloshin, *Phys. Lett. B* 503 (2001) 58
- [19] D. Teaney, J. Lauret and E. V. Shuryak, *Phys. Rev. Lett.* 86 (2001) 4789
- [20] D. Teaney, J. Lauret and E. V. Shuryak, preprint arXiv:nucl-th/0110037
- [21] T. Hirano, *Phys. Rev. C* 65 (2002) 011901
- [22] T. Hirano and K. Tsuda, *Phys. Rev. C* 66 (2002) 054905
- [23] http://www.bnl.gov/bnlweb/pubaf/pr/PR_display.asp?prID=05-38
- [24] T. D. Lee, *Nucl. Phys. A* 750 (2005) 1
- [25] M. Gyulassy, L. McLerran, *Nucl. Phys. A* 750 (2005) 30
- [26] E. V. Shuryak, *Nucl. Phys. A* 750 (2005) 64
- [27] T. Hirano and M. Gyulassy, *Nucl. Phys. A* 769 (2006) 71
- [28] M. L. Miller, K. Reygers, S. J. Sanders and P. Steinberg, *Ann. Rev. Nucl. Part. Sci.* 57 (2007) 205
- [29] W. Broniowski, M. Rybczynski and P. Bozek, *Comput. Phys. Commun.* 180 (2009) 69
- [30] B. Alver, M. Baker, C. Loizides and P. Steinberg, preprint arXiv:0805.4411 [nucl-ex]
- [31] C. Alt *et al.* [NA49 Collaboration], *Phys. Rev. C* 68 (2003) 034903
- [32] B. Alver *et al.* [PHOBOS Collaboration], *Phys. Rev. Lett.* 98 (2007) 242302
- [33] M. Miller and R. Snellings, preprint nucl-ex/0312008
- [34] B. Alver and G. Roland, *Phys. Rev. C* 81 (2010) 054905 [Erratum *Phys. Rev. C* 82 (2010) 039903]
- [35] J. Adams *et al.* [STAR Collaboration], *Phys. Rev. Lett.* 95 (2005) 152301
- [36] S. S. Adler *et al.* [PHENIX Collaboration], *Phys. Rev. Lett.* 97 (2006) 052301
- [37] A. Adare *et al.* [PHENIX Collaboration], *Phys. Rev. C* 78 (2008) 014901

- [38] K. Aamodt *et al.* [ALICE Collaboration], *Phys. Lett. B* 708 (2012) 249
- [39] G. Aad *et al.* [ATLAS Collaboration], *Phys. Rev. C* 86 (2012) 014907
- [40] E. Shuryak, *Phys. Rev. C* 80 (2009) 054908 [Erratum *Phys. Rev. C* 80 (2009) 069902]
- [41] P. Staig and E. Shuryak, *Phys. Rev. C* 84 (2011) 034908
- [42] P. Staig and E. Shuryak, *Phys. Rev. C* 84 (2011) 044912
- [43] A. Mocsy and P. Sorensen, preprint arXiv:1008.3381 [hep-ph]
- [44] P. Sorensen, B. Bolliet, A. Mocsy, Y. Pandit and N. Pruthi, *Phys. Lett. B* 705 (2011) 71
- [45] E. Komatsu *et al.* [WMAP Collaboration], *Astrophys. J. Suppl.* 180 (2009) 330
- [46] <http://lambda.gsfc.nasa.gov/toolbox/>
- [47] https://karman.physics.purdue.edu/OSCAR/index.php/Main_Page
- [48] E. Iancu, A. Leonidov and L. McLerran, preprint arXiv:hep-ph/0202270
- [49] E. Iancu and R. Venugopalan, in *Quark Gluon Plasma 3 (QGP3)* (2004) 249. Eds. R. C. Hwa and X. N. Wang, World Scientific
- [50] F. Gelis, E. Iancu, J. Jalilian-Marian and R. Venugopalan, *Ann. Rev. Nucl. Part. Sci.* 60 (2010) 463
- [51] G. Gatoff, A. K. Kerman and T. Matsui, *Phys. Rev. D* 36 (1987) 114
- [52] T. Lappi and L. McLerran, *Nucl. Phys. A* 772 (2006) 200
- [53] T. Hirano, P. Huovinen and Y. Nara, *Phys. Rev. C* 83 (2011) 021902
- [54] T. Hirano, P. Huovinen and Y. Nara, *Phys. Rev. C* 84 (2011) 011901
- [55] H.-J. Drescher and Y. Nara, *Phys. Rev. C* 75 (2007) 034905
- [56] H.-J. Drescher and Y. Nara, *Phys. Rev. C* 76 (2007) 041903
- [57] T. Hirano and Y. Nara, *Phys. Rev. C* 79 (2009) 064904
- [58] M. Cheng, N. H. Christ, S. Datta, J. van der Heide, C. Jung, F. Karsch, O. Kaczmarek and E. Laermann *et al.*, *Phys. Rev. D* 77 (2008) 014511
- [59] A. Bazavov, T. Bhattacharya, M. Cheng, N. H. Christ, C. DeTar, S. Ejiri, S. Gottlieb and R. Gupta *et al.*, *Phys. Rev. D* 80 (2009) 014504
- [60] P. Huovinen and P. Petreczky, *Nucl. Phys. A* 837 (2010) 26
- [61] Y. Nara, N. Otuka, A. Ohnishi, K. Niita and S. Chiba, *Phys. Rev. C* 61 (2000) 024901
- [62] T. Hirano and Y. Nara, *Prog. Theor. Exp. Phys.* 1 (2012) 01A203
- [63] A. M. Poskanzer and S. A. Voloshin, *Phys. Rev. C* 58 (1998) 1671
- [64] N. Borghini, P. M. Dinh and J.-Y. Ollitrault, *Phys. Rev. C* 63 (2001) 054906
- [65] N. Borghini, P. M. Dinh and J.-Y. Ollitrault, *Phys. Rev. C* 64 (2001) 054901
- [66] C. Adler *et al.* [STAR Collaboration], *Phys. Rev. Lett.* 90 (2003) 4778 [Erratum *Phys. Rev. Lett.* 90 (2003) 119903]
- [67] S. S. Adler *et al.* [PHENIX Collaboration], *Phys. Rev. C* 69 (2004) 034909
- [68] B. I. Abelev *et al.* [STAR Collaboration], *Phys. Rev. C* 79 (2009) 034909
- [69] M. Floris, talk at Quark Matter 2011, Annecy, France
- [70] D. H. Rischke, In *Cape Town 1998, Hadrons in dense matter and hadrosynthesis* 21-70 [nucl-th/9809044]
- [71] P. Colella and P. R. Woodward, *J. Comput. Phys.* 54 (1984) 174
- [72] P. Petreczky, *J. Phys. G* 39 (2012) 093002

- [73] S. Borsanyi, G. Endrodi, Z. Fodor, A. Jakovac, S. D. Katz, S. Krieg, C. Ratti and K. K. Szabo, *JHEP* 1011 (2010) 077
- [74] R. Venugopalan and M. Prakash, *Nucl. Phys. A* 546 (1992) 718
- [75] M. Cheng *et al.*, *Phys. Rev. D* 81 (2010) 054504
- [76] A. Bazavov *et al.* [HotQCD Collaboration], *PoS LATTICE 2010* (2010) 169
- [77] P. F. Kolb, U. W. Heinz, P. Huovinen, K. J. Eskola and K. Tuominen, *Nucl. Phys. A* 696 (2001) 197
- [78] P. Huovinen and P. V. Ruuskanen, *Ann. Rev. Nucl. Part. Sci.* 56 (2006) 163
- [79] J. Adams *et al.* [STAR Collaboration], *Phys. Rev. C* 72 (2005) 014904
- [80] P. Huovinen, *Nucl. Phys. A* 761 (2005) 296
- [81] J. Sollfrank, P. Huovinen, M. Kataja, P. V. Ruuskanen, M. Prakash and R. Venugopalan, *Phys. Rev. C* 55 (1997) 392
- [82] R. A. Schneider and W. Weise, *Phys. Rev. C* 64 (2001) 055201 .
- [83] M. Chojnacki and W. Florkowski, *Acta Phys. Polon. B* 38 (2007) 3249
- [84] M. Chojnacki, W. Florkowski, W. Broniowski and A. Kisiel, *Phys. Rev. C* 78 (2008) 014905
- [85] H. Song, S. A. Bass, U. Heinz, T. Hirano and C. Shen, *Phys. Rev. C* 83 (2011) 054910
- [86] F. Cooper and G. Frye, *Phys. Rev. D* 10 (1974) 186
- [87] P. Huovinen and H. Petersen, *Eur. Phys. J. A* 48 (2012) 171
- [88] G. Welke, R. Malfliet, C. Gregoire, M. Prakash and E. Suraud, *Phys. Rev. C* 40 (1989) 2611
- [89] D. Molnar and M. Gyulassy, *Phys. Rev. C* 62 (2000) 054907
- [90] A. Lang, H. Babovsky, W. Cassing, U. Mosel, H-G. Reusch, and K. Weber, *J. Comp. Phys.* 106 (1993) 391
- [91] P. Danielewicz and G. F. Bertsch, *Nucl. Phys. A* 533 (1991) 712
- [92] Z. Xu and C. Greiner, *Phys. Rev. C* 71 (2005) 064901
- [93] H. Petersen, J. Steinheimer, G. Burau, M. Bleicher and H. Stocker, *Phys. Rev. C* 78 (2008) 044901
- [94] K. Murase, “Relativistic hydrodynamic model with event-by-event fluctuation in high energy heavy ion collisions”, master thesis (in Japanese), the University of Tokyo (2012).
- [95] M. Isse, A. Ohnishi, N. Otuka, P. K. Sahu and Y. Nara, *Phys. Rev. C* 72 (2005) 064908
- [96] H. Sorge, H. Stöcker and W. Greiner, *Annals Phys.* 192 (1989) 266
- [97] H. Sorge, A. von Keitz, R. Mattiello, H. Stöcker and W. Greiner, *Z. Phys. C* 47 (1990) 629
- [98] H. Sorge, L. Winkelmann, H. Stöcker and W. Greiner, *Z. Phys. C* 59 (1993) 85
- [99] H. Sorge, *Phys. Rev. C* 52 (1995) 3291
- [100] L. A. Winkelmann *et al.*, *Nucl. Phys. A* 610 (1996) 116c
- [101] S. A. Bass *et al.*, *Prog. Part. Nucl. Phys.* 41 (1998) 225
- [102] M. Bleicher *et al.*, *J. Phys. G* 25 (1999) 1859
- [103] G. F. Bertsch and S. Das Gupta, *Phys. Rep.* 160 (1998) 189
- [104] J. Aichelin, *Phys. Rep.* 202 (1991) 233
- [105] X. N. Wang and M. Gyulassy, *Phys. Rev. D* 44 (1991) 3501
- [106] X. N. Wang, *Phys. Rep.* 280 (1997) 287
- [107] X. N. Wang and M. Gyulassy, *Comp. Phys. Comm.* 83 (1994) 307
- [108] <http://www-nsdth.lbl.gov/~xnwang/hijing/>
- [109] B. Andersson, G. Gustafson and H. Pi, *Z. Phys. C* 57 (1993) 485

- [110] H. Pi, *Comp. Phys. Comm.* 71 (1992) 173
- [111] B. Andersson, G. Gustafson, G. Ingelman and T. Sjöstrand, *Phys. Rep.* 97 (1983) 31
- [112] B. Andersson, *The Lund Model*, (Cambridge, 2005).
- [113] T. Sjostrand, S. Mrenna and P. Z. Skands, *JHEP* 0605 (2006) 026
- [114] A. Bialas, M. Gyulassy, *Nucl. Phys. A* 291 (1987) 793
- [115] Gy. Wolf, W. Cassing, U. Mosel, *Nucl. Phys. A* 552 (1993) 549
- [116] B.-A. Li, *Nucl. Phys. A* 552 (1993) 605
- [117] A. Dumitru, S. A. Bass, M. Bleicher, H. Stoecker and W. Greiner, *Phys. Lett. B* 460 (1999) 411
- [118] S. A. Bass, A. Dumitru, M. Bleicher, L. Bravina, E. Zabrodin, H. Stoecker and W. Greiner, *Phys. Rev. C* 60 (1999) 021902
- [119] S. A. Bass and A. Dumitru, *Phys. Rev. C* 61 (2000) 064909
- [120] E. Andersen *et al.* [WA97 Collaboration], *Phys. Lett. B* 433 (1998) 209
- [121] H. Appelshäuser *et al.* [NA49 Collaboration], *Phys. Lett. B* 444 (1998) 523
- [122] A. M. Poskanzer *et al.* [NA49 Collaboration], *Nucl. Phys. A* 661 (1999) 341c
- [123] K. H. Ackermann *et al.* [STAR Collaboration], *Phys. Rev. Lett.* 86 (2001) 401
- [124] K. Adcox *et al.* [PHENIX Collaboration], *Nucl. Phys. A* 757 (2005) 184
- [125] T. Hirano, U. W. Heinz, D. Kharzeev, R. Lacey, Y. Nara, *Phys. Lett. B* 636 (2006) 299
- [126] T. Hirano, U. W. Heinz, D. Kharzeev, R. Lacey and Y. Nara, *Phys. Rev. C* 77 (2008) 044909
- [127] P. F. Kolb, *Heavy Ion Phys.* 15 (2002) 279
- [128] M. .Nasim [STAR Collaboration], arXiv:1210.5045 [nucl-ex]
- [129] C. Nonaka and S. A. Bass, *Phys. Rev. C* 75 (2007) 014902
- [130] H. Petersen and M. Bleicher, *Phys. Rev. C* 79 (2009) 054904
- [131] H. Petersen and M. Bleicher, *Phys. Rev. C* 81 (2010) 044906
- [132] H. Petersen, G.-Y. Qin, S. A. Bass and B. Muller, *Phys. Rev. C* 82 (2010) 041901
- [133] G.-Y. Qin, H. Petersen, S. A. Bass and B. Muller, *Phys. Rev. C* 82 (2010) 064903
- [134] H. Petersen, V. Bhattacharya, S. A. Bass and C. Greiner, *Phys. Rev. C* 84 (2011) 054908
- [135] H. Petersen, *Phys. Rev. C* 84 (2011) 034912
- [136] S. Pratt and J. Vredevoogd, *Phys. Rev. C* 78 (2008) 054906 [Erratum-ibid. C 79 (2009) 069901]
- [137] K. Werner, I. Karpenko, T. Pierog, M. Bleicher and K. Mikhailov, *Phys. Rev. C* 82 (2010) 044904
- [138] K. Werner, I. .Karpenko, T. Pierog, M. Bleicher and K. Mikhailov, *Phys. Rev. C* 83 (2011) 044915
- [139] K. Werner, I. .Karpenko and T. Pierog, *Phys. Rev. Lett.* 106 (2011) 122004
- [140] K. Werner, I. Karpenko, M. Bleicher, T. Pierog and S. Porteboeuf-Houssais, *Phys. Rev. C* 85 (2012) 064907
- [141] H. Song, S. A. Bass, U. Heinz, T. Hirano and C. Shen, *Phys. Rev. Lett.* 106 (2011) 192301 ; [Erratum-ibid. 109 (2012) 139904]
- [142] H. Song, S. A. Bass and U. Heinz, *Phys. Rev. C* 83 (2011) 024912
- [143] H. Song, S. A. Bass and U. Heinz, *Phys. Rev. C* 83 (2011) 054912
- [144] P. Kovtun, D. T. Son and A. O. Starinets, *Phys. Rev. Lett.* 94 (2005) 111601
- [145] R. A. Soltz, I. Garishvili, M. Cheng, B. Abelev, A. Glenn, J. Newby, L. A. L. Levy and S. Pratt, preprint arXiv:1208.0897 [nucl-th]
- [146] S. Ryu, S. Jeon, C. Gale, B. Schenke and C. Young, preprint arXiv:1210.4588 [hep-ph]
- [147] A. Krasnitz and R. Venugopalan, *Nucl. Phys. B* 557 (1999) 237

- [148] A. Krasnitz and R. Venugopalan, *Phys. Rev. Lett.* 84 (2000) 4309
- [149] A. Krasnitz and R. Venugopalan, *Phys. Rev. Lett.* 86 (2001) 1717
- [150] A. Krasnitz, Y. Nara and R. Venugopalan, *Phys. Rev. Lett.* 87 (2001) 192302
- [151] A. Krasnitz, Y. Nara and R. Venugopalan, *Nucl. Phys. A* 717 (2003) 268
- [152] A. Krasnitz, Y. Nara and R. Venugopalan, *Nucl. Phys. A* 727 (2003) 427
- [153] T. Lappi, *Phys. Rev. C* 67 (2003) 054903
- [154] T. Lappi, *Phys. Rev. C* 70 (2004) 054905
- [155] L. V. Gribov, E. M. Levin and M. G. Ryskin, *Phys. Rep.* 100 (1983) 1
- [156] D. Kharzeev and E. Levin, *Phys. Lett. B* 523 (2001) 79
- [157] D. Kharzeev, E. Levin, and M. Nardi, *Phys. Rev. C* 71 (2005) 054903
- [158] D. Kharzeev, E. Levin, and M. Nardi, *Nucl. Phys. A* 730 (2004) 448
- [159] A. Adil, H. J. Drescher, A. Dumitru, A. Hayashigaki, and Y. Nara, *Phys. Rev. C* 74 (2006) 044905
- [160] F. Gelis, A. M. Stasto and R. Venugopalan, *Eur. Phys. J. C* 48 (2006) 489
- [161] J. L. Albacete, *Phys. Rev. Lett.* 99 (2007) 262301
- [162] J. L. Albacete and C. Marquet, *Phys. Lett. B* 687 (2010) 174
- [163] E. Levin and A. H. Rezaeian, *Phys. Rev. D* 82 (2010) 014022
- [164] E. Levin and A. H. Rezaeian, *Phys. Rev. D* 82 (2010) 054003
- [165] E. Levin and A. H. Rezaeian, *Phys. Rev. D* 83 (2011) 114001
- [166] P. Tribedy and R. Venugopalan, *Nucl. Phys. A* 850 (2011) 136 [Erratum *Nucl. Phys. A* 859 (2011) 185]
- [167] P. Tribedy and R. Venugopalan, *Phys. Lett. B* 710 (2012) 125
- [168] A. Dumitru, D. E. Kharzeev, E. M. Levin and Y. Nara, *Phys. Rev. C* 85 (2012) 044920
- [169] J. L. Albacete and A. Dumitru, preprint arXiv:1011.5161[hep-ph]; http://faculty.baruch.cuny.edu/naturalscience/physics/dumitru/CGC_IC.html
- [170] J. L. Albacete, A. Dumitru and Y. Nara, *J. Phys. Conf. Ser.* 316 (2011), 012011
- [171] H. J. Drescher and Y. Nara, *Phys. Rev. C* 75 (2007) 034905
- [172] J. L. Albacete, A. Dumitru, H. Fujii and Y. Nara, *Nucl. Phys. A* 897 (2013) 1
- [173] H. J. Drescher and Y. Nara, *Phys. Rev. C* 76 (2007) 041903(R)
- [174] B. Muller and A. Schafer, *Phys. Rev. D* 85 (2012) 114030
- [175] A. Dumitru and Y. Nara, *Phys. Rev. C* 85 (2012) 034907
- [176] R. M. Barnett *et al.*, *Phys. Rev. D* 54 (1996) 1
- [177] G. A. Schuler and T. Sjostrand, *Nucl. Phys. B* 407 (1993) 539
- [178] G. A. Schuler and T. Sjostrand, *Phys. Rev. D* 49 (1994) 2257
- [179] H. De Vries, C. W. De Jager and C. De Vries, *Atom. Data Nucl. Data Tabl.* 36 (1987) 495
- [180] U. Heinz and J. S. Moreland, *Phys. Rev. C* 84 (2011) 054905
- [181] P. Filip, R. Lednicky, H. Masui and N. Xu, *Phys. Rev. C* 80 (2009) 054903
- [182] K. Aamodt *et al.* [ALICE Collaboration], *Phys. Rev. Lett.* 106 (2011) 032301
- [183] K. Aamodt *et al.* [ALICE Collaboration], *Phys. Rev. Lett.* 106 (2011) 032301
- [184] K. Aamodt *et al.* [ALICE Collaboration], *Eur. Phys. J. C* 68 (2010) 89
- [185] Y. Nara, *Prog. Theor. Phys. Suppl.* 193 (2012) 145
- [186] D. Kharzeev and M. Nardi, *Phys. Lett. B* 507 (2001) 121

- [187] K. Golec-Biernat and M. Wusthoff, *Phys. Rev. D* 59 (1999) 014017
- [188] K. Golec-Biernat and M. Wusthoff, *Phys. Rev. D* 60 (1999) 114023
- [189] D. Teaney and L. Yan, *Phys. Rev. C* 83 (2011) 064904
- [190] B. H. Alver, C. Gombeaud, M. Luzum and J.-Y. Ollitrault, *Phys. Rev. C* 82 (2010) 034913
- [191] R. S. Bhalerao, M. Luzum and J.-Y. Ollitrault, *Phys. Rev. C* 84 (2011) 034910
- [192] R. S. Bhalerao, M. Luzum and J.-Y. Ollitrault, *Phys. Rev. C* 84 (2011) 054901
- [193] F. G. Gardim, F. Grassi, M. Luzum and J.-Y. Ollitrault, *Phys. Rev. C* 85 (2012) 024908
- [194] B. Alver *et al.*, *Phys. Rev. C* 77 (2008) 014906
- [195] S. J. Brodsky, J. F. Gunion and J. H. Kuhn, *Phys. Rev. Lett.* 39 (1977) 1120
- [196] A. Adil and M. Gyulassy, *Phys. Rev. C* 72 (2005) 034907
- [197] B. B. Back *et al.*, *Phys. Rev. Lett.* 91 (2003) 052303
- [198] J. D. Bjorken, *Phys. Rev. D* 27 (1983) 140
- [199] M. Gyulassy, D. H. Rischke and B. Zhang, *Nucl. Phys. A* 613 (1997) 397
- [200] H. J. Drescher, M. Hladik, S. Ostapchenko, T. Pierog and K. Werner, *Phys. Rept.* 350 (2001) 93
- [201] T. Osada, C. E. Aguiar, Y. Hama and T. Kodama, nucl-th/0102011
- [202] C. E. Aguiar, Y. Hama, T. Kodama and T. Osada, *Nucl. Phys. A* 698 (2002) 639
- [203] Y. Hama, T. Kodama and O. Socolowski, Jr., *Braz. J. Phys.* 35 (2005) 24
- [204] R. Andrade, F. Grassi, Y. Hama, T. Kodama and O. Socolowski, Jr., *Phys. Rev. Lett.* 97 (2006) 202302
- [205] R. P. G. Andrade, F. Grassi, Y. Hama, T. Kodama and W. L. Qian, *Phys. Rev. Lett.* 101 (2008) 112301
- [206] J. Takahashi, B. M. Tavares, W. L. Qian, R. Andrade, F. Grassi, Y. Hama, T. Kodama and N. Xu, *Phys. Rev. Lett.* 103 (2009) 242301
- [207] F. G. Gardim, F. Grassi, Y. Hama, M. Luzum and J.-Y. Ollitrault, *Phys. Rev. C* 83 (2011) 064901
- [208] Y. Cheng, L. P. Csernai, V. K. Magas, B. R. Schlei and D. Strottman, *Phys. Rev. C* 81 (2010) 064910
- [209] Y.-Y. Ren, W.-N. Zhang and J.-L. Liu, *Phys. Lett. B* 669 (2008) 317
- [210] C. Adler *et al.* [STAR Collaboration], *Phys. Rev. Lett.* 87 (2001) 082301
- [211] K. Adcox *et al.* [PHENIX Collaboration], *Phys. Rev. Lett.* 88 (2002) 192302
- [212] H. Holopainen, H. Niemi and K. J. Eskola, *Phys. Rev. C* 83 (2011) 034901
- [213] R. Chatterjee, H. Holopainen, T. Renk and K. J. Eskola, *Phys. Rev. C* 83 (2011) 054908
- [214] T. Renk, H. Holopainen, J. Auvinen and K. J. Eskola, preprint arXiv:1105.2647 [hep-ph]
- [215] Z. Qiu and U. W. Heinz, *Phys. Rev. C* 84 (2011) 024911
- [216] Z. Qiu and U. W. Heinz, *Phys. Lett. B* 717 (2012) 261
- [217] J. Jia [ATLAS Collaboration], preprint arXiv:1208.1427 [nucl-ex]
- [218] K. Werner, F.-M. Liu and T. Pierog, *Phys. Rev. C* 74 (2006) 044902
- [219] B. Schenke, S. Jeon and C. Gale, *Phys. Rev. Lett.* 106 (2011) 042301
- [220] B. Schenke, S. Jeon and C. Gale, *Phys. Rev. C* 85 (2012) 024901
- [221] B. Schenke, P. Tribedy and R. Venugopalan, *Phys. Rev. Lett.* 108 (2012) 252301
- [222] C. Gale, S. Jeon, B. Schenke, P. Tribedy and R. Venugopalan, preprint arXiv:1209.6330 [nucl-th]
- [223] B. Schenke, P. Tribedy and R. Venugopalan, *Phys. Rev. C* 86 (2012) 034908
- [224] J. Bartels, K.J. Golec-Biernat and H. Kowalski, *Phys. Rev. D* 66 (2002) 014001

- [225] H. Kowalski and D. Teaney, *Phys. Rev. D* 68 (2003) 114005
- [226] A. K. Chaudhuri, *Phys. Lett. B* 710 (2012) 339
- [227] A. K. Chaudhuri, *Phys. Lett. B* 713 (2012) 91
- [228] M. .Rihan Haque, V. Roy and A. K. Chaudhuri, *Phys. Rev. C* 86 (2012) 037901
- [229] P. Bozek and W. Broniowski, *Phys. Rev. C* 85 (2012) 044910
- [230] L. Pang, Q. Wang and X. -N. Wang, *Phys. Rev. C* 86 (2012) 024911
- [231] H. Zhang, T. Song and C. M. Ko, preprint arXiv:1208.2980 [hep-ph]
- [232] B. I. Abelev *et al.* [STAR Collaboration], *Phys. Rev. C* 81 (2010) 044902
- [233] J.-Y. Ollitrault, A. M. Poskanzer, and S. A. Voloshin, *Phys. Rev. C* 80 (2009) 014904
- [234] S. Afanasiev *et al.* [PHENIX Collaboration], *Phys. Rev. C* 80 (2009) 024909
- [235] A. Adare *et al.* [PHENIX Collaboration], *Phys. Rev. Lett.* 98 (2008) 162301
- [236] X. Zhang *et al.* [STAR Collaboration], *Acta Phys. Polon. Supp.* 5 (2012) 509
- [237] M. Luzum, *Phys. Rev. C* 83 (2011) 044911
- [238] S. A. Voloshin, A. M. Poskanzer, A. Tang, and G. Wang, *Phys. Lett. B* 659 (2008) 537
- [239] P. Arnold, G. D. Moore and L. G. Yaffe, *JHEP* 05 (2003) 051
- [240] H. Niemi, G. S. Denicol, P. Huovinen, E. Molnar and D. H. Rischke, *Phys. Rev. Lett.* 106 (2011) 212302
- [241] H. Niemi, G. S. Denicol, P. Huovinen, E. Molnar and D. H. Rischke, *Phys. Rev. C* 86 (2012) 014909
- [242] N. Borghini and J. -Y. Ollitrault, *Phys. Lett. B* 642 (2006) 227
- [243] D. Teaney, *Phys. Rev. C* 68 (2003) 034913
- [244] X. -l. Zhu, M. Bleicher and H. Stoecker, *Phys. Rev. C* 72 (2005) 064911
- [245] A. Adare *et al.* [PHENIX Collaboration], *Phys. Rev. Lett.* 107 (2011) 252301
- [246] J. I. Kapusta, B. Muller and M. Stephanov, *Phys. Rev. C* 85 (2012) 054906
- [247] G. Torrieri, B. Tomasik and I. Mishustin, *Phys. Rev. C* 77 (2008) 034903
- [248] K. Rajagopal and N. Tripuraneni, *JHEP* 1003 (2010) 018